Development of Nanostructured Cathode Materials for Lithium-Sulfur Battery Applications

This thesis is presented in fulfilment of the requirement for the degree of

DOCTOR OF PHILOSOPHY

of the

University of Technology Sydney

By

Tuhin Subhra Sahu, B. Sc., M. Sc.

March-2022

CERTIFICATE OF ORIGINAL AUTHORSHIP

I certify that the work presented in this thesis has not previously been submitted for a degree or submitted as part of requirements for a degree except as fully acknowledged within the text.

I also certify that the I have written the thesis. Any help that I have received in my research work and the thesis's preparation has been acknowledged. In addition, I certify that all information sources and literature used are indicated in the thesis.

This research is supported by an Australian Government Research Training Program.

Tuhin Subhra Sahu

Production Note:
Signature removed prior to publication.

02/12/2021

Dedicated to

My Parents

Acknowledgement

First and foremost, I wish to express my deep gratitude to my principal supervisor, Prof. Guoxiu Wang, director of the Centre for Clean Energy Technology, for his invaluable advice, encouragement, and constant support during my study at the University of Technology, Sydney (UTS). This thesis would not have been possible without his guidance and support.

I am grateful to Professor Arumugam Manthiram for his valuable guidance during my visit to The University of Texas at Austin. I am also thankful to Dr. Dong Zhou for being my co-supervisor and his constant help during my research work.

I cannot miss thanking Dr. Jane Yao. Her kind help and precious support are essential to my laboratory work.

Many thanks to my colleagues at UTS, Dr. Anjon Kumar Mondal, Dr. Bing Sun, Dr. Hao Liu, Mr. Xin Guo, Mr. Xiao Tang, Dr. Jianjun Song, Dr. Jinqiang Zhang, Dr. Yufei Zhao, Dr Katja Kretschmer, Dr Jing Xu, Dr. Dong Zhou, Dr. Huajun Tian, Miss Xiaochun Gao, Mr. Yi Chen, Mr. Kang Yan, who have not only provided helpful suggestions during my progress meetings/presentations but also offered all assistance whenever I asked. I am also very thankful to my friends in Austin, Mr. Amruth Bhargav, Dr. Jiarui He, Mr. Sanjay Nanda, Mr. Robert Pipes, Kevin, Mr. Abhay Gupta, Mr. Soham Aggarwal.

In addition, I acknowledge my gratitude to the administrative and technical support I received from Dr. Ronald Shimmon, Dr. Linda Xiao, Mr. Sorabh Jain, and Miss Emaly Black. Also, I would like to thank Mr. Hugo Celio for his support with XPS measurements while I was at The University of Texas at Austin.

I am also very thankful to Katie McBean, Mark Berkahn and Herbert Yuan from the MAU and Physics Research Labs in UTS for their help on material characterization.

The financial support from UTS and Australian Renewable Energy Agency (ARENA) to help finish my Ph.D. study are highly appreciated.

Last but not the least, I deeply indebted to my parents for providing boundless love and unconditional support throughout writing this thesis and my life in general.

Date : 08/05/2021

Tuhin Subhra Sahu
School of Mathematical and Physical Sciences
University of Technology Sydney
Sydney, Australia

RESEARCH PUBLICATIONS

1. **Sahu, T. S.**; Choi, S.; Jaumaux, P.; Zhang, J.; Wang, C. and Wang, G., Squalene-derived sulfur-rich copolymer@3D graphene-carbon nanotube network cathode for high-performance lithium-sulfur batteries. ***Polyhedron*** 2019, 162, 147-154.
2. **Sahu, T. S.**; Zhou, D.; Wang, G. and Manthiram, A., Multi-Application of Amine-functionalize Metal-Organic Frameworks in High-performance Alkali Metal-Sulfur Batteries. (***manuscript ready for submission***)
3. **Sahu. T. S.**; Wang, G. and Manthiram, A., Rationally Designed Freestanding Bilayer Cathode with Polar Electrocatalyst for Efficient Polysulfides Conversion and High-performance Li/Na-S Batteries. (***manuscript ready for submission***)
4. Shanmukaraj. D.; Kretschmer. K.; **Sahu. T.**; Bao. W.; Rojo. T.; Wang, G. and Armand, M., Highly Efficient, Cost-Effective, and Safe Sodiation Agent for High-Performance Sodium-Ion Batteries. ***Chem Sus Chem*** 2018, 11, 3286- 3291.

TABLE OF CONTENTS

LIST OF TABLES

LIST OF FIGURES

Abstract

Over the last decade demand for renewable energy technologies has been one of the primary issues of concern across the globe. It is in this context, lithium-sulfur battery based on sulfur cathode have drawn the particular interest owing to the high specific capacity, high energy density and low cost of eco-friendly sulfur. Nonetheless, there are still formidable challenges hindering the successful application of lithium-sulfur battery. Those challenges can be categorized as, poor electrical conductivity of elemental sulfur, lithium polysulfide intermediate dissolution / shuttling. In my doctoral work, I focused mainly on the cathodes, such as developing a new class of sulfur material and optimizing the cathode structure to improve the electrochemical performance of lithium-sulfur batteries.

The first part of the thesis, we report a novel sulfur rich copolymer@ 3D graphene-carbon nanotubes (G-CNT) network cathode for high performance lithium-sulfur batteries. Unlike elemental sulfur as cathode, this squalene-derived copolymer can greatly suppress the dissolution of sulfur and polysulfides due to the chemical confinement from the crosslinking of polysulfur chains with the squalene molecules. While in the SP@G-CNT composite electrode, the interlinked Sp^2 G-CNT network not only enhance the polysulfide entrapment capability, but also provide the composite with an 3D electrically conductive path as well as an eminent mechanical resilience towards the huge volume change of sulfur. The as-developed cathode can deliver a high specific capacity, excellent rate performance and cycling stability.

In the second part, a nitrogen-doped micro/mesoporous carbon is derived from an amine-functionalized metal oxide framework (UIO-66-NH_2 abbreviated as NH_2-MOF) to host sulfur. Moreover, a freestanding permselective membrane was fabricated by the layer-by-layer (LBL) assembly of NH_2-MOF and graphene oxides nanosheets and implicated as an interlayer. Such,

multifunctional interlayer can block the shuttling of polysulfides in both physical and chemical ways without compromising the ion conductivity. The optimized lithium-sulfur cells realized high reversible capacity, extended cycling stability at high rate and much improved rate performance.

In the third part, a well-designed bilayer cathode structure is proposed to increase the active material loading and improve the areal capacity. The support layer contains carbon nanofiber / nickel nanoparticles decorated nitrogen-doped graphene (Ni-NG) and the top layer composed of Ni-NG nanosheets. The porous and highly conductive bilayer host not only ameliorates high sulfur loading and increase active material utilization but also accelerates the rapid conversion of polysulfides. With Li_2S_6 catholyte, bilayer Ni-NG@CNF cathodes demonstrates low voltage polarization, superior cycling stability and excellent rate performance.

Introduction

Lithium-Sulfur (Li-S) battery is one of the most promising candidates for the next-generation energy storage devices, with high specific capacity (~1672 mAh g^{-1}), high theoretical energy density (2600 Wh kg^{-1}) and low cost.[1,2] However, the development and applications of Li-S battery have been severely hindered by the intrinsic poor electronic conductivity of sulfur and the rapid-capacity degradation due to dissolution of intermediate polysulfides into the electrolytes. [3]

Considerable efforts have been made to address the issues, including design of nanostructured cathode, optimization of electrolytes and protection of lithium anodes. One of the most common approaches in the cathode design is to utilize mesoporous carbonaceous materials as a potential host for sulfur. [4] Typically, a highly conductive carbon matrix can improve the charge transfer resistance of the cathode and the mesopores within the structure can be used to trap soluble lithium polysulfides physically. However, weak interaction between hydrophilic lithium polysulfides and the non-polar carbon surface often leads to out-diffusion of polar lithium polysulfides over extended cycling. [5] Recently, polar materials such as, hetero-atom doped carbon, [6,7] metal oxides/ sulphides/nitrides [8, 9, 10] have been explored extensively. Unlike non-polar carbon, the hydrophilic surfaces of these polar hosts can bind the migrating lithium polysulfides via hydrophilic surface interaction and improve the cyclability of Li-S system. As a replacement for elemental sulfur, polymers containing high content of organosulfur that is covalently bonded to the organic backbones have also been reported as an effective strategy to endow both physical and chemical confinements on the soluble lithium polysulfides intermediates. [11] Therefore, in a nut-shell an ideal sulfur cathode host should have: (i) highly porous structure to encapsulate sulfur; (ii) high electronic conductivity to improve the active material utilization; (iii) capability to restrain

polysulfides and (iv) flexible and robust physical properties to buffer the volume change of active materials during lithium insertion/extraction. [12]

Chapter 1 introduces the research development of lithium-sulfur batteries. The working principle, major challenges, and the ongoing approaches to overcome these challenges are presented in this chapter.

Chapter 2 briefs about the experimental section, which includes material preparation techniques, physiochemical characterizations of as-prepared materials and their electrochemical investigations. Various synthesis strategies, such as solid-state reaction and hydrothermal synthesis were mainly applied to prepare different electrode materials in this doctoral work. This chapter also briefly introduces the instrumental analysis techniques that have been used to characterize the as-prepared electrode materials, including X-ray diffraction (XRD), Raman Spectroscopy, thermogravimetric analysis, field emission scanning electron microscopy (FESEM), transmission electron microscopy (TEM), X-ray photoelectron spectroscopy (XPS), nitrogen adsorption-desorption, and Fourier transform infrared spectroscopy (FTIR). Cell assembly and electrochemical testing techniques, including cyclic voltammetry (CV) galvanostatic charge-discharge and electrochemical impedance spectroscopy (EIS) were also presented.

Chapter 3 presents synthesis of a novel sulfur-rich copolymer which is utilized as a new cathode active material for Li-S batteries. The sulfur-rich copolymer (87.29 % sulfur) synthesized by inverse vulcanization between two eco-friendly sources, sulfur and squalene. Covalent bonding between squalene (organic moiety) and sulfur molecules effectively suppresses the active material dissolution and migration during consecutive charge-discharge process. With such merit, the sulfur-rich copolymer (SP) demonstrates superior electrochemical performances as compared to that of elemental sulfur. For further improvement in electrochemical performances, SP was

combined with two-dimensional graphene (G) and three-dimensional graphene-carbon nanotubes (G-CNT) matrixes. The three-dimensional SP@ G-CNT composite shows high discharge capacity value (1265 mAh g^{-1} at 0.2 C), improved cycling stability (782 mAh g^{-1} at after 300 cycles at 1 C) and excellent rate performances compared to that of two-dimensional SP@G. This is attributed to the 3D interlinked Sp^2 G-CNT network, which not only improve the 3D electrically conductivity of the composite for better active material utilization, but also enhance the polysulfide entrapment capability and acts as a mechanical buffer against the huge volume change of active material.

Chapter 4 reports the synthesis of nitrogen-doped mesoporous carbon (NMC) with hierarchical pore architecture for high performance Li-S batteries. The materials contain nanopores (< 2 nm) and mesopores (2 – 4 nm), derived from carbonization of porous amine (NH_2)-functionalize metal organic frameworks (NH_2-MOFs). Subsequently, sublimed sulfur was infused into the porous NMC by simple melt-diffusion method. Through the synergistic effect of nanopores and mesopores, the porous matrix can endow an exceptionally high ion–accessible surface area and low ion diffusion barrier. This conductive host not only improve the active materials utilization but also alleviate the large volume change of sulfur during electrochemical reaction. Besides, the successful N-doping can provide an additional interaction to the migrating lithium polysulfides. Exploiting the interaction between amidogen (NH_2) groups of NH_2-MOFs and the surface functional groups of graphene oxide (GO), a layer-by-layer (LBL) assembled membrane (NH_2-MOF-GO) was prepared by simple vacuum filtration technique and was utilized as an interlayer in between the cathode and the separator (PP). This freestanding permselective membrane can interact to the migrating lithium polysulfides in both physical and chemical ways. Therefore, the newly configured interlayer suppresses the polysulfide migration and ensure the lithium anode stability. As a result, compared with the NMC-S/PP, this rationally designed NMC-S/NH_2-MOF-

GO cell shows an obviously improved electrochemical performance, including discharge capacity and high-capacity retention.

Chapter 5 elucidates a sophisticated bilayer cathode structure to increase the sulfur loading, active material utilization, and the enhanced areal capacity. A simple vacuum filtration technique was adopted to fabricate the freestanding and flexible bilayer cathode. Bottom layer of this cathode consists of carbon nanofiber (CNF) and nickel nanoparticles decorated with nitrogen-doped graphene (NiNG). The top layer is composed of only NiNG. The integrated CNF and NiNG matrixes in the bottom layer host the active material and ensure their high utilization efficiency. Besides, intertwined CNF network possesses abundant void spaces to buffer the volume expansion of the active material. With the presence of nickel nanoparticles, the top NiNG layer accelerates the polysulfide conversion kinetics and effectively block the polysulfide migration. To maximize the potential of this bilayer host, Li_2S_6 / electrolyte solution (catholyte) was used as active material due well-dispersibility of the catholyte and drop-casted onto bottom layer of the bilayer host. Benefitting from such advantageous structural features, the bilayer Li_2S_6-NiNG@CNF cathodes demonstrates low voltage polarization, improved cycling stability and excellent rate performance, including a reversible discharge capacity of 1272 mAh g^{-1} at 0.2 C rate, 89.4 % capacity retention after 100 cycles and discharge capacity of 848 mAh g^{-1} at 3 C current rate. In addition, high sulfur loading up to 8 mg cm^{-2} and an areal capacity of 6.8 mAh cm^{-2} were achieved at low electrolyte to sulfur (E/S) ratio of 7 µL mg^{-1}_{sulfur}.

Chapter 6 briefly summarizes the research outcomes of this thesis work and future perspective of cathode materials for Li-S batteries.

Chapter 1

Literature Review

The ever-growing demand for economic and efficient energy storage technologies has triggered the intensive exploration for advanced rechargeable battery technologies. To date, several kinds of rechargeable batteries have been reported and can be categorized as, (i) lithium ion-based rechargeable batteries; [13] (ii) sodium-ion based rechargeable batteries; [14] (iii) other metal-ion based batteries (magnesium ion secondary batteries and alkali metal-air secondary batteries); [15]and supercapacitors.[16] To date, there are mainly three types of lithium-ion based batteries have been reported, (i) Li-ion batteries (LIBs), (ii) Lithium-sulfur batteries (Li-S) and (iii) Li-oxygen batteries (Li-O_2). [17, 18] In this doctoral work, the research was mainly focused on designing novel sulfur cathodes with 'smart' nanostructures and their subsequent application in Li-S battery for improved electrochemical performances.

1.1 Rechargeable Lithium-ion Batteries

Li-ion battery (LIB) technologies have become an indispensable part of our day-to-day lives since they were first commercialised by Sony Inc. in 1991.[19] With the emergence of new portable electronic devices (i.e. mobile phones, laptops, tablets, cameras, drones etc) the consumption of LIB has increased significantly.[20, 21] The key factors that LIBs have attracted tremendous scientific interest as they have considerable energy density, long cycle life, low maintenance, no memory effect and low self-discharge.[22- 25] In most cases, a conventional LIBs implement Li-intercalating electrode materials to store electrical energy during charge, and releasing electrical energy on discharge.[26] The most common Li-ion electrode chemistry is a graphite/$LiCoO_2$.[27,28,29] A typical graphite/$LiCoO_2$ cell shown in **Figure1.1**, consists of four components, $LiCoO_2$ coated on aluminium current collector as positive electrode (cathode), a negative electrode (anode) made

from graphite coated on a copper current collector, an insulating separator and electrolyte made of Li-salt in a organic solvent.

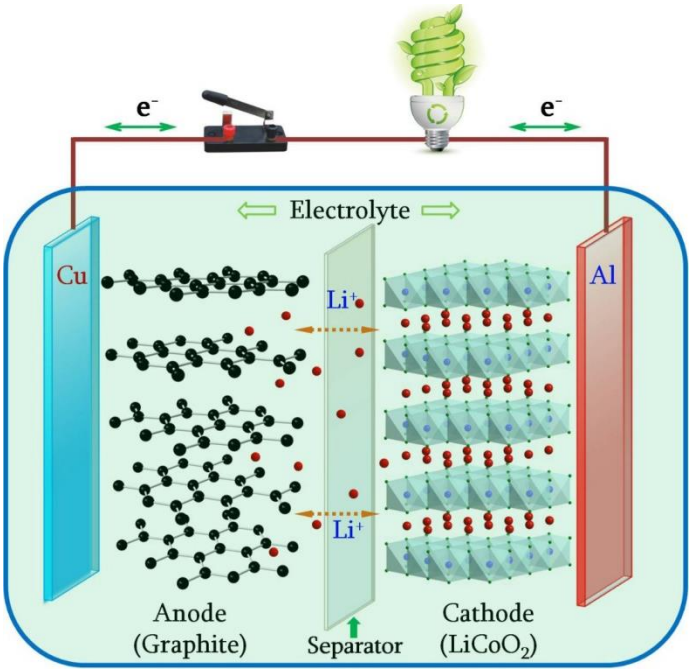

Figure 1.1 schematic diagram of the lithium intercalation/de-intercalation reaction mechanism in rechargeable LIBs.[13]

During Charging process, the $LiCoO_2$ is get oxidized to release a Li-ion from its solid lattice into the electrolyte and an electron that transfer via the external circuit to the anode. Meanwhile, graphite, the anode accepts a Li-ion and an electron in a reduction reaction, storing electrochemical energy within the battery in the form of chemical energy. When the cell is under discharged, the reverse occurs and the electrons flow in the opposite direction through the external circuit powering electrical devices.[13] The specific reactions corresponding to the charge and the discharge process are as follows:

$$C_6 + Li^+ + e^- \leftrightharpoons LiC_6 \quad (1)$$

$$LiCoO_2 \leftrightharpoons x\,Li^+ + x\,e^- + Li_{1-x}CoO_2 \quad (2)$$

However, based on such intercalation reactions, LIBs generally have an energy density of no higher than 200 Wh kg^{-1} and cannot match the requirements for the development of electric vehicles (EVs). [25,30,31] Owing to this inadequacy, advanced battery technologies with improved electrochemistry are crucial to offer high capacities and energy densities.

1.2 Rechargeable Lithium-Sulfur battery

Beyond intercalation-based LIBs, Li-S batteries have garnered much scientific interest in the recent years as the sulfur cathode delivers a high theorical capacity of ~1672 mAh g^{-1} (calculated based on $S^0 \leftrightarrow S^{2-}$) at an average operating potential of ~2.1 V vs. Li/Li^+, and a staggering energy density of ~ 2500 Wh kg^{-1}, which is 3-5 times higher than current Li-ion batteries. Moreover, the natural abundance, low cost, and environment benignity of sulfur make it an appealing material for the use in next generation Li-based batteries. [32,33,34]

1.2.1 Basic Principle of a Li-S battery

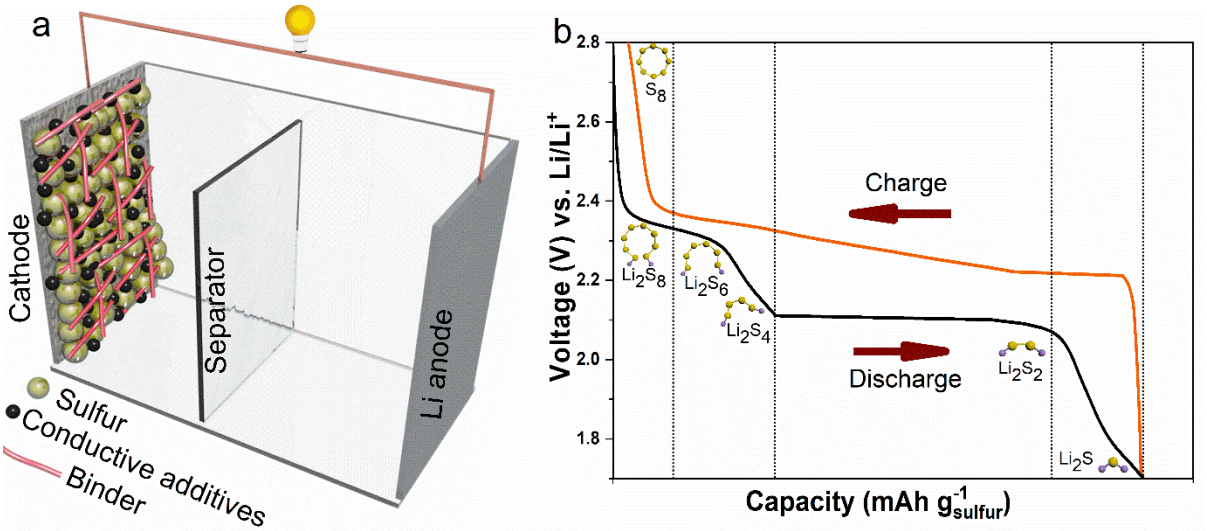

Figure 1.2 (a) Conventional cell configuration and (b) charge-discharge voltage profile of Li-S cell.

A typical Li-S battery is composed of a positive electrode (cathode) of sulfur (S_8) with a conductive additive and a polymer binder, a negative electrode (anode) of lithium metal separated by an insulating separator immersed with organic electrolyte (demonstrated in **Figure 1.2a**). [1]

During discharge process, oxidation takes place in the anode, where Li-metal is oxidised to produce electrons and Li-ions. The electrons then transfer through the load and reach cathode, where the sulfur gets reduced to lithium polysulfides (Li_2S_x, x = 4 - 8) by accepting electrons and Li-ions. Subsequently, the intermediate polysulfide (Li_2S_x, x = 4 - 8) further reduced to yield lithium sulfide (Li_2S) with a gradual decrease in the sulfur chain length. During cell charge, reverse phenomenon occurs where Li_2S is reversibly oxidized to S_8 after releasing electrons and Li-ions. Both of electrons and Li-ions travel back to the anode. [35- 40]

The overall reaction involves two electrons transfer per sulfur molecule and can be depicted as follows:

$$2\ S_8 + 16\ Li = 8\ Li_2S \qquad (3)$$

Despite seemingly simple electrochemistry, the actual electrochemical reaction is occurring in Li-S battery is complex and multi-stepped, which involves series of soluble polysulfide intermediates (Li_2S_x, $3 \leq x \leq 8$) and insoluble final product (S_8 or Li_2S_2/Li_2S). **Figure 1.2b** demonstrates typical discharge-charge process of an ideal Li-S cell. As it can be seen, the typical reduction (discharge) of elemental sulfur to Li_2S can be divided into three steps: (i) the upper plateau region at ~ 2.3 V (vs Li/Li^+), (ii) the sloping region between ~ 2.3 V – 2.1 V (vs Li/Li^+) and (iii) lower plateau region at ~ 2.1 V (vs Li/Li^+). [41,42]

In the first step at ~ 2.3 V, the cyclo-sulfur (S_8) will step-wisely reduced into high-order polysulfide S_6^{2-} by accepting two electrons as shown in equation (4) and (5).

$S_8 + 2e^- \longrightarrow S_8^{2-}$ (4)

$3\ S_8 + 2e^- \longrightarrow 4\ S_6^{2-}$ (5)

The high order polysulfides are highly soluble in organic electrolyte due to their high polarity and increase the viscosity of the electrolyte. As a result, diffusion overpotential and corresponding impedance raise a concentration polarization. This leads to voltage drop between 2.3 V to 2.1 V (vs Li/Li^+). During this process, S_6^{2-} is converted into S_4^{2-} as illustrated in equation (6).

$3\ S_6^{2-} + 2e^- \longrightarrow 3\ S_4^{2-}$ (6)

In the lower plateau region at ~2.1 V (vs Li/Li^+), S_4^{2-} will further reduced to insoluble solid Li_2S by accepting two additional electrons as demonstrated in equation (7) and (8).

$S_4^{2-} + 2e^- + 4\ Li+ \longrightarrow 2\ Li_2S_2$ (7)

$Li_2S_2 + 2e^- + 2\ Li+ \longrightarrow 2\ Li_2S$ (8)

It is worth to mention that, the reactions in the lower plateau are typical of solid-state reaction and occur in a much slower rate compared to the reactions takes place in the upper plateau.[43]

During charging, the charge curve shows two plateaus corresponding to stepwise oxidation of Li_2S into octa-sulfur via soluble polysulfide (Li_2S_x, $4 < x \leq 8$) intermediates.

The overall capacity of sulfur (S_8) cathode in Li-S battery can be quantified in following way:

The theoretical capacity of any element is = nF / atomic mass of that element

Where, n = number of electron transfer per atom

F = Faraday's Constant = 96485 Coulomb ≈ 26800 mAh

Theoretical capacity of lithium = $(1 \times 26800)/6.94 \approx 3862$ mAh g^{-1}

Theoretical capacity of sulfur = $(2 \times 26800)/32.065 \approx 1675$ mAh g^{-1}

Hence, the theoretical capacity of Li-S cell is,

$(1/Q) = (1/3861) + (1/1675)$; $Q \approx 1166$ mAh $g^{-1} \approx 1166$ Ah kg^{-1}

Since the average potential for Li-S discharge is 2.2 V.

So, average energy density of a Li-S battery is = (2.2 × 1166) ≈ 2600 Wh kg^{-1}.

1.3 Challenges of Li-S battery

Despite very high theoretical capacity, high energy densities, low-cost and environment benignity of sulfur, the potential application of Li-S battery is severely hindered by low sulfur utilization, poor cycling ability, low coulombic efficiency, low-rate capability and unsafe Li-metal. This can be ascribed to the following reasons:

1.3.1 Insulating nature of elemental sulfur and lithium sulfide

It is very essential for a cathode material to have high electrical and ionic conductivity, so that it can transport electrons and ions to keep the battery active. During discharge-charge process in Li-S system, the sulfur cathode must receive electrons from the external circuit and react with Li^+ ions for the reduction to occur. Unfortunately, the electrical conductivity of elemental sulfur at room temperature is 5 × 10^{-30} S cm^{-1}, which clearly indicates sulfur falls into category of insulating material. [44, 45, 46] Henceforth, conductive additives must be added to use sulfur as a cathode in Li-S system.

When sulfur is completely reduced, it forms Li_2S_2/Li_2S which are not only electronically insulating but also ionically insulating.[47, 48, 49] Therefore, after discharge, when it starts to be deposited on the cathode surface and forms a passivation layer, further lithiation will be largely impeded. This will lead to premature failure of the Li-S cells. Such problem can be possibly relieved by controlling the morphology and distribution of discharge products.

1.3.2 Volume Change

On account of different densities of sulfur (2.07 g cm^{-3}) and Li_2S (1.66 g cm^{-3}), the sulfur cathode undergoes 80% volume expansion upon lithiation.[50] Such repeated volume change of the cathode

during lithiation/de-lithiation can cause pulverization of the electrode and loss of electrical contact between the active materials and conductive surface. This leads to formation of isolated sulfur particles; those are very difficult to re-use. To counter this issue, the cathode should possess enough void space to accommodate large volume change of sulfur and maintain the structural integrity of the electrode. [51, 52, 53]

1.3.3 Polysulfide dissolution

Lithium polysulfides are (Li_2S_x, 4- x -8) the intermediate redox species generated during the discharge (reduction) process in Li-S battery. These liner chain polysulfides are highly soluble in organic solvent. Interestingly, the soluble nature of polysulfides into the electrolyte has dual-effects in the lithium-sulfur batteries. In one aspect, the dissolution of polysulfides is crucial to improve the active material utilization. [54, 55]As polysulfides continuously dissolved into electrolyte, the inner core of the non-conductive bulk sulfur particle will get exposed to the lithium ions /electrolyte, resulting in an enhancement of active materials utilization. [56]

However, such dissolution behaviour also causes several problems in Li-S batteries with a standard cell configuration. For instance, during discharge process the high-order polysulfides get dissolve into the electrolyte, pass through the separator, and are deposited on the lithium-metal surface that further block the access of electrolyte.[57, 58, 59] Such migration behaviour is controlled by (i) concentration difference of polysulfides between the cathodic and the anodic compartments, and (ii) chemical potential. [60, 34] This adverse effect brings unexpected self-discharge, irreversible loss of active materials and severe capacity decay in lithium-sulfur cells. Therefore, restraining the migrating polysulfides within the sulfur cathode and inhibiting their diffusion to lithium anode side is crucial to improve the electrochemical performance. [61- 73]

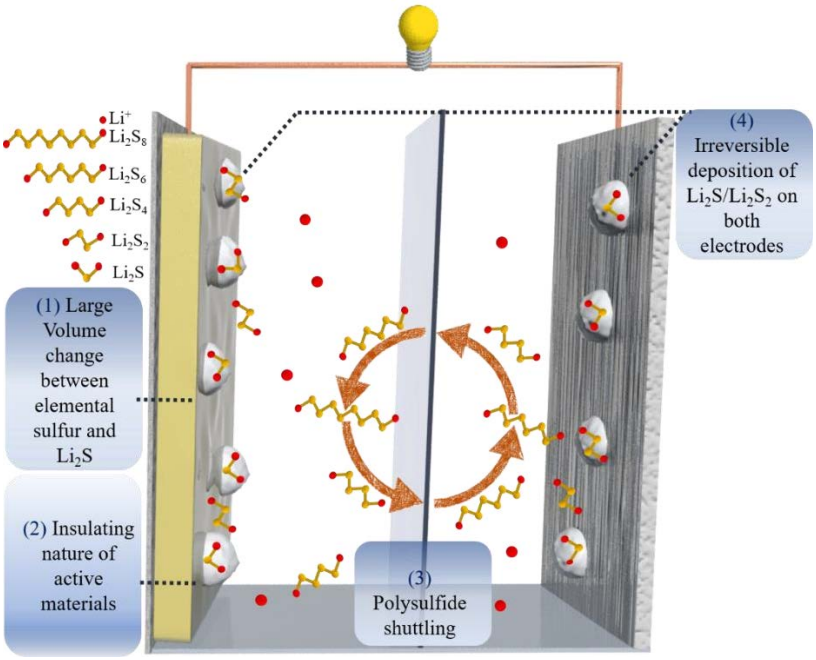

Figure 1.3 Schematic illustration of Li-S cell with four main challenges.

1.3.4 Shuttle Effect

The shuttle effect originates from the free migration of dissolved lithium polysulfides between the cathode and the anode. The high-order polysulfides (Li_2S_x, $6< x \leq 8$) diffuse through the separator and are reduced to low-order polysulfides (Li_2S_x, $2< x \leq 6$) after reacting with the lithium anode. This low-order polysulfide can diffuse back to the cathode side and be oxidized to high-order polysulfides. This parasitic process takes place in a repeated manner, causing low coulombic efficiency and anode corrosion. Recently, the addition of $LiNO_3$ as an electrolyte additive has been shown to passivate the lithium anode from side reactions with polysulfides. [74- 78]

1.3.5 Self-discharge

Even when the lithium-sulfur cell is resting, the self-discharge takes place and form soluble polysulfides. Now, the dissolved polysulfides gradually diffuses into anodic side due to concentration gradient and reacts with the lithium anode. This will result decrease in open circuit voltage (OCV) and discharge capacity of the affected Li-S cell. [79]

1.4 Current Approaches on Cathode

The improvement in electrochemical performance of a Li-S cell heavily relies on the optimization within the cathode configuration. In general, a sulfur cathode composed of sulfur, a conductive additive and a polymeric binder. The poor electronic conductivity of sulfur and dissolution of intermediate polysulfides are major concerns to deal with. Therefore, a practical cathode design should include, (i) abundant pores to host sulfur and boost the ion transfer; (ii) high electronic conductivity to improve sulfur usage; (iii) capability of restraining polysulfides within its microstructure; (iv) mechanical resilience against volume charge of active materials. [4, 12, 59, 62, 80, 81, 82]

1.4.1 Porous Carbon Materials

Due to low density, low cost, excellent electrical conductivity and inertness over extended voltage window, carbon materials have been widely used as conductive additives for Li-S battery. [83, 93] In the early stage of Li-S research, the sulfur was physically mixed with carbon by ball milling process. [94] Despite the simplicity, the microscopic isolation of sulfur and carbon particles after such treatment will leads to poor electronic conductivity and low sulfur utilization. The first breakthrough was achieved in 2009, when Nazar and co-workers infused sulfur into the mesoporous carbon by melt-diffusion technique at 155 ˚C. [4] Typically, at 155 ˚C molten sulfur can be infused inside the mesoporous channels of CMK-3, enabling sulfur to possess an intimate contact with the conductive carbon surfaces. By utilizing micropores (~2nm) for polysulfide retention and mesopores (~ 6nm) for electrolyte infiltration, CMK-3@S composite delivered high specific capacity of 1005 mAh g^{-1} with cycling over 20 cycle at 0.1 C.

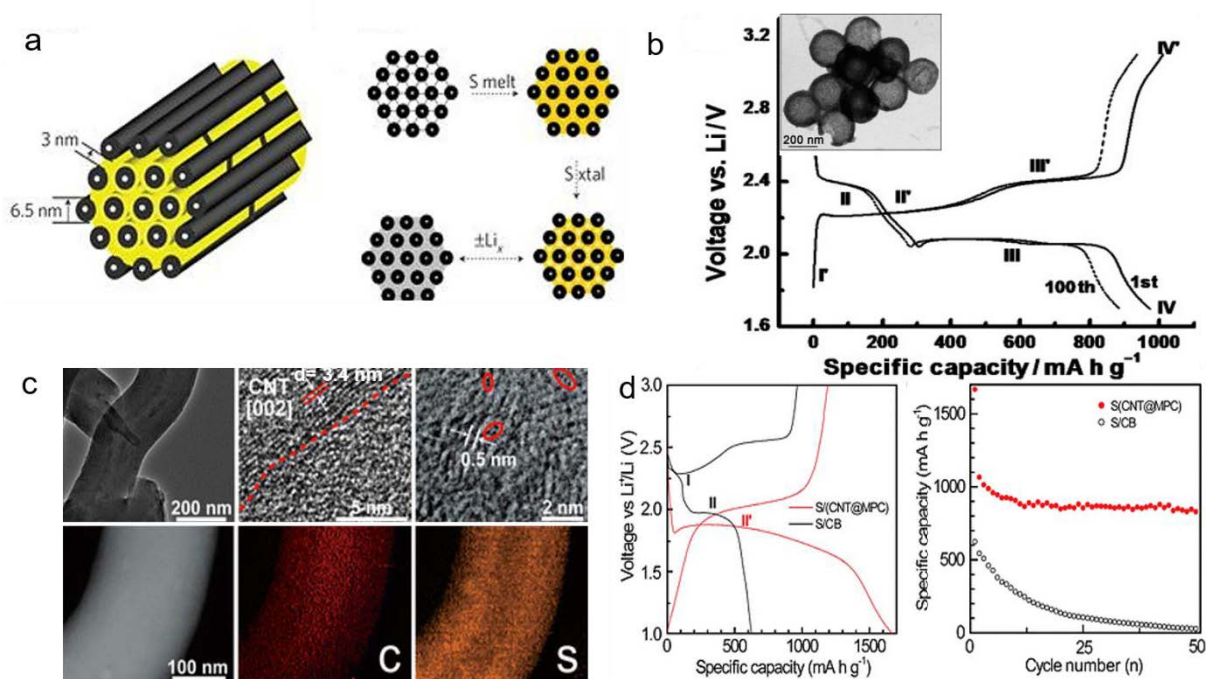

Figure 1.4 (a) Schematic illustration of CMK-3/S composite where sulfur (yellow) is impregnated into interconnected pores of CMK-3 host by melt-diffusion process. [4] (b) TEM images of Mesoporous carbon hollow sphere-sulfur (C@S) composite and corresponding discharge-charge profile at 0.5 C rate. [95] (c) TEM, HR-TEM and EDX mapping of S(CNT@MPC) composite with smaller sulfur allotropes (S_{2-4}). (d) galvanostatic discharge profile of S(CNT@MPC) composite demonstrates different electrochemistry than S/CB composite. [96]

Jayprakash *et al*. reported the synthesis of mesoporous carbon spheres to encapsulate sulfur through vapour deposition into the interior and the porous wall. [95] Such vaporization technique will instigate the molecular level contact between insulating sulfur and conductive carbon. Furthermore, the outer shell minimizes the polysulfide dissolution and allows easy access to electrolyte. With Such rationally designed structure this porous hollow carbon@sulfur composite cathode provided a high capacity of 1000 mAh g^{-1} stable up to 100 cycles. On the other hand, Xin et al. confined metastable small sulfur (S_{2-4}) molecules inside ~0.5 nm pores of a microporous

carbon matrix (shown in **Figure 1.4c**). [96] With this strategy, the transition from S_8 to S_4^{2-} can be avoided entirely. With different electrochemistry (**Figure 1.4d**), the composite electrode showed much higher capacity and stable cycling performance over bulk carbon black-sulfur (CB-S) composite. Nonetheless, the disadvantage is that it is difficult to completely confine sulfur inside micropores and the sulfur remaining outside.

1.4.2 Hetero atom-doped Porous Carbon Materials

Another approach to dope hetero atoms, such as nitrogen/ sulfur / phosphorous on porous carbon network have also been thoroughly investigated. There are two main advantages of heteroatom-doped carbon has been reported in literature. Firstly, the improved electronic conductivity of the doped carbon, leading to high sulfur utilization. Secondly, the dopant sites could restrain the polusulfides from migrating towards anode and result a stable cycling performance. Brezesinski et al. have synthesized a monolithic N-doped carbon from ionic liquid using as a carbon precursor. [97] With 1 mg cm^{-2} sulfur loading, this lightweight and mechanically robust cathode delivered a high discharge capacity of 1450 mAh g^{-1} during first discharge at C/50. However, with high sulfur loading (4 mg cm^{-2}), the issue of polysulfide dissolution and rapid fall of capacity were persisted. Later, Nazar et al. have infused sulfur into N, S-doped mesoporous carbon nanosheets. [6] To further understand the detailed interaction between hetero atoms on carbon surface and Li_2S_2, ab initio calculation was performed which showed that the binding energy (E_b) was significantly increased when N and S were simultaneous doped on the carbon network. Using this dual-doped carbon as sulfur host, the composite cathode has delivered a high charge/ discharge capacity (1372 mAh g^{-1} at C/20) and excellent cycling stability (0.052 % capacity decay per cycle for 1100 cycles).

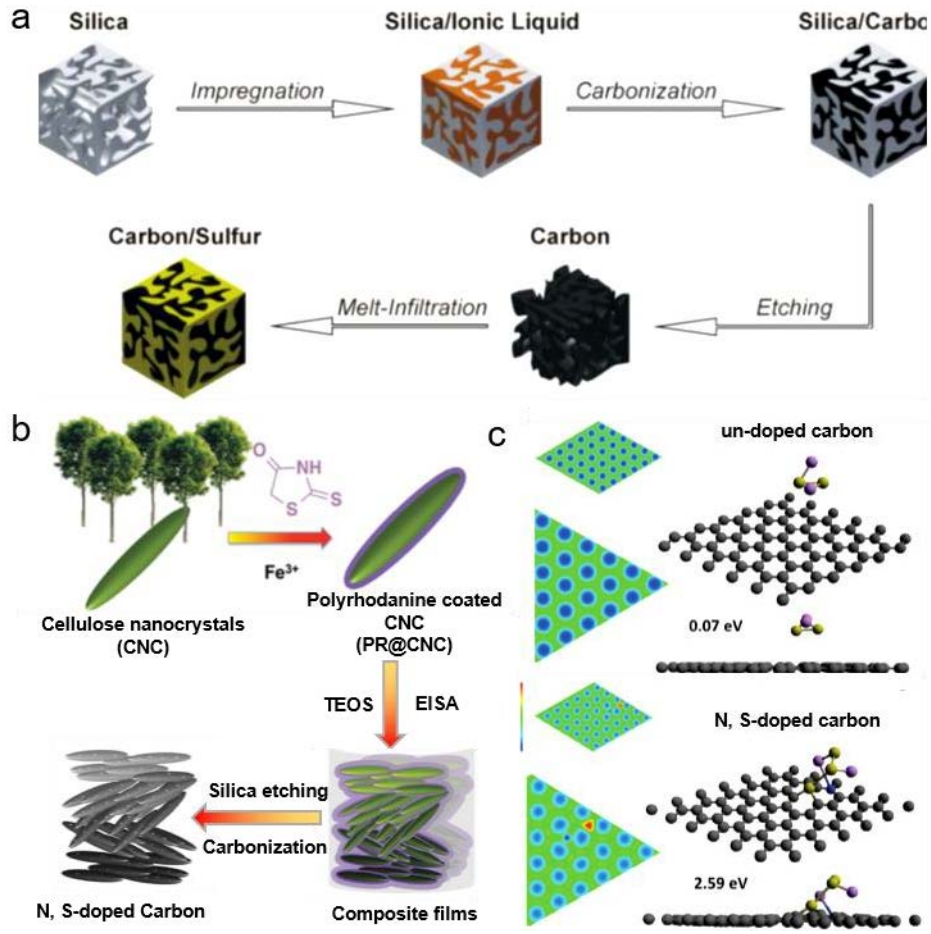

Figure 1.5 (a) Schematic diagram of ionic liquid assisted synthesis of N-doped carbon using mesoporous silica as sacrificial template. [97] (b) Schematic illustration for synthesis of N, S co-doped porous carbon. (c) ab initio calculation of binding energies between Li_2S_2 and as-prepared hosts. [6]

1.4.3 Graphene Based Materials

Since the exploration of graphene in 2004, this two-dimensional carbon allotrope has been applied extensively in the field of energy storage due to the superior electrical conductivity, high surface area and excellent mechanical durability. [98, 99, 100] There are basically two ways to exploit graphene in a sulfur cathode. One approach is the use of graphene as a host for sulfur. In this technique, sulfur is coated on the graphene surfaces by some physical or chemical methods. Wang

et al. followed two steps process to coat sulfur on the graphene. [101] First, they simply mixed sulfur and graphene by mechanical mixing and then thermally treated the mixture at 200 ˚C for 6 hours. Despite some improvements, it is difficult to control the uniformity of sulfur distribution on the graphene surfaces by simple mechanical mixing and heating techniques. This could result agglomeration of sulfur particle and obvious dwindling of capacity. Another approach to coat sulfur on graphene is a wet chemical route. A uniform sulfur/graphene composite has been prepared treating graphene oxide with a sulfur-containing compound in presence of sodium thiosulfate / sodium sulphide. [102] The graphene oxide first converted to sulfur-modified graphene oxide by hydrophilic interaction between graphene oxide and S^{2-} form $Na_2S_2O_3$ and Na_2S. Then, elemental sulfur will uniformly be deposited on the graphene surface upon addition of sulfuric acid. This composite delivered a specific capacity of 800 mA h g^{-1} at a specific current of 312 mA g^{-1}. Nevertheless, such coating techniques are not effective enough to prevent polysulfide dissolution. The sulfur is directly exposed to the electrolyte and therefore, the intermediate polysulfides get dissolved into the electrolyte upon discharge. Another effective strategy is to wrap sulfur particles with graphene nanosheets. Wang *et al*. reported synthesis of a core-shell type graphene-sulfur composite material by wrapping poly (ethylene glycol) (PEG) coated sub-micron sulfur particle as a cathode for Li-S battery. [103]The PEG and graphene coating layers not only help to alleviate volume expansion of sulfur, but also trap the intermediate polysulfides inside the core-shell structure. As a result, the graphene-wrapped sulfur particles delivered a high and stable capacity up to 100 cycles. However, it is difficult to control the size of sulfur particles deposited during the wet-chemical synthesis. Submicrometer-sized sulfur particle could increase the charge transfer resistance of the composite and result poor electrochemical performance. On the other hand, smaller sulfur particles were also reported using large quantity of surfactants. Nonetheless, removal of the surfactant molecules from the sulfur surfaces is tedious and

time consuming. If not completely removed, those insulating surfactants could block the electron transfer between sulfur and conductive graphene. More importantly, physical interaction between graphene surface and polar polysulfides is not effective enough to suppress the shuttling effect. In 2014, Lou et al. have introduced amino-functionalized graphene as a natural immobilizer for lithium polysulfides. The amine group contain two electron-doating lone pairs and has strong affinity towards the polar lithium polysulfides. [104] While the conductive graphene network maintains the continuous flow of electrons during electrochemical process. With such unique structure, the sulfur nanocomposite has delivered a high discharge capacity of 812 mAh g^{-1} during first discharge and retain 80% of the initial capacity after 350 cycles. However, introduction of such organic functionalities to reduced graphene oxide structure would limit its electronic conductivity to certain extent.

1.4.4 Polar Materials and Electrocatalysts

Recently, intensive work has been done on introduction of polar materials in Li-S batteries owing to their unique physical and chemical characteristics. Typically, a polar molecule possesses an electric dipoles or multipoles that originated from the separation of electrical charges within its structure. Because of the difference in electronegativity between two bonded atoms, a polar molecule must contain polar bond. Moreover, polar molecules could interact with each other through strong dipole-dipole intermolecular forces and hydrogen bonds. The lithium polysulfide species belong to class of polar molecules due to charge separation of positively charge Li^+ and negative S_n^{2-} moiety. Therefore, the chemical affinity in polar-polar interaction between polar lithium polysulfides and a polar molecule is more favourable. Cui et al. designed a sulfur-TiO_2-yolk-shell nanoarchitecture as shown in **Figure 1.6a**.[50]

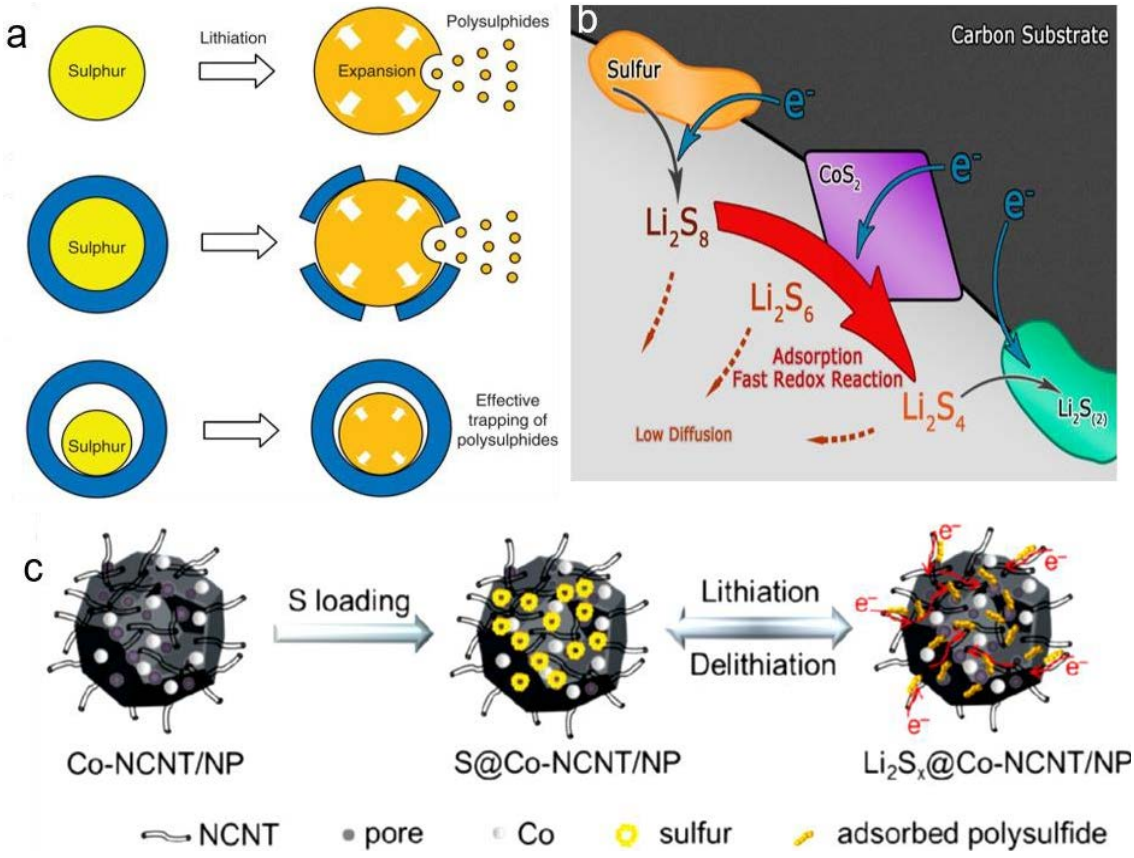

Figure 1.6 (a) Hollow and yolk-shell type TiO_2 host applied for sulfur composite. [50] (b) Schematic illustration showing CoS_2 mediated catalysation of long chain polysulfides. [112] (c) MOF-derived porous carbon host for sulfur composite. Present cobalt nanoparticles can participate as an electrocatalyst for polysulfide conversion. [113]

Here, the yolk sulfur is protected by the TiO_2 shell. This unique yolk-shell structure could supply enough internal void space to accommodate the volume change of sulfur. The hydrophilic Ti-O bonds and the surface hydroxyl groups provide additional interaction to the migrating polysulfides. The as-designed sulfur cathode delivered high specific capacity and cycling stability for 1000 discharge-charge cycles. A wide range of metal oxides composites have been used as sulfur host to trap the polysulfides, such as Nb_2O_5, [105] Fe_3O_4, [106], MnO_2, [107] MoO_2 [108] etc. Based on such polar-polar interaction concept, other polar materials have also drawn extensive attention such as MoS_2,[109] VS_2,[110] and TiN-VN [111] On

the other hand, electrocatalyst is a class of polar material that accelerate the kinetics of polysulfide conversion reaction. As a result of this, there will be less chances for polysulfides to accumulate or escape from cathodic compartment. Yuan et al. have introduced pyrite CoS_2 into graphene/ sulfur composite. [112] The half-metallic CoS_2 not only showed a strong affinity to polysulfides but also accelerated the charge transfer at the CoS_2/polysulfide interface (schematically illustrated in **Figure 1.6b**). With 75 wt.% sulfur, the graphene/CoS_2 composite exhibited a high initial capacity of 1368 mAh g^{-1} at 0.5 C and excellent cycling performance. Liu et al. used bimetallic metal oxide framework (ZnCo-ZIF) derived "sea urchin"- like Co nanoparticles embedded nitrogen-doped nanopolyhedra (Co-NCNT/NP) as sulfur host (**Figure 1.6c**).[113] The hierarchical porous cathode not only facilitate the ion/electron transfer but also restrain polysulfide. Moreover, the remaining encapsulated Co nanoparticles and high doping content of nitrogen species can promote the redox conversion of long chain polysulfides. On this basis, different metal nanoparticles such as, Pt, Ni have also been reported as a catalyst for polysulfide conversion reaction. [114, 115]

1.4.5 Organosulfur polymer

Apart from elemental sulfur, utilizing organosulfur polymer as an active cathode material in Li-S battery have also been reported as an effective strategy. The organosulfur were prepared by simple copolymerization process called "inverse vulcanization" between elemental sulfur and polymerizable linker monomer. Under normal condition, sulfur mainly exists in its most stable octa-atomic cyclic form (S_8). Once heated above its floor temperature (~ 159 ˚C), S_8 molecule undergoes a ring opening polymerization (ROP) reaction to yield polysulfane diradicals (**Figure 1.7a**). In presence of suitable linker monomer, the polysulfane diradicals could undergo a polymerization reaction to form chemically stable organosulfur polymer. The unique advantage of the sulfur copolymer lies in the presence of covalent bond between sulfur chains and organic

linkers, thus effectively suppressing the dissolution of polysulfide into the electrolytes. Pyun *et al*. directly copolymerized elemental sulfur with diisopropyl benzene (DIB) monomer at ~ 185 ˚C without any initiator or organic solvent, as shown in **Figure 1.7b**. [11]

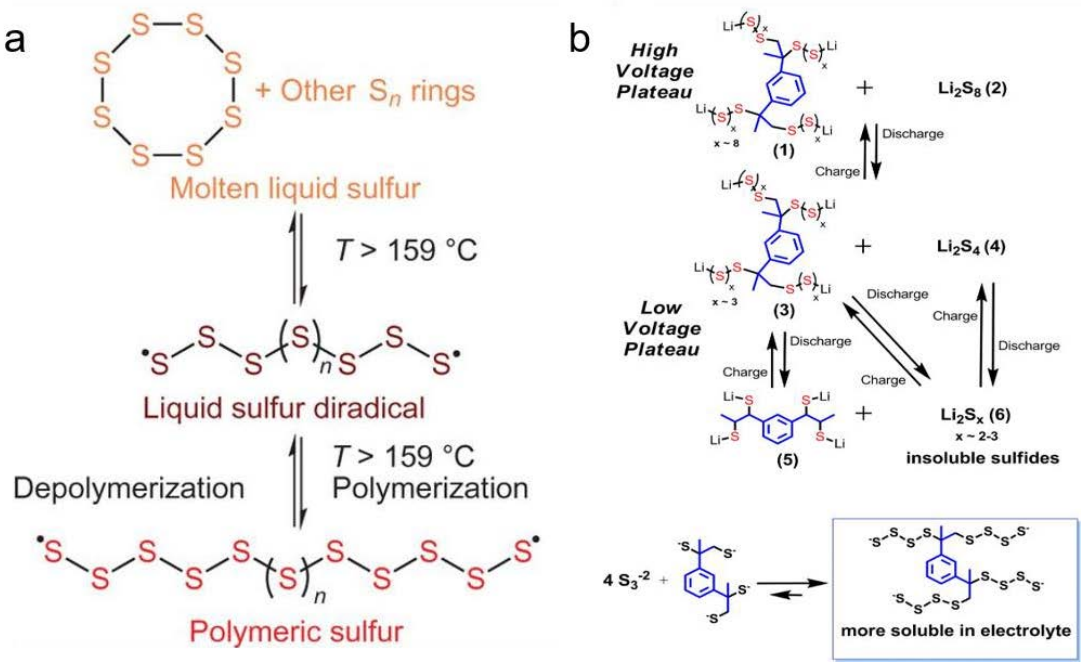

Figure 1.7 (a) Schematic illustration of S_8 ring opening mechanism above 159 ˚C. [11] (b) reaction mechanism of DIB-based sulfur copolymer as Li-S cathode during discharging and charging. [116]

When applied as cathode in Li-S battery, the copolymer showed high capacity and improved cycling stability compared to traditional sulfur cathode. The electrochemical activity of such organosulfur compounds is very similar to conventional sulfur cathodes. Upon discharge, the copolymer units go through high-order, low-order and fully discharged stages, as shown in **Figure 1.7b**. [116] A few other monomers were attempted for inverse vulcanization such as, thiocyanuric acid, [117] 1,4-diphenylbutadiyene, [118] benzoxazine. [119] However, like elemental sulfur, these sulfur-rich copolymers are insulating in nature and demands large quantity of conductive additives to be composited with to perform well in Li-S battery.

1.4.6 Polysulfide catholyte

The concept of using Li-soluble polysulfides (Li_2S_x) as an active material in Li-S battery was first introduced by Rauh *et al*. in 1979. [54] The polysulfide catholyte was prepared by adding stoichiometric amount of sulfur and lithium sulfide (Li_2S) into a mixed solution of $LiAsF_6$ in THF organic electrolyte. The soluble polysulfide catholytes are highly reactive as compared to the solid sulfur particles. As a result, a high capacity about 1.83 electrons per sulfur atom were achieved with those catholytes.

1.4.7 Interlayer / Separator Design

The notorious shuttling effect in Li-S cell can be eliminated by inserting a freestanding interlayer between the cathode and the existing separator. The idea of utilizing an interlayer was first introduced by Manthiram et al. In their work they prepared the freestanding multi-walled carbon nanotube (MWCNT) interlayer by ultrasonicating MWCNT dispersion, followed by simple vacuum filtration technique. This porous interlayer not only render a superior electronic conductive network, but also high mechanical strength to stabilize the cathode structure. As a result, the newly configured Li-S cell demonstrated very high specific capacity and excellent cycling stability for 100 cycles. A schematic diagram in **Figure 1.8a** shows the improvement mechanism of Li-S battery performances without and with SWCNT-modulated separator. [120] Kim et al. fabricated a CNT- loaded glass-filter composite (GF/CNT) by simple sonication method (**Figure 1.8b**). [121] According to the report, the interlocking fibre network of GF can restrain the escaping polysulfide, while interwoven CNTs inside GF network will maintain the continuous electron flow to ensure the reactivation of trapped polysulfides.

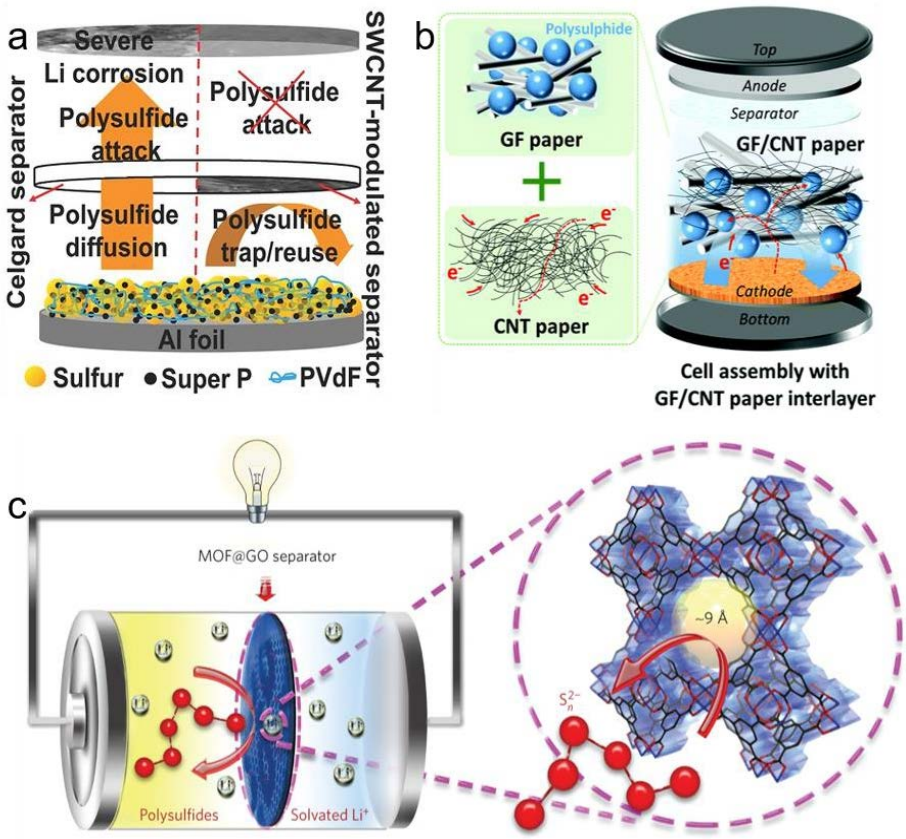

Figure 1.8 (a) Schematic diagram showing electrochemical performance enhancement mechanism of Li-S batteries with and without SWCNT-modulated separator. [120] (b) Schematic of CNT modified glassier separator for Li-S battery. [121] (c) Schematic diagram of re-configured Li-S cell with MOF@GO separator. [122]

Regarding the separator, Zhou *et al.* adopted a unique approach by combining the metal oxide framework (HUKST-1) with graphene oxide (MOF@GO) and fabricated a freestanding MOF@GO separator by simple vacuum filtration. [122] The three-dimension channel structure of this MOF contains micropores of size ~ 9 Å, which is less than the diameter of high-order polysulfides (Li_2S_n, $4 \leq n \leq 8$); thus, it is well suited as a physical barrier against polysulfide migration. On the other hand, GO will induce enough mechanical strength to maintain structural integrity of the separator before / after cycling. With this "smart" cell configuration, CMK-3/S

cathode delivered an average discharge capacity 813 mAh g^{-1} at 0.5C. However, sulfur loading in this study was as low as 0.6 -0.8 mg cm^{-2} and more importantly, lack of surface functionality could cause bulk diffusion of polysulfides during extended cycling.

1.4.8 Optimization of Electrolyte

Electrolyte is an indispensable part of a battery system as it helps to flow of Li^+ ions in between two electrodes. However, the role of electrolytes is far greater than simply Li^+ conduction. The kind of passivation layers it forms on electrolyte-anode anode interfaces also dictates the electrochemical performance of the cell. In Li-S, ether-based liquid electrolytes, such as dimethyl ether (DME), 1,3-dioxolane (DOL) are commonly used. Lithium polysulfides are highly soluble in.

1.4.9 Anode Protection

Lithium metal is the mainly used anode in Li-S batteries due to its high oxidation potential, high specific capacity, and high gravimetric energy density. However, there are several challenges remain with the lithium anode regarding its stability and safety issues when applied in Li-S cells. The major problem is the deposition of lithium polysulfides on the surface of lithium anode. Such passivation layer could block the ion/electron transfer and initiate the shuttle phenomenon. In addition, the lithium dendrites can form and penetrate through the separator, causing short circuit of the cell, and even fire in some extreme cases. A pioneer research was conducted by Lee *et al*. by creating a protection layer on the lithium metal surface using a UV cured polymerization method. In their report, the Li-S cell with protected lithium anode and liquid electrolyte demonstrated stable capacity compared to bare lithium anode due to the stable soild electrolyte interface (SEI) formation. Adding $LiNO_3$ as an electrolyte additive is another approach to stabilize the anode by forming a stable passivating layer on the anode surface. X-ray photoelectron spectroscopy (XPS) study revealed that $LiNO_3$ is converted into Li_xSO_y in presence of lithium polysulfide. Therefore, during the passivation process, lithium polysulfides

(or possibly Li_2S) is consumed to form the passivation film and shuttle phenomenon could be inhibited. [123]

1.5 Summery

Although the invention of Li-S battery can be traced back in 1962 by Herbet and Ulam, the practical applications of Li-S battery have been facing serious challenges from the low sulfur utilization, polysulfide dissolution and shuttling. To counter these issues, different cathode designs have been reported by scientist in last 10 years. However, polysulfide dissolution and shuttling issues still exist and need to be overcome.

1.6 Thesis Scope

The doctoral research will be focused on development of unique cathode materials for high active material utilization, to eliminate the lithium polysulfide dissolution / migration and to realize improved electrochemical performances of Li-S battery. ***Chapter 1*** introduced a comprehensive literature review on Li-S battery, particularly on Li-S cathodes. ***Chapter 2*** described the experimental details and physiochemical characterization techniques used in this doctoral work. ***Chapter 3*** examined the synthesis of a novel sulfur-rich copolymer and its composite with 3D graphene-carbon nanotube network for improved electrochemical performance. ***Chapter 4*** presented the synthesis of N-doped porous carbon derived from an amine functionalized metal oxide framework (NH_2-MOF) as a host for active materials and a NH_2-MOF @graphene oxide interlayer and improved electrochemical performance. ***Chapter 5*** introduced a freestanding bilayer cathode composed of carbon nanofiber (CNF) and nickel nanoparticles grafted on nitrogen-doped graphene architecture for high sulfur loading and high areal capacity cathode. ***Chapter 6*** briefly summarized the results of this doctoral work and future perspective of cathode materials for Li-S batteries.

Experimental

2.1 Overview

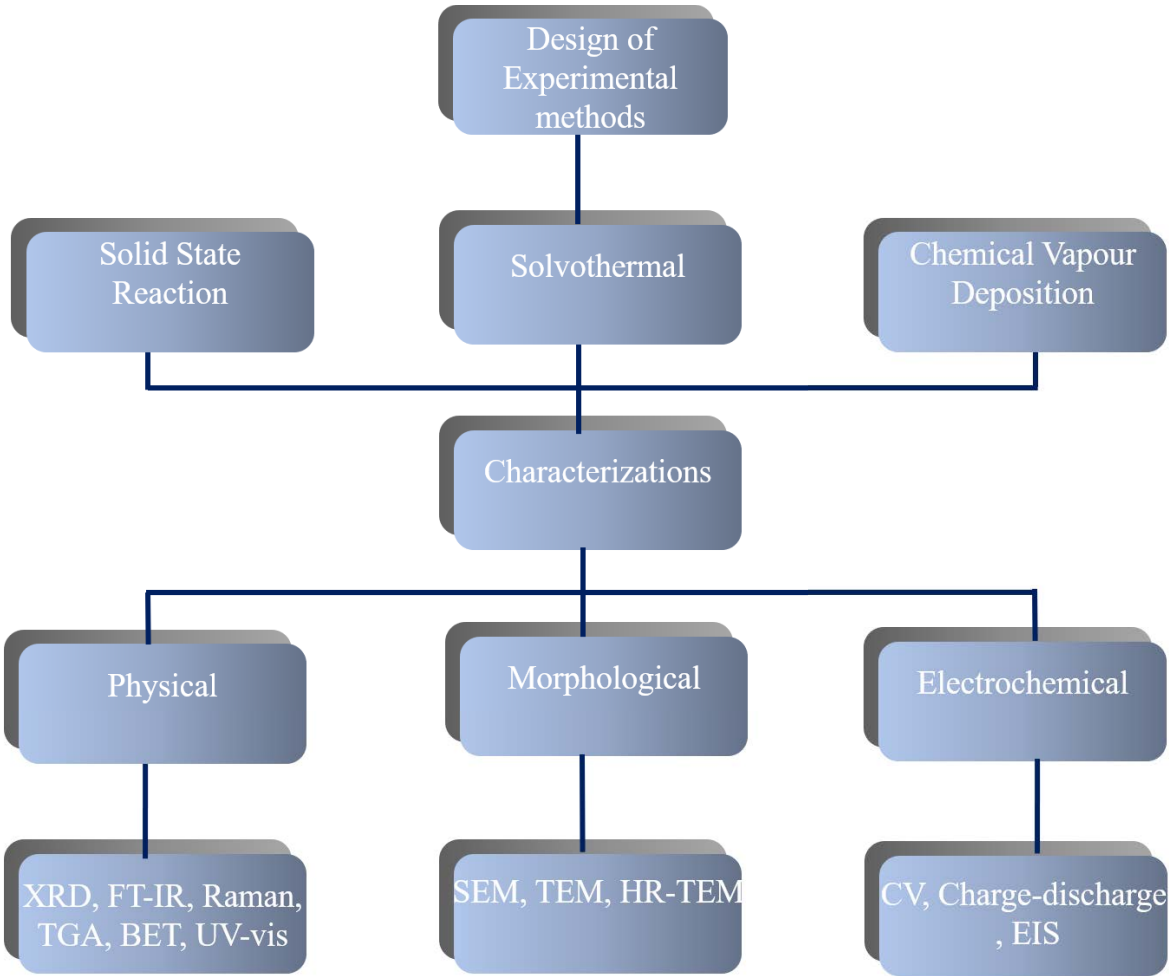

Figure 2.1 Framework of the experimental details.

The experimental synthetic approach of as-prepared nanomaterials, as well as physical and electrochemical characterization techniques are outlined in **Figure 2.1**. In detail, which include:

(i) Sophisticated electrode materials were prepared by different synthesis methods, such as chemical vapour deposition (CVD), solid state synthesis, solvothermal methods. All chemicals and materials that have been used during the experiments are listed in **Table 2.1.**

(ii) The physical and chemical properties of as-prepared electrode materials, such as nanostructure, morphology, chemical bonding, surface area and porosity were determined by X-ray diffraction spectroscopy (XRD), Raman spectroscopy, Fourier transformed infrared spectroscopy (FT-IR), thermogravimetric analysis (TGA), scanning electron microscopy (SEM), energy dispersive X-ray spectroscopy (EDX), transmission electron microscopy (TEM), high-resolution TEM (HRTEM), Brunauer Emmett Teller (BET), X-ray photo electron spectroscopy (XPS), ultraviolet visible spectroscopy (UV-vis). Finally, the as-prepared materials are assembled as cathode in an Argon-filled glove box and subjected to variety of electrochemical testing for Li-S battery applications. The common electrochemical characterization techniques are cyclic voltammetry (CV), galvanostatic charge-discharge, cycling performance, rate performance (cycling at different current densities), electrochemical impedance spectroscopy (EIS).

Table 2.1 List of Chemicals with formula, purity, and supplier.

Chemicals	Formula	Purity	Supplier
Carbon black	C	99 %	Sigma-Aldrich
Poly(vinylidene difluoride) (PVdF)	$(CH_2CF_2)_n$	-	Sigma-Aldrich
Polytetrafluoroethylene (PTFE)	$(C_2F_4)_n$	-	Sigma-Aldrich
Sulfur	S	99 %	Sigma-Aldrich
Ethanol	CH_3CH_2OH	95 %	Chem Supply
1, 3 -dioxolane	$C_3H_6O_2$	99 %	Sigma-Aldrich
Graphite (natural flakes)	C	75 %	Sigma-Aldrich
Orthophosphoric acid	H_3PO_4	85%	Chem Supply
Sulfuric Acid	H_2SO_4	98%	Chem Supply
Hydrogen peroxide solution	H_2O_2	50 %	Sigma-Aldrich
Lithium nitrate	$LiNO_3$	99.9 %	Sigma-Aldrich
N-methyl pyrrolidinone (NMP, anhydrous)	C_5H_9NO	99.5 %	Sigma-Aldrich
Terephthalic acid	C_6H_4-1,4-$(CO_2H)_2$	99 %	Sigma-Aldrich
2-aminoterephthalic acid	H_2N-C_6H_4-1,4-$(CO_2H)_2$	99 %	Sigma-Aldrich
Potassium permanganate	$KMnO_4$	99 %	Sigma-Aldrich
Lithium foil	Li	99.999 %	Hohsen Corporation Japan
1, 2 -dimethoxyethane	$CH_3CH(OCH_3)_2$	99.7 %	Sigma-Aldrich
Polypropylene separator	$(C_3H_6)_n$	100 %	Celgard
Zirconium (IV) chloride	ZrCl4	99.9 %	Sigma-Aldrich
Dimethylformamide (DMF)	$HCON(CH_3)_2$	99 %	Sigma-Aldrich

Chemicals	Formula	Purity	Supplier
Acetic acid	$C_2H_4O_2$	99.7 %	Chem Supply
Squalene	$C_{30}H_{50}$	98 %	Sigma-Aldrich
Carbon Nanofiber	C	99 %	Sigma-Aldrich
Nickel Nitrate hexahydrate	Ni $(NO_3)_2$, 6 H_2O	99.9 %	Sigma-Aldrich
Propan-2-ol	C_2H_7O	95 %	Fisher Scientific
Lithium bis (trifluoromethane sulfonel) imide	LiTFSI	99.95%	Sigma-Aldrich
Graphite (natural flakes)	C	75 %	Sigma-Aldrich
Hydrofluoric acid	HF	48 %	Sigma-Aldrich

2.2 Materials Synthesis

2.2.1 Solvothermal Process

Solvothermal method is one of the most used techniques for the synthesis of advanced nanostructured materials. The advantage of this method lies in precise control over the morphology, size, and crystallinity of the nano structure product. In a typical procedure, the precursors and other reagent, including the solvent, are loaded in a Teflon liner protected by a thick stainless-steel cover and heated (typically < 250 ˚C) in an air oven for fixed period. During this process, the solvent partially evaporated to generate an internal pressure, favouring the decomposition of precursors and initiate the crystal nucleation. Hydrothermal process is similar to solvothermal process where water is used instead of organic solvent.

2.2.2 Solid State Synthesis

Solid state reaction route is the most used method for the preparation of solid crystalline compounds from a mixture of solid materials. From thermodynamic and kinetic considerations, it is necessary to anneal the starting precursors at much higher temperature ranging from 300 to 1500 ˚C. In a typical synthesis, the reactants first dried thoroughly and mixed in a required amount using manual or mechanical mixing techniques. During this process, sufficient number of volatile solvents, such as acetone or alcohol, are added to the mixture to assist the hominization. Finally, the solid precursor materials are placed in a suitable container, which is thermally stable, and chemically inert to the reactants during thermal treatment. The heating program to be employed depends entirely on the form and reactivity of the starting materials.

2.3 Materials Characterization

2.3.1 X-ray Diffraction (XRD)

X-ray diffraction technique was used to investigate the crystallographic structure and chemical composition of as-prepared materials. Every matter is composed of atoms, ions, or molecules. The arrangements of these atoms, ions, or molecules in three-dimensional space determine the crystalline or amorphous nature of a matter. When the arrangements are in regular and repetitive manner, then the matter is considered as crystalline and if not, it is called amorphous. X-rays are the high-energy electromagnetic radiation with very short wavelength. When an X-ray beam interacts with an atom of targeted material, it is scattered in all possible direction to produce constructive interference which can be determined by Bragg's equation:

$$n\lambda = 2d \sin\theta$$

In this equation, d is the spacing between diffraction planes, θ is the diffraction angle, n is the order of diffraction or could be any integer, λ is the wavelength of the X-ray beam. In this thesis, XRD

was conducted on a Bruker D8 DISCOVER XRD. This device uses Cu Kα radiation, λ = 1.5418 Å.

2.3.2 Scanning Electron Microscopy (SEM)

Field emission scanning electron microscopy (FESEM) is one of the most useful tools to investigate the morphology of a nanomaterial. This technique is relying upon the interaction between focused electron beam and atoms of the sample, which can provide detailed physical information such as, topography, composition, and elemental percentage (equipped with energy dispersive X-ray spectroscopy (EDS). In this thesis, A Zeiss Supra 55VP high resolution FESEM was used, which was operated with an acceleration voltage of 5 ~ 20 kV.

2.3.3 Transmission Electron Microscopy (TEM)

Transmission electron microscopy (TEM) is a powerful tool to investigate detailed morphological information of as-prepared nanomaterial, such a high-resolution image, crystalline information, and phase features. In this technique, an ultra-thin specimen which is less than 200 nm is used so that a beam of electrons can be transmitted through the specimen and produce high-resolution image. In this doctoral work, TEM images were captured by a HR-TEM (Tecnai-G2 F30 S-Twin, 300 kV).

2.3.4 Raman Spectroscopy

Raman Spectroscopy is molecular spectroscopic technique to determine vibrations, rotational and other low-frequency modes of a molecule. Therefore, this technique is useful to identify the structural footprint of that molecule. When a molecule is irradiated by electromagnetic radiation, the radiation will interact with the bonds and electron clouds of the molecule. Then, the Raman Effect occurs in a form of inelastic scattering. This spectroscopy technique records the energy shift

of photons, caused by the interaction of a monochromatic laser and molecular vibrations, phonons, or other excitations. In this thesis, the Raman spectra were recorded on a Leica DMLB microscope (Wetzlar, Germany) with 17 mW at 633 nm helium neon laser.

2.3.5 X-ray Photoelectron Spectroscopy (XPS)

XPS is a surface-sensitive technique, which is useful to identify the elemental composition, chemical and electronic state of the compositional elements present within a molecule. XPS spectra obtained by irradiating a material with a beam of X-rays under ultra-high vacuum and simultaneously recording the kinetic energy and number of escaping electrons from the surface (from top 0 to 10 nm) of the sample. In this thesis, the XPS were recorded on ESCALAB250Xi (Thermo Scientific, UK) equipped with mono-chromated Al Kα radiation (energy 1486.68 eV).

2.3.6 Brunauer- Emmett-Teller (BET) technique

Brunauer-Emmett-Teller (BET) method has been widely used to measure the specific surface area, pore size distribution and pore volume of a solid material. BET surface area can be measured by allowing adsorption of nitrogen molecules on the surface of the desired material and counting experimental points at a relative pressure of $P/P_0 = 0.05 – 0.25$. The pore size distribution of a porous material can be calculated using Barret-Joyner-Halenda (BJH) method. In this doctoral work, the BET surface area of as-prepared samples was recorded on a Micromeritics 3Flex analyzer at the temperature of 77 K.

2.3.7 Thermogravimetric Analysis (TGA)

Thermogravimetric analysis (TGA) is a technique of thermal analysis in which the mass of an as-prepared sample is measured over time as the temperature changes. This method is very useful to detect several physical phenomena, such as sublimation, vaporization, adsorption and desorption, and different chemical phenomena, such as chemisorption, dehydration, and thermal

decomposition. In this doctoral work, the TGA analysis was used to determine the sulfur percentage and carbon ratio in the as-prepared composite material. TGA experiment was performed on an SDT 2960 at a heating rate of 10 ˚C min^{-1} under N_2 atmosphere from room temperature to 500 ˚C.

2.4 Electrochemical techniques

2.4.1 Electrode Preparation

The slurry for the Li-S battery was prepared by mixing 80 wt.% active material, 10 wt.% conductive additives (Super P, Sigma Aldrich, ≥ 99%) and 10 wt.% Polyvinylidene fluoride (PVDF) or polytetrafluoroethylene (PTFE) as binder. For PVDF, N-methyl pyrrolidone (NMP) was used as a solvent while, propan-2-ol was chosen for PTFE. The obtained homogeneous slurry was spread onto carbon-coated aluminium foil which is then dried in a vacuum oven at 60 ˚C for 12 hours.

2.4.2 Cell assembly

The Li-S cells were assembled in an Ar-filled glove box (Mbraun, Unilab, Germany) using CR2032-type coin cells. Sulfur-containing electrodes were used as the cathode while lithium metal foil was used as the counter and reference electrode. A polypropylene separator saturated with electrolyte was then inserted between the cathode and the anode. the electrolyte was 1.0 M Lithium bis (trifluoromethane sulfonel) imide (LiTFSI, 99.95%, Aldrich) and 0.1 M $LiNO_3$ in 1:1 (v/v) mixed solvent of 1, 3-dioxolane (DOL) and 1, 2-dimethoxy ethane (DME).

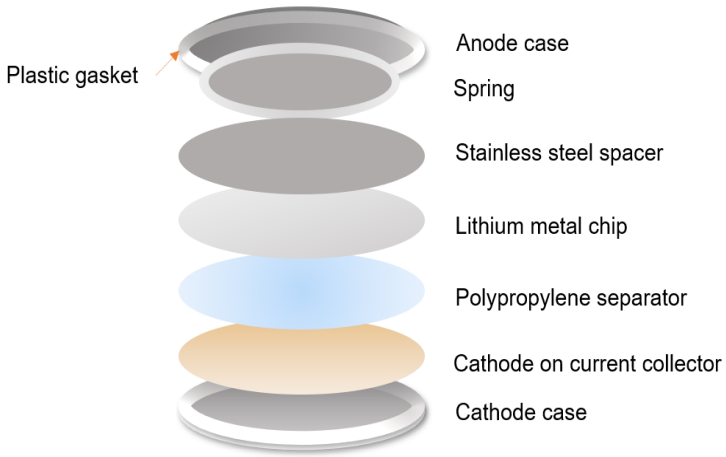

Figure 2.2 Schematic configuration of 2032-type coin cells used for electrochemical characterization of Li-S electrodes.

2.4.3 Cyclic Voltammetry

Cyclic voltammetry is an electrochemical technique to measure the current to the response of linearly sweeping voltage as a function of time set between two or more points. By using CV one can investigate the oxidation, reduction process and intermediates of material and initiation of the chemical reactions by electron transfer which includes catalysis. Since the current is dependent of the material concentration, by using the calibration curve of current vs. concentration one can find out the concentration of unknown material by using current. Basically, the redox potential of the active material should be contained within the potential window of CV to analyse the electrochemical property of the material. In this study, Cyclic Voltammetry data was collected by using Biologic VMP3 between 1.7 – 2.8 V at an adjustable scan rate (mV s^{-1}).

2.4.4 Galvanostatic discharge-charge

The specific capacity, cycling stability, rate performance and discharge-charge profile of the sulfur-containing cathode were obtained by galvanostatic charge-discharge experiments. During

this study, the Li-S cell was discharged and charged within a certain cut-off voltage potential range applying constant current. In this study, the galvanostatic measurements of Li-S cells were conducted in the voltage range of 1.7 to 2.8 V using a LAND CT2001A charge-discharge system. All experiments were carried out at room temperature.

2.4.5 Electrochemical Impedance Spectroscopy

The resistance is the ability of a resist the current in electrical circuit. The Ohm's law defines the resistivity but only limited to one circuit element i.e., resistor. But in real time there are many more circuit elements such as inductor, capacitor which shows different complex behaviours in electrochemical circuit. To know about ideal current resistivity, one should consider these complex elements and need to be study with the different name i.e. impedance other than resistance. This electrochemical impedance measures by applying AC current signal to the electrochemical cell. EIS is mainly used to study charge transport across the membrane and interfaces, electrode kinetics and double layer studies. From the obtained data, the equivalent electrical circuit (series and parallel combination of electrical components) of electrochemical cell cab be designed. Most of the circuit elements in the electrochemical cells are double layer capacitance (C_{dl}), electron transference resistance (R_e), uncompensated resistance (R_s) and Warburg impedance (Z_w). In this doctoral research, the electrochemical impedance spectroscopy (EIS) of all the electrodes were measured using a CHI 660C and Biologic VMP3 systems.

Chapter 3

Squalene-Derived Sulfur-Rich Copolymer@ 3D Graphene-Carbon nanotube Network Cathode for High-Performance Lithium-Sulfur Batteries

3.1 Introduction

Recently, Lithium-sulfur (Li-S) batteries have been regarded as one of the most promising rechargeable batteries for energy storage and conversion. The Li-S battery is capable of delivering a specific energy of 2567 Wh kg^{-1}, almost 6 times higher than the state-of-art electrode materials based on intercalation mechanisms. It also can provide a high reversible capacity of 1672 mAh g^{-1} at average potential 2.0 V, which is 10 times higher than conventional $LiCoO_2$ cathodes,[2, 12] In addition, sulfur is environmentally benign and widely accessible at a low cost.[59, 124] Despite those advantages, the efficient use of sulfur as cathode for rechargeable Li-S batteries is severely hindered by its huge volume expansion during cycling (~80%), poor electronic conductivity (~5 × 10−30 S.cm^{-1}) and dissolution of both elemental sulfur and its intermediate polysulfides into electrolytes before and after cycling. Additionally, the insoluble intermediate polysulfides (Li_2S_2/Li_2S) tend to deposit on the electrodes, which can initiate blockages for both electronic and ionic transports.[3, 125, 80] Several attempts have been made to resolve the aforementioned issues focusing mainly on nano-architecturing of the hosts, including graphene-composites, [64, 104, 126, 127] porous carbon [4, 85, 128, 129] MXene [130] and metal oxides/ nitrides/ sulphides.[50,65, 105, 109, 131] Although achieved some improvements, the physical confinement in those approaches is always kinetically unfavourable to immobilize the dissolved polysulfides. Therefore, another potentially efficient and simple strategy has been developed, based on the free radical polymerization between sulfur and suitable organic monomers. In particular, at 159 °C, a cyclic ring of elemental sulphur (S_8) undergoes a ring opening polymerization (ROP) reaction, which is ended up with

the formation of linear polysulfane diradicals as temperature is raised to 180 °C. This diradical participates in an inverse vulcanization react with vinylic monomer to yield a sulfur copolymer with C-S bonds. [131] This type of synthesis strategy has several advantages such as being rapid, scalable and easy to handle. The copolymer can possess a sulfur content up to 90%, and the chemical confinement from the S-C bond can suppress the dissolution of sulfur and polysulfide into electrolyte. Recently, Pyun et al. synthesized a sulfur-rich copolymer utilizing inverse vulcanization between sulfur and 1,3 diisopropenyl benzene (DIB) for Li-S cathode.[132, 11] Li et al. have anchored the same copolymer onto a 3D graphene framework and demonstrated excellent cycling performances.[116] Furthermore, this approach was extended to similar type of monomers: cardanol-benzoxazine sulfur copolymer/rGO, [133] sulfur copolymer with waste rubber [134] and thiocyanuric acid-sulfur copolymer.[135] However, all these above-mentioned materials contain carcinogenic benzoic moieties, are expensive and hardly biodegradable. In addition, some of these materials need prolonged and sensitive stepwise synthesis techniques for their monomer preparation. Besides, the low conductivity of such sulfur copolymer greatly reduces the rate and cycling performances of Li-S batteries.

Herein, a report for well-designed sulfur-rich copolymer@3D graphene-carbon nanotubes (G-CNT) network cathode for high-performance Li-S batteries. The sulfur-rich copolymers can be rapidly synthesized on large scale by inverse vulcanization of elemental sulfur and 10% squalene as a monomer. As an economical and environmentally friendly material, squalene can be widely obtained from shark liver oil, amaranth seed, wheat germ, rice bran and olives. Besides these, the high temperature stability and non-volatility (boiling point ~285 °C) of squalene make it an ideal monomer for the preparation of sulfur copolymer. The chemical bonding between the carbon and sulfur in the prepared copolymer can greatly suppress the

polysulfides dissolution during cycling. The interlinked Sp^2 graphene/carbon nanotube network can not only provide the composite with an excellent electrical conductivity together with an efficient polysulfide entrapment capability, but also enhance the mechanical durability of the cathode. In addition, the porous structure of the cathode can facilitate the ultra-fast Li-ion diffusion during the electrochemical cycling. Thereby, combining the chemical bonding of sulfur with the physical confinement of polysulfides in carbon framework, as-developed cathode delivered a high specific capacity of 1265 mAh g^{-1} at 0.2 C, a high-rate capability, and an excellent cycling stability with 782 mAh g^{-1} at 1 C after 300 cycles.

3.2 Experimental

3.2.1 Preparation of graphene (G)

Graphene oxide (GO) was synthesized by an improved method reported elsewhere. rGO was synthesized by thermal reduction of GO. Simply, 0.1 g GO sheets are thermally treated in a tube furnace under a stream of Argon gas at 900 °C for 1 h with a heating rate of 5 °C min^{-1}.

3.2.2 Preparation of graphene-carbon nanotubes (G-CNT) structures

Vertically aligned CNTs were grown on graphene surfaces by a chemical vapour deposition (CVD) technique reported earlier.[136] Typically, a stable GO dispersion was achieved by sonication of 0.15 g GO in 20 mL DI water with 0.025 g sodium dodecyl benzenesulfonate (SDBS) and referred to as solution 1. Solution 2 was prepared by mixing 0.228 g Co $(NO_3)_3$, 6 H_2O and 0.336 g hexamethyltetraamine (HMT) in 20 mL equimolecular mixture of ethanol and DI water (v/v, 1/1). Next, solution 1 and 2 were mixed together and then treated under a microwave source at 120 °C for 5 min. This will result in the deposition of $Co(OH)_2$ nanoparticles onto reduced graphene sheets. The black product was washed, dried and finally

subjected to chemical vapour deposition (CVD) process under acetylene (C_2H_2) flow for 10 min at 600 °C. The black mass was collected and washed with dilute HCl to remove the cobalt-derivatives.

3.2.3 Preparation of sulfur-rich copolymer (SP, ~90% sulfur)

233 µL of squalene (Aldrich) was added to 1.8 g of molten sulfur, which was then heated to 180 °C and vigorously stirred for 15 min. The product was then collected and kept under vacuum at 110 °C for 24 h to ensure the complete removal of unreacted sulfur.

3.2.4 Preparation of SP@G and SP@G-CNT (~85% sulfur)

Firstly, a mixture of 0.425 g molten sulfur and 58 µL of squalene was stirred for 5 min at 180 °C. Subsequently, 0.024 g (5 wt.%) of either graphene or graphene-CNT was added to the same and vigorously stirred mixture for another 10 min under the fixed temperature. Finally, composites were collected after the same drying technique as performed for SP.

3.2.5 Characterization

The crystal structure and phases of as-prepared materials were characterized by X-ray diffraction with a BRUKER D8 Discovery. The morphology was analysed by field emission scanning electron microscope (FESEM, Zeiss Supra 55VP) meanwhile energy dispersive X-ray spectroscopy (EDX) was performed by Zeiss Evo SEM. The FTIR specta of the samples were recorded with a Nicolate 6700 spectrometer. Differential Scanning Calorimetry (DSC) analysis was carried out on TA Instruments Q2000 under a N_2 atmosphere with a heating rate 10 °C min^{-1}. TGA/DTA was performed to analyse the weight ratio of nanocomposite at a heating rate of 10 °C min^{-1} under N_2 flow from room temperature to 500 °C with a SDT 2960

system. The Raman measurement of the nanocomposites were conducted on a confocal MicroRaman Spectrometer with a Lab RAM HR system (Renishaw inVia) using a 632.8 nm He-Ne laser source. X-ray photoelectron spectroscopy (XPS) of the copolymer was performed on an ESCALAB250Xi (Thermo Scientific, UK) equipped with mono-chromated Al Kα radiation (energy 1486.68 eV). N_2 adsorption–desorption isotherms of graphene and CNT/graphene were measured by using a Micromeritics 3Flex analyzer at a test temperature of 77 K. Brunauer–Emmett–Teller (BET) analysis was used to determine the surface area and was calculated using the isothermal points at a relative pressure of $P/P_0 = 0.05–0.25$.

3.2.6 Cell assembly and electrochemical testing

The electrodes were prepared using bare sulfur, SP, SP@G and SP@G-CNT as active material, carbon black as conductive additive and polytetrafluorethylene (PTFE) as binder with an overall ratio of 8:1:1 (by wt. %). The slurry was prepared in propan-2-ol and then casted onto carbon-coated aluminium foil and dried in an oven at 60 °C. The sulfur loadings of the electrodes were within range of 1.2–1.5 mg cm^{-2}, and higher sulfur loading of 2.6 mg cm^{-2} was also evaluated for SP@G-CNT electrodes. Finally, cells were operated in a voltage window of 1.7–2.8 V with an electrolyte composed of 1.0 M lithium bis (trifluoromethane sulfonyl) imide (LiTFSI, 99.95%, Aldrich) and 0.1 M $LiNO_3$ in 1:1 (v/v) mixed solvent of 1, 3-dioxolane (DOL) and 1,2-dimethoxy ethane (DME). The volume of electrolyte injected in the coin cells were controlled about 15 µL electrolyte per mg of sulfur. Porous polypropylene (Celgard 2400) was used as separator. Cyclic Voltammetry (CV) and electrochemical impedance spectroscopy (EIS) of all the electrodes were performed using a CHI 660C. The cyclic voltammogram was recorded with a scan rate of 0.2 mV s^{-1} in the potential range of 1.5–3.0 V. The galvanostatic

discharges-charges were carried out within the potential range of 1.7–2.8 V on a LAND CT2001A charge–discharge system. All experiments were conducted at room temperature.

3.3 Results and discussion

As displayed by the optical images in **Figure 3.1a**, the gradual colour change of the mixture between squalene and liquid sulfur confirms the polymerization reaction. Such polymerization can lead to a chemically stable product, where polysulfur chains remain cross-linked to the squalene units. Considering the insulating nature of the sulfur-rich copolymer (SP), conductive filler such as graphene was employed (only 5 wt.%) to achieve an improved electrochemical performance and the corresponding composite is donated as SP@G (**Figure 3.1b**).

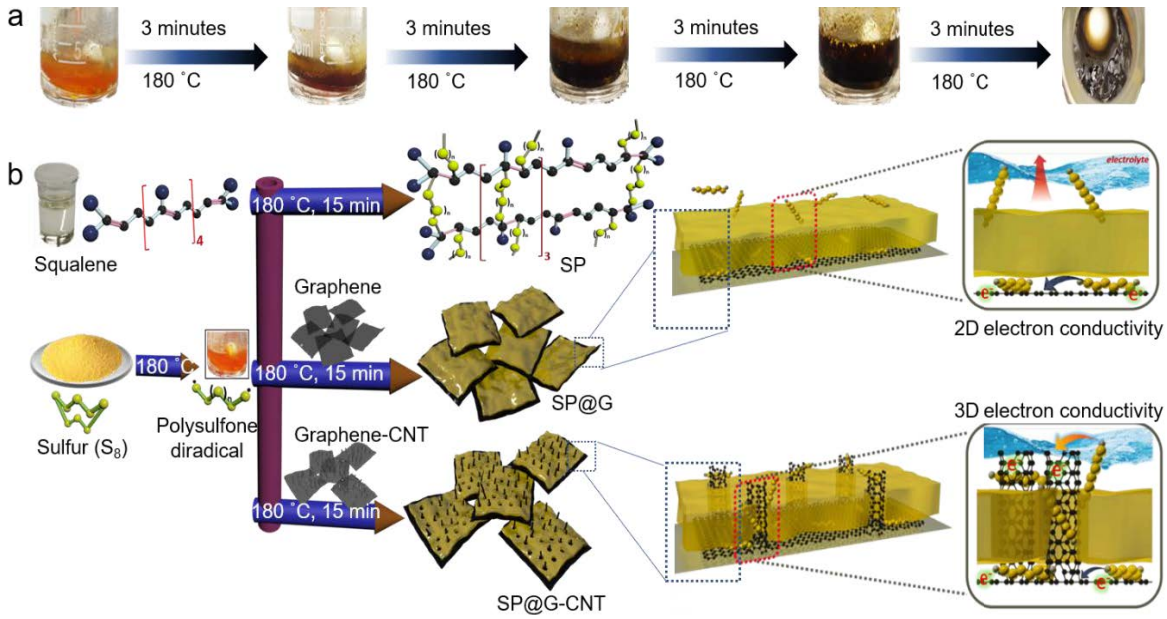

Figure 3.1 Optical images of squalene and molten sulfur mixture during copolymerization reaction, b) Schematic illustration for sulfur-rich copolymer (SP), SP@G and SP@G-CNT and enhanced polysulfide entrapment capability of 3D G@CNT network in SP@G-CNT.

However, the electrical conductivity and volume-buffering ability of graphene is limited to only two-dimensions, and the smooth graphene surface may not be able to provide enough

interaction with the outer-surface of copolymer and the intermediate polysulfides. Thereafter, suitable nanoarchitecture of graphene is quite essential to achieve further improvements in electrochemical performance. We have further grown carbon nanotubes (CNT) on graphene nanosheets by a CVD technique and utilize the nano graphene-carbon nanotubes (G-CNT) networks as conformal holding blocks for sulfur-rich copolymer (termed as SP@G-CNT, **Figure 3.1b**). Here, the growth of carbon nanotubes on graphene can create additional roughness to the graphene surface, that is beneficial for anchoring the copolymer and polysulfides to the conductive matrix. It also can provide a more 3D electronic path and a better buffering network to alleviate the huge volume change of copolymer during the cyclic processes.

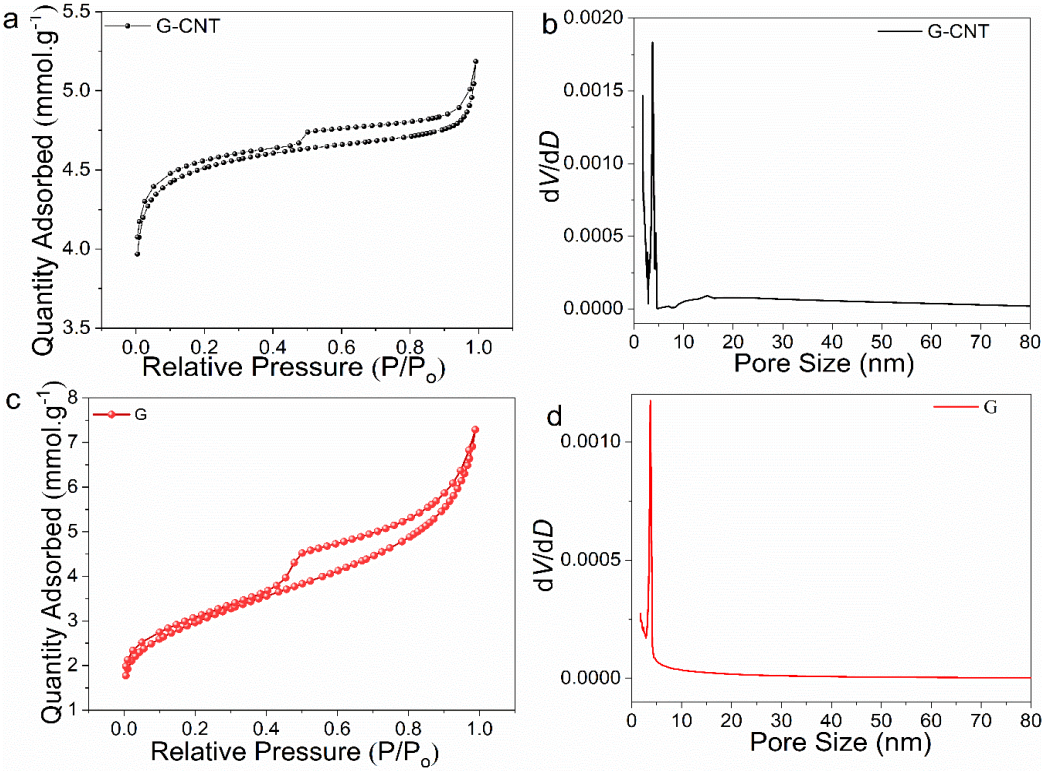

Figure 3.2 N_2 adsorption- desorption isotherm and pore size distribution of (a-b) Graphene-CNT and (c-d) Graphene networks.

Moreover, the G-CNT network can preserve more active surface area for the copolymer compared to the bare graphene, because graphene nanosheets very prone to restack (378.51 $m^2 g^{-1}$ for graphene-CNT vs. 229.42 $m^2 g^{-1}$ for graphene, **Figure 3.2a** and **3.2c**, respectively). For G-CNT network the pore size mainly concentrated around 3.64 nm. Mesopores with size of 14.7 nm are also visible, quite effective for electrolyte infiltration (**Figure 3.2b**). While, for graphene (G) network the pore size was measured to be 3.88 nm (**Figure 3.2d**). To determine the phase of the as-prepared samples, X-ray diffraction (XRD) studies were performed (**Fig. 3.3a**). The less intense sulfur peaks for SP, as compared to that of elemental sulfur indicate the polymeric nature of SP. This peak intensity was further minimized for SP@G and SP@G-CNT respectively, due to uniform distribution of copolymers onto these carbon matrices. As demonstrated by Raman Spectra (**Figure 3.3b**), three peaks located around 150, 220 and 472 cm^{-1} originating from S-S-S bending and stretching vibrations, respectively. Whereas two additional Raman peaks present only for SP@G and SP@G-CNT (1350 cm^{-1}, disordered induced phonon mode; 1580 cm^{-1}, graphite band), confirming the co-existence of graphene/G-CNT with sulfur copolymer.

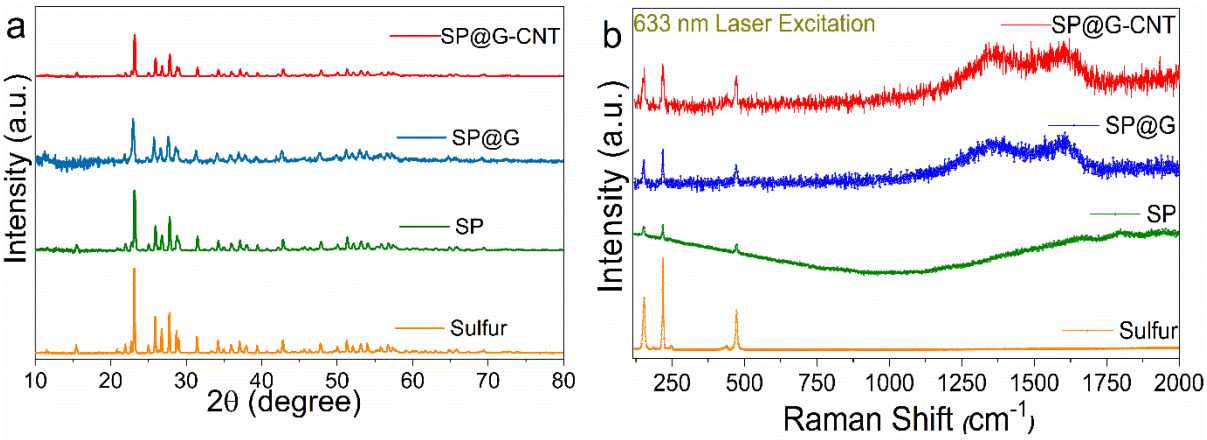

Figure 3.3 (a) X-ray diffraction pattern (XRD) and (b) Raman spectra of Sulfur, SP, SP@G and SP@G-CNT composites.

As shown in Fourier transform infrared spectra (FT-IR, **Figure 3.4a**), SP exhibits all the characteristic peaks of squalene except the peak at 1680 cm^{-1}, which originates from C=C stretching vibration in squalene molecules.[137] This indicates the involvement of the double bond of the alkylene chain with polysulfane di-radicals during sulfur-copolymer formation. The sulfur-rich copolymer was analysed by X-ray photoelectron spectroscopy (XPS) to ascertain details of bonding between squalene units and polysulfur chains. The XPS profile in **Figure 3.4b** displays the expected C and S elements presented in the sulfur-rich copolymer. In the high-resolution XPS spectrum of S2p region for SP (**Figure 3.4c**) can be fitted by three species.

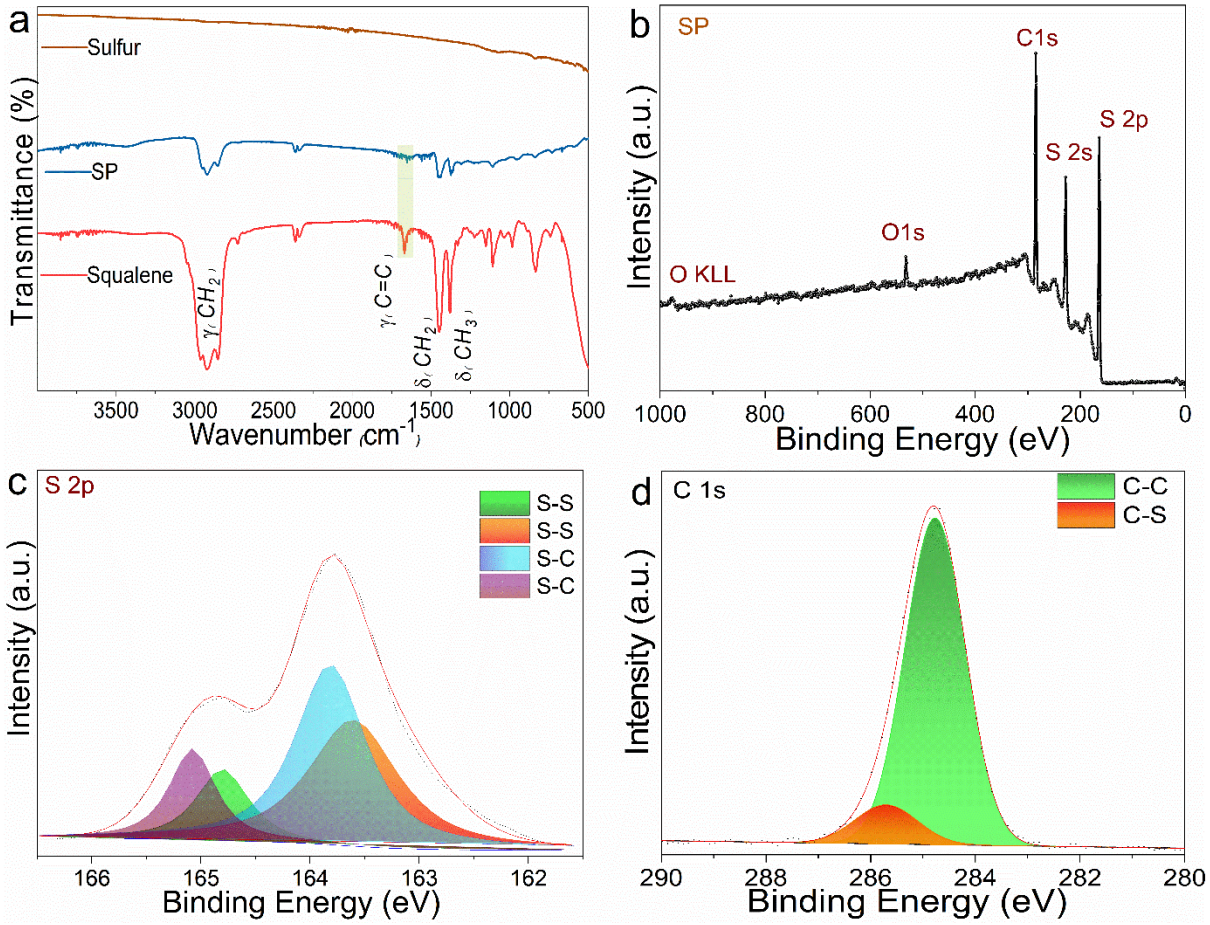

Figure 3.4 (a) FTIR analysis of sulfur, copolymer and squalene; XPS spectra (b) survey, (c) S 2p and (d) C 1s spectra for the sulfur-rich copolymer.

Two peaks centred around 163.7 and 164.9 eV can be assigned to S 2p3/2 and S 2p1/2 responses of sulfur molecules.[130] Two new peaks appeared at around 163.8 and 165.07 eV are related to S 2p3/2 and S 2p1/2 of the S-C bond generated by the successful copolymerization between squalene and sulfur molecules.[138, 139] The C 1s spectra of SP in **Figure 3.4d**, shows two peaks, the first peak at 284.8 eV is belonging to C-C hydrocarbon bonds of the squalene molecules, another peak at about 285.7 eV is ascribed to the C-S bond in copolymer.[138] The formation of cross-linked sulfur and squalene molecules in SP can be further confirmed by differential scanning calorimetry (DSC) experiments. DCS curves for elemental sulfur (**Figure 3.5a**) show three pronounced peaks, the first one at around 111 °C is attributed to the solid-to-solid conversion where orthorhombic sulfur converted into monoclinic phase, second peak at 121 °C due to the melting, peak at 170 °C can be assigned to the breaking of S-S bonds in sulfur to di-radicals formation. For SP, peak at 170 °C disappeared confirming the sulfur is partially covalently bonded to squalene. The amount of sulfur contents in the copolymer and in the composites were quantified by thermogravimetric analysis (TGA, **Figure 3.5b**), a high sulfur content of 87.29 wt% was measured for SP, while the SP@G-CNT and SP@G composites contained 83.73 wt% and 81.46 wt% of sulfur, respectively.

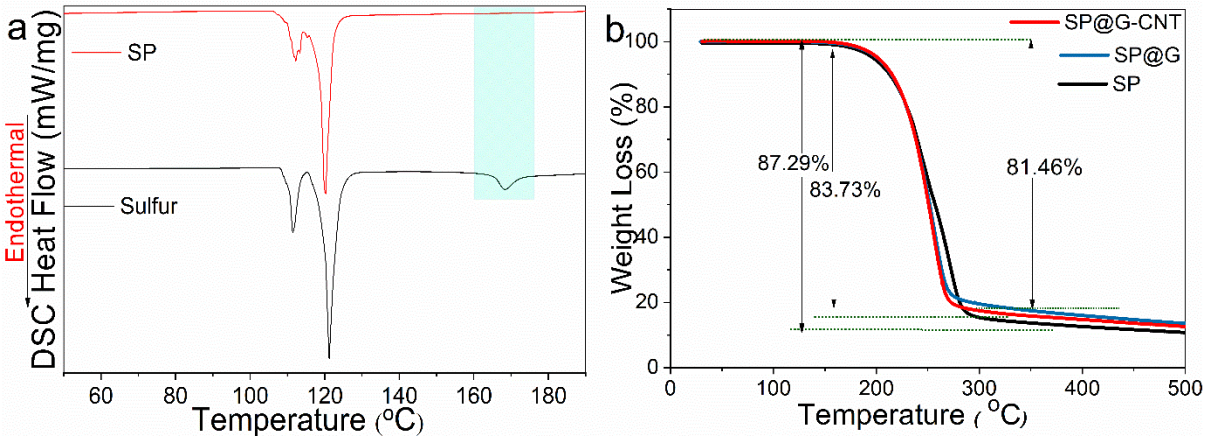

Figure 3.5 (a) DSC traces of sulfur and surfur-rich copolymer (SP). (b) TGA analysis of SP, SP@G and SP@G-CNT composites.

The microstructure and morphology of the as-prepared composites were evaluated by field-emission scanning electron microscopy (FE-SEM) and Energy dispersive X-ray spectroscopy (EDX). **Figure 3.6a** and **Figure 3.6b** display the graphene nanosheets and G-CNT nanostructures used as some conformal hosts for the sulfur-rich copolymer.

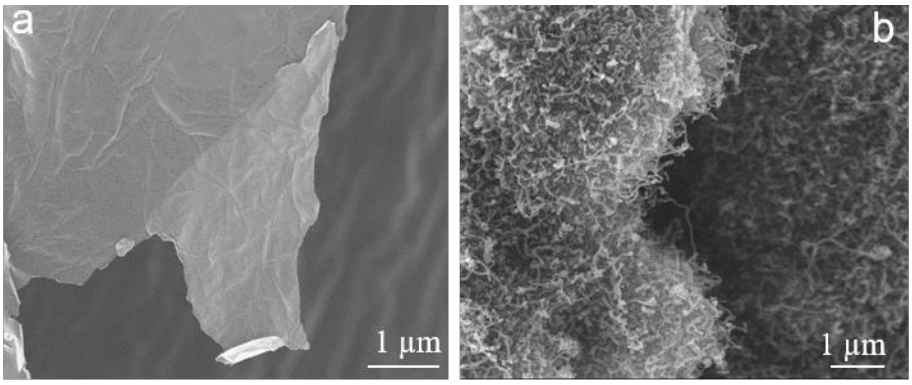

Figure 3.6 FE-SEM images of (a) graphene nanosheets (G) and (b) graphene-CNT (G-CNT).

The SEM figure and corresponding elemental colour mapping of sulfur copolymer (SP) is represented in **Figure 3.7a** and **Figure 3.7b-c**. **Figure 3.7d** displays the uniform coating of copolymer onto graphene-matrix. The addition of graphene should improve the electrical conductivity and mechanical durability of SP@G composite. **Figure 3.7g** for SP@G-CNT, is demonstrating the porous copolymer overlaid onto a G-CNT network, probably influenced significantly by the craggy surface of G-CNT. Such a hierarchical structure is desirable for energy storage applications, as it can render a better percolation network for solvated Li^+ ions through the 3D interconnected hierarchical pores and contains enough void space to buffer the structural deformations during rapid cycling. Elemental colour mapping of SP@G (**Figure 3.7e-f**) and SP@G-CNT (**Figure 3.7h-i**) reveal uniform dispersion of sulfur throughout the organosulfur units and their adhering carbon matrices. To determine the electrochemical performances of the as-

prepared SP and bare sulfur cathodes, typical cyclic voltammograms (CVs) at a scan rate of 0.2 mV S^{-1} within the potential range 1.5–3.0 V were measured and presented in **Figure 3.8**.

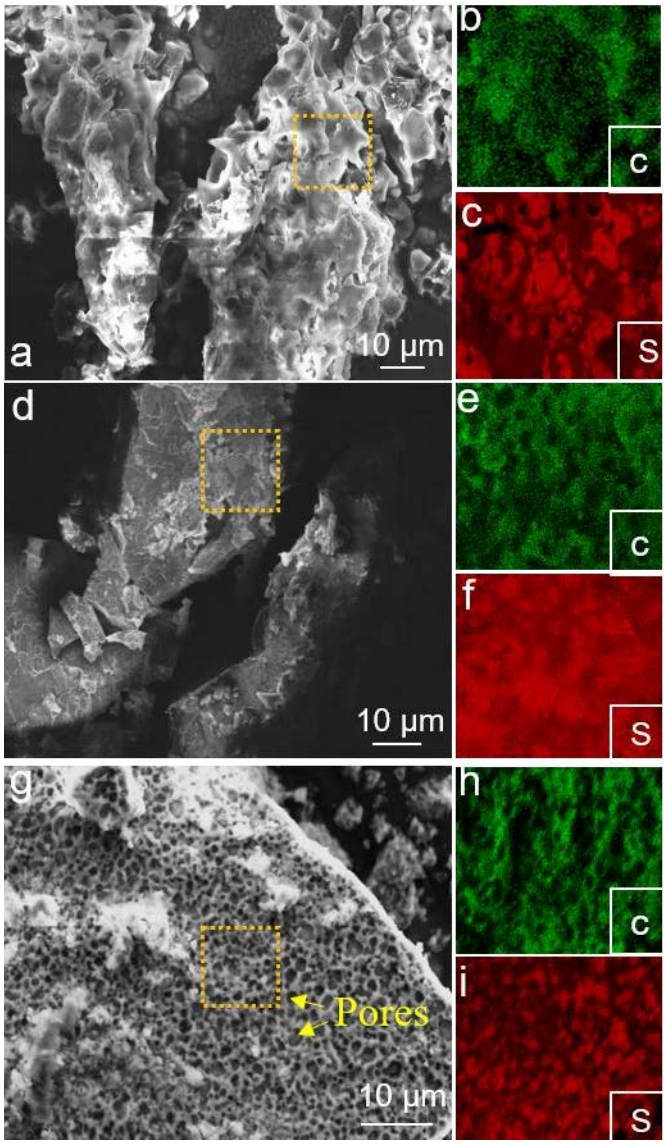

Figure 3.7 FE-SEM images of (a) SP, (b) SP@G and (c) SP@G-CNT. Elemental colour mapping of (b-c) SP, (e-f) SP@G and (h-i) SP@G-CNT.

The CV curves for both SP and bare sulfur electrodes show two reduction peaks and one oxidation peak. The reduction peaks are attributed to the conversion of sulfur to high order polysulfides (Li_2S_n, n ≥4) and sulfur-copolymer to high order organosulfur units; and shortened oligo-sulfur

upon further reaction.[140] Continued discharged to lower potential resulted in Li_2S_2/Li_2S for sulfur and fully discharged organosulfur products for sulfur-copolymer. The intense oxidation peak in the charge process is ascribed to the conversion of short-chain polysulfides/organo-sulfurs to their long-chain structures.

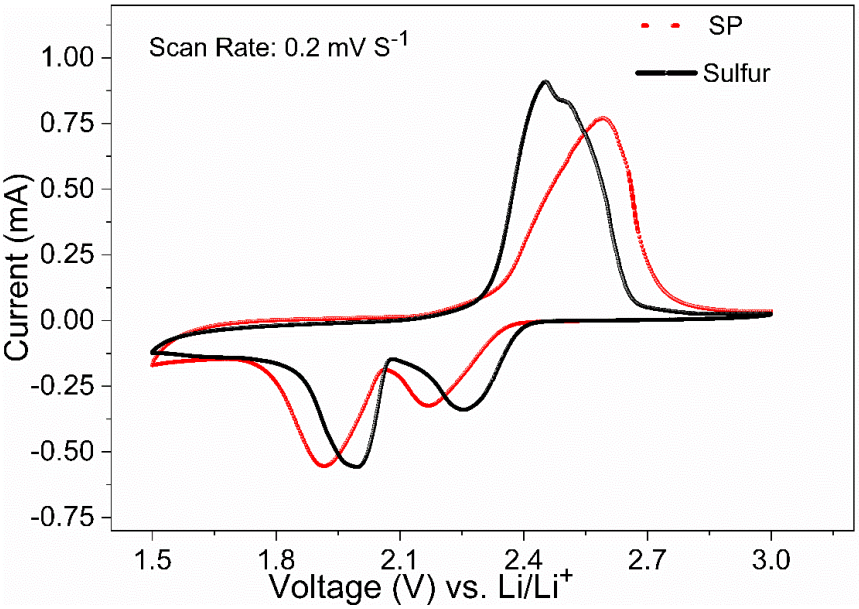

Figure 3.8 Cyclic Voltammograms of sulfur and SP cathodes at 0.2 mV s^{-1} within 1.5~2.8 V vs. Li/Li^+.

These observations therefore confirm that the sulfur-rich copolymer has a similar electrochemical activity to the elemental sulfur (S_8). Considering the similar electrochemical behaviour, the theorical specific capacity for SP can be calculated by multiplying the theoretical specific capacity of sulfur with the weight percentage of sulfur (i.e., 87.3%) in the SP. Therefore, the theoretical specific capacity for SP can reach a value of 1459 mAh g^{-1}. **Figure 3.9a** and **Figure 3.9b** show the galvanostatic discharge–charge profiles of SP and sulfur electrodes at 0.2 C (1C = 1672 mAh g^{-1}) rate within a potential range of 1.7–2.8 V vs. Li/Li^+. Like the CV scans, both the electrodes displayed two discharge plateaus and one charge plateau during discharge–charge.

The upper plateau and its corresponding capacity (Q_H) are attributed to the reduction of sulfur to polysulfides and derived polysulfides diffusion/shuttling.[79, 66] Therefore, the Q_H value can be considered as an indicative parameter to ascertain the initial sulfur and polysulfide dissolution in the electrolyte from the corresponding electrode surfaces. The Q_H value for the SP electrode in the 2nd cycle was found to be slightly higher than the sulfur electrode (302 mAh g^{-1} for SP vs. 288 mAh g^{-1} for sulfur). This difference much increased (234 mAh g^{-1} for SP vs. 114 mAh g^{-1} for sulfur) just after the 50th cycle. In addition, the lower-plateau capacity (Q_L) attributable to the intermediate polysulfides retention is also found to be significantly higher for the SP electrode (512 mAh g^{-1}) than the pure-sulfur (270 mAh g^{-1}) after 50 cycles. This observation clearly reflects the uncontrolled sulfur and polysulfides dissolution and their shuttling in bare sulfur electrodes, while the chemical confinement of sulfur with squalene molecules in SP electrodes dramatically suppress the shuttle effect and the dissolution of sulfur/polysulfides. In addition, the polarization (ΔE) between discharge and charge curves for SP cathodes remain almost unchanged during cycling. However, for the bare sulfur electrodes, the ΔE value was found to increase gradually with cycling, probably caused by the deposition of insoluble and insulating Li_2S on the electrodes, leading to slower redox reaction kinetics. The cycling performance of SP and sulfur cathodes at 0.2 C rate is shown in **Figure 3.9c**. When discharged at 0.2C rate, the SP cathode delivered a discharge capacity of 1023 mAh g^{-1} in the 2nd cycle compared to 932 mAh g^{-1} of sulfur electrode and retained much higher capacity (713 mAh g^{-1}, ~70% retention) than the later (320 mAh g^{-1}, ~34% retention) after their 100th cycles. Such improved electrochemical performance of SP cathode over the bare sulfur cathode is owing to the chemical attachment of sulfur with squalene, which remarkably suppresses the active material dissolution in electrolyte and restrains the polysulfide shuttling.

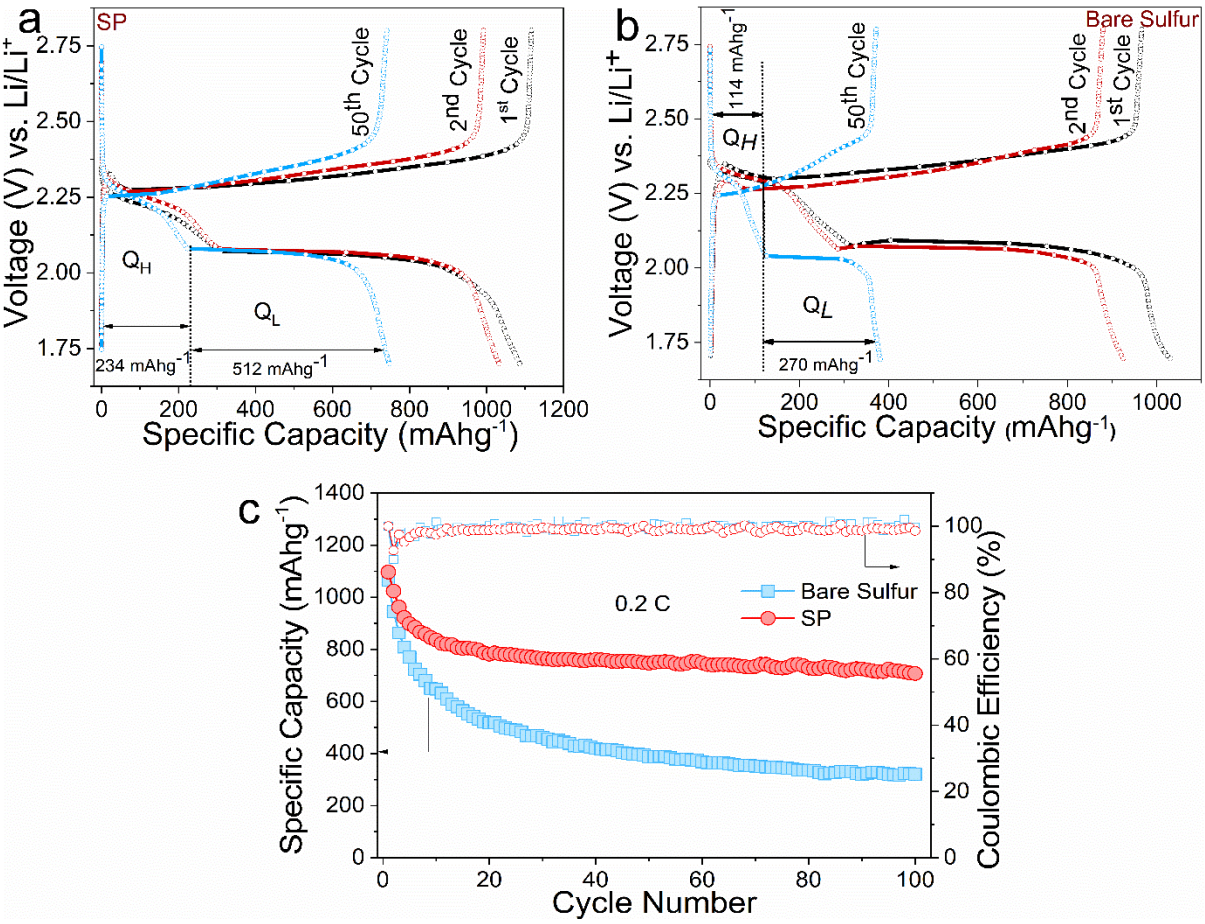

Figure 3.9 Galvanostatic discharge-charge profiles of (a) SP and (b) sulfur cathodes at 0.2 C. (c) Cycling performances of SP and sulfur cathodes for consecutive 100 cycles at 0.2 C.

Moreover, the organic moieties in the copolymer can act as "plasticizer", which could help prevent the uncontrolled deposition of insoluble Li_2S on the electrode surfaces.[116] However, the gradual capacity fading for SP electrodes is probably caused by its lower electronic conductivity. When composited with the conductive matrixes such as, graphene (i.e. SP@G) or G-CNT (i.e. SP@G-CNT) a significant improvement in the electrochemical performance was noticed. **Figure 3.10a** represents the galvanostatic discharge–charge profiles for the composite electrodes (i.e., SP@G-CNT and SP@G) at a 0.2C rate within the potential window of 1.7–2.8 V. The ΔE for both composites were found to be significantly low (around 0.23 V), indicating faster redox reaction

kinetics. When discharged at 0.2C rate, SP@G-CNT cathodes achieved a remarkably high Q_H value of 368 mAh g^{-1}, which indicates the controlled sulfur/polysulfides dissolution and much improved electronic conduction, facilitating the reduction process of sulfur/polysulfides. **Figure 3.10b** shows the cycling stability of SP@G and SP@G-CNT cathodes.

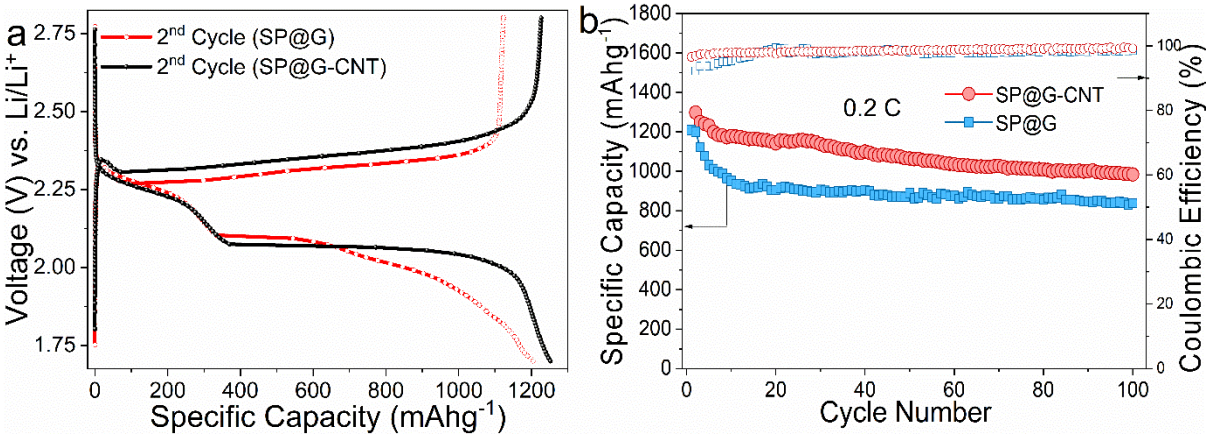

Figure 3.10 (a) Galvanostatic discharge-charge profiles and (b) Cycling performances of SP@G and SP@G-CNT composites at 0.2 C rate.

The SP@G-CNT cathode delivered a reversible capacity of 1249 mAh g^{-1} in its 2nd discharge cycle at 0.2C rate and maintained at 961 mAh g^{-1} after 100th cycle. This result is truly remarkable considering the high sulfur content (83.73%) in the SP@G-CNT composite. On the contrary, the SP@G electrodes achieved a very high discharge capacity of 1205 mAh g^{-1} in their 2nd cycle and recovered at 838 mAh g^{-1} at the end of 100 cycles (**Figure 3.10b**). Both the electrodes attained a high Coulombic efficiency (~99%) throughout their cycling. A comparative study of rate performances for both the composite electrodes is depicted in **Figure 3.11a**. The SP@G-CNT cathode delivered a reversible capacity of 1265 mAh g^{-1} (0.2C), 958 mAh g^{-1} (0.5C), 825 mAh g^{-1} (1C) and 762 mAh g^{-1} (2C), respectively. On the other hand, SP@G electrode achieved 1193 mAh g^{-1} (0.2C), 846 mAh g^{-1} (0.5C), 692 mAh g^{-1} (1C) and 614 mAh g^{-1} (2C). The extended

cycling performances of SP@G-CNT and SP@G electrodes are displayed in **Figure 3.11b**. Before discharging at a high current density (1C), these electrodes were discharged and re-charged at 0.2C for an initial five cycles to form stable solid electrolyte interfaces (SEI). At 1C rate, SP@G-CNT electrodes delivered an average reversible capacity of 782 mAh g^{-1}, which then decreased to 627 mAh g^{-1} at the 300th cycle.

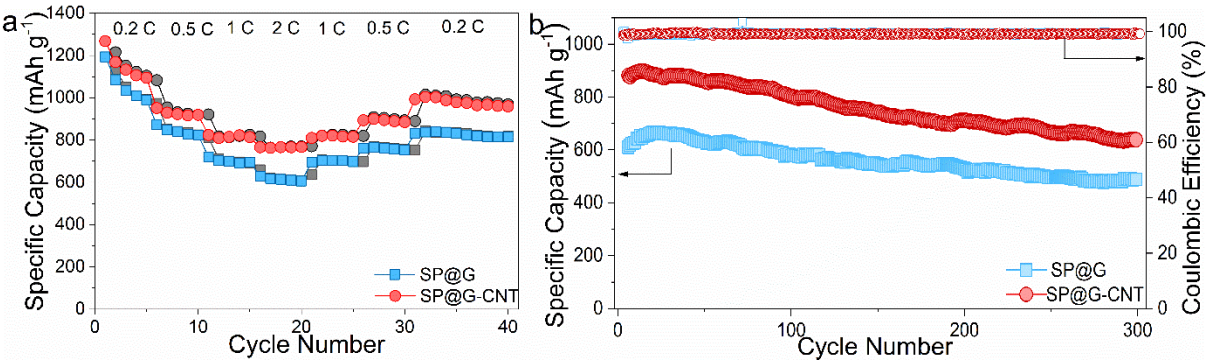

Figure 3.11 (a) rate performances at different current densities, (b) long-term cycling performances of SP@G and SP@G-CNT electrodes at 1C rate (results are shown from 6th cycle as both the electrodes were discharged-charged at 0.2 C rate for initial 5 cycles).

Meanwhile, SP@G electrodes achieved an average capacity of 578 mAh g^{-1} under the same current density (1C) and retained 472 mAh g^{-1} at the end of 300 cycles. We further conducted additional cycling tests using our best performing cathode (i.e. SP@G-CNT) with sulfur loadings (~2.6 mg cm^{-2}). 40 µL of electrolyte was used to confirm complete infiltration of thick electrodes. As depicted in **Figure 3.12a**, a high discharge capacity of 944 mAh g^{-1} was achieved at 0.2C rate in the first cycle and could still deliver a reversible capacity of 728 mAh g^{-1} after 100th cycles with an average Coulombic efficiency above 99% throughout the cycling.

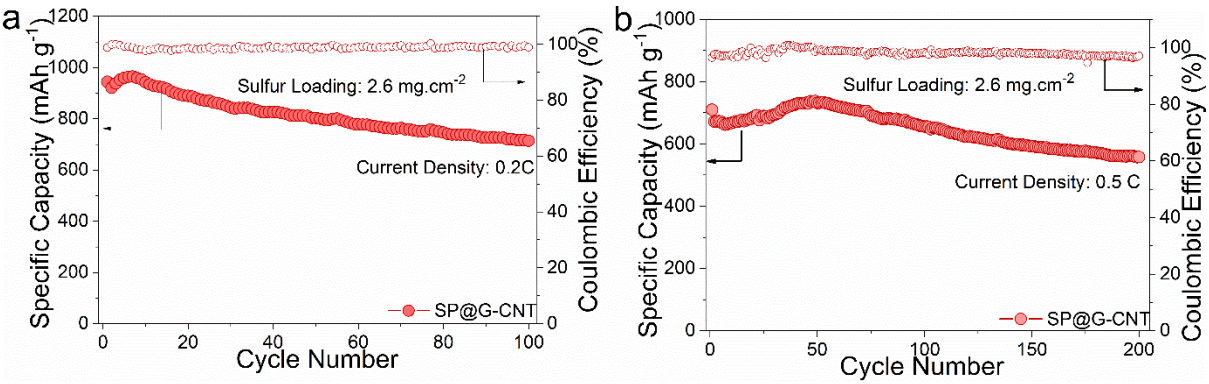

Figure 3.12 Cycling performances of SP@G-CNT electrodes with a sulfur loading of 2.6 mg cm^{-2} at (a) 0.2 C and (b) 0.5 C.

Furthermore, when discharged at a high rate of 0.5C (**Figure 3.12b**), the high sulfur loaded SP@G-CNT electrode delivered an initial discharge capacity of 715 mAh g^{-1} and recovered 542 mAh g^{-1} after 200 cycles. To explore the interfacial charge transfer kinetics of the as-prepared electrodes, electrochemical impedance spectroscopy (EIS) was performed on the open circuit potential (OCV). In the impedance spectra (**Figure 3.13**), R_Ω and R_{ct} are attributed to the Ohmic resistance and charge transfer resistance coupled with double layer capacitance Q_{dl}, respectively, and W (Warburg impedance) is represented by a straight line arising from solid-state diffusion. The SP@G-CNT ($R_{ct} \sim 172\ \Omega$) and SP@G ($R_{ct} \sim 238\ \Omega$) electrodes exhibited much reduced charge transfer resistance (R_{ct}) compared to SP ($R_{ct} \sim 375\ \Omega$) and bare sulfur ($R_{ct} \sim 389\ \Omega$) electrodes. The reason for the improved electrical conductivity of the as-prepared composites is mainly attributed to the incorporation of carbon scaffolds in the composite structures. The minimum charge transfer resistance in SP@G-CNT is typical of its porous structure, which implies ultrafast Li^+ diffusion throughout interconnected pores.

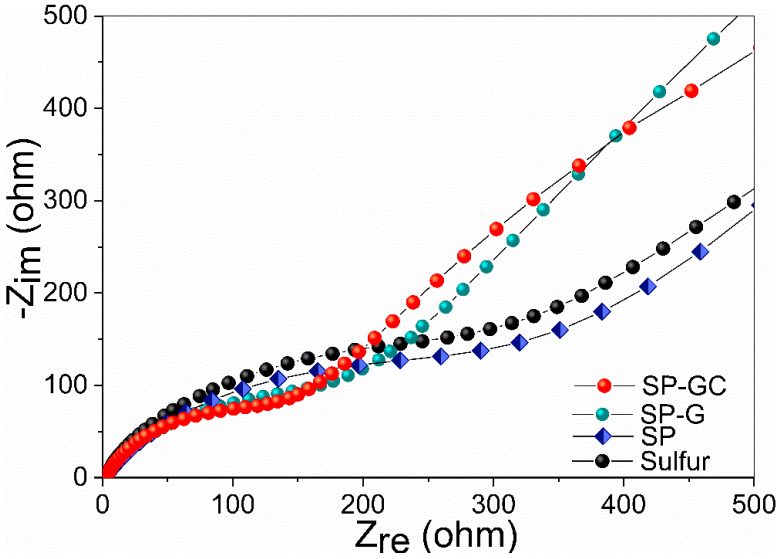

Figure 3.13 Electrochemical impedance spectroscopy (EIS) of sulfur, SP, SP@G and SP@G-CNT electrodes.

The excellent cycling stability and outstanding rate performances for SP@G-CNT electrodes over SP@G electrodes could be ascribed to the following factors. (i) A multidimensional electron transport pathway rendered by 3D G-CNT scaffolds in SP@G-CNT could accelerate the sulfur/polysulfides reduction, compared to the 2D conductive graphene in SP@G. (ii) The interconnected pores in SP@G-CNT composites facilitate easy electrolyte access, and lead to an ultrafast Li^+ ion diffusion throughout the electrode and enhanced rate performance. (iii) Porous copolymers supported by flexible 3D G-CNT possess enough void spaces to relieve the strain developed during cycling and maintain the structural integrity over long-term cycling. (iv) During extended cycling, 2D graphene in SP@G could be ineffective for preventing polysulfide dissolution from the copolymer-electrolyte interface, although it can obviate similar diffusion from graphene-copolymer interfaces. In contrast, rationally designed 3D G-CNT network can remarkably immobilize the polysulfide diffusion from both the interfaces.

3.4 Conclusion

In summary, here is a report of a novel sulfur-rich copolymer@ 3D graphene-carbon nanotubes cathode for Li-S batteries. The sulfur-rich copolymer has been prepared via a simple, scalable and sustainable approach using squalene monomer provides excellent chemical confinement of sulfur, which greatly circumvents the sulfur/polysulfides dissolution and irreversible low ordered polysulfide deposition on electrode surfaces. Sp^2 graphene-carbon nanotubes have been employed in the cathode to address the poor electronic conductivity and slow polysulfide dissolution of sulfur copolymer and served as optimised conformal holding blocks for copolymers. The as-developed cathode delivered a high reversible capacity of 1265 mAh g^{-1} at 0.2C, and average capacity of 782 mAh g^{-1} at 1C with excellent cycling stability over 300 cycles. The excellent electrochemical performance of this composite material is solely attributed to the optimized porosity, improved 3D electronic conductivity, a better mechanical strain buffering network and excellent polysulfide entrapment capabil

Chapter 4

Multi-Application of Amine-functionalized Metal-Organic Frameworks in High-performance Lithium-Sulfur Batteries

4.1 Introduction

As the traditional lithium-ion batteries based on intercalation chemistry are approaching their theoretical energy density limits, intensive research efforts are being made to obtain advanced battery systems involving new battery chemistries. Room-temperature lithium-sulfur (Li-S) batteries have attracted immense interest as next-generation battery systems, owing to their high theoretical capacity (1675 mAh g^{-1}) together with the natural abundance and low-cost of elemental sulfur. [21, 24] However, the practical applications of Li-S batteries have been severely hindered by the problems associated with both the sulfur cathode and the metal anode. As for the sulfur cathode, the poor electronic conductivity and large volume expansion of sulfur (~80 %) limit the electrochemical activity. Moreover, the soluble polysulfide as reactive intermediates tend to diffuse though the separator and reacts with the Li anode, which escalates the issues of active material loss, self-discharge and rapid capacity fading. [141, 3] Additionally, the involvement of polysulfides can lead to a solid electrolyte interface (SEI) layer with higher resistance and larger activation energy, which causes an accelerated degradation of Li-metal anode. [142]

So far, several strategies have been proposed to restrain the soluble polysulfides within the cathode and thereby improve the performance, which include designing sulfur hosts or separators, [4, 50, 71, 142] optimizing the electrolyte formula, [76, 143- 145] and protecting the anode by surface coatings.[146, 147] Among them, one of the most common approaches is to employ carbonaceous materials as a sulfur-host or a physical barrier coated on the separator. Nevertheless, the weak interactions between nonpolar carbon and polar polysulfides are not effective enough to block the shuttling of polysulfides for long-term cycling.[148, 149] Recently, polar materials, such as

heteroatom-doped carbon and transition-metal compounds (metal oxides/sulfides/ nitrides/phosphides) have been exploited tremendously as sulfur-reservoirs. [109, 150-155] The polar materials can bind the polysulfides in a chemical way, which is more effective than physical adsorption of nonpolar carbon. This strategy, to some extent, have inhibited the polysulfide shuttling. However, the capacity and cycling stability obtained to date have still been far from satisfactory. [109]

Metal oxide frameworks (MOFs) represent a special class of crystalline materials composing of organic struts with inorganic nodes, which feature high accessible surface area and tunable pore-size distribution.[156] Recently, their structural and composition attributes have enabled their application as a sulfur-host in alkali metal-sulfur batteries.[122, 157] However, the limited pore volume and the almost insulating nature of the MOFs inevitably lessen the amount of sulfur loading, and lead to short cycle life and poor rate capability of the alkali metal-sulfur batteries.

In this chapter, a micro/mesoporous N-doped carbon was synthesized from UIO-66-NH_2 MOF (termed as NH_2-MOF) and utilized the resulting porous structure as a sulfur-host for Li-S batteries. UIO-66- NH_2 is a functional derivative of Zr- based UIO-66 MOFs, which is facile to prepare and possess excellent thermal and chemical stability. More importantly, the pendent amidogen (-NH_2) functionalities in this MOF can also serve as a nitrogen source during the carbonization process to yield N-doped carbon, in which the N-doped sites can interact with the polysulfides and efficiently retard their shuttling. The micropores (< 2 nm) in such carbon- host can provide enormous active sites for the adsorption of sulfur on the carbon surface, whereas the mesopores (~ 3.7 nm) can improve the sulfur loading and increase electrolyte penetration into carbon structure. To further restrain the polysulfide migration and eliminate the issue of anode corrosion, a NH_2-MOF@graphene oxide (GO, acts as strength enhancement) interlayer was developed. The three-

dimensional channel structure of NH_2-MOF shows mesoporosity with a narrow pore size (approximately 5.2 Å), which is significantly smaller than the diameter of polysulfides (1-2 nm). [158] This enables the NH_2-MOF to act as a physical barrier against the shuttling of polysulfides. Moreover, the abundant amidogen functionalities of the NH_2-MOF can strongly bind the polar polysulfides by acid-base type interaction, suppressing their diffusion and the anode degradation. Thus, the as-developed Li-S batteries exhibit a reversible capacity of 1318 mAh g^{-1} at 0.2 C, with extended cycling stability and much improved rate performance.

4.2 Experimental Section

4.2.1 Synthesis of nano-octahedral UIO-66-NH_2 (NH_2-MOF) and UIO-66:

In a typical synthesis, a mixture of $ZrCl_4$, 2-amioterepthalic acid (for UIO-66-NH_2) or terephthalic acid (for UIO-66) was added into 40 mL of dimethylformamide containing a certain amount of acetic acid in a 50 mL of borosilicate glass vial. The molar ratio of metal ion/ligand was maintained at 1. The vial was capped and placed into a pre-heated oven at 120 ˚C for 18 h. After the completion of the reaction, the obtained product was collected by centrifugation and repeatedly washed with dimethylformamide and methanol. Finally, the product was dried under vacuum at 90˚C.

4.2.2 Synthesis of micro-/mesoporous N-doped carbon (NMC) or micro-/mesoporous non-doped carbon (MC) and their sulfur composites:

A certain amount of UIO-66- NH_2 (for NMC) or UIO-66 (for MC) was heated at 800 ˚C for 1 h under a nitrogen flow with a heating ramp of 5 ˚C min^{-1}. After cooling down to room temperature, the obtained black powder was dispersed in 30 mL of H_2O containing 0.1 mol hydrogen fluoride (HF) and stirred for 2 h. Finally, the product was collected by centrifugation and washed repeatedly with H_2O and ethanol and dried under vacuum at 60 ˚C. Elemental sulfur was impregnated into

either the NMC or MC hosts by a simple melt-diffusion method. In a typical procedure, the host and sulfur were mixed thoroughly, and the mixture was treated at 155 ˚C for 12 h in a sealed vial.

4.2.3 Fabrication of free-standing NH_2-MOF@GO interlayer:

GO nanosheets were prepared according to previous method.[159] NH_2-MOF@GO membrane were prepared by a simple vacuum filtration method. First, a stable aqueous dispersion of NH_2-MOF was slowly added to another stable GO suspension in ethanol/water. Then, the resulting homogeneous suspension was filtered through a mixed cellulose ester filter paper, followed by air-drying, and peeling from the filter paper. The areal loading for NH_2-MOF and GO were controlled at 0.12 and 0.08 mg cm^{-2}, respectively.

4.2.4 Materials Characterization:

X-ray diffraction (XRD) patterns of the as-prepared materials was recorded with a Bruker D8 Discovery X-ray diffractometer. The morphology and structure of the composites were captured by FE-SEM (Zeiss Supra 55VP FESEM) and HR-TEM (Tecnai-G2 F30 S-Twin, 300 kV). Raman spectroscopy measurement of the composite was conducted on a confocal MicroRaman spectrometer with a Lab RAM HR system (Renishaw inVia) using a 632.8 nm He-Ne laser source. X-ray photoelectron spectroscopy (XPS) analyses were performed on an ESCALAB250Xi (Thermo Scientific, UK) equipped with monochromatic Al Kα radiation (energy 1486.68 eV). The FTIR spectra of the samples were recorded with a Nicolet 6700 spectrometer. Thermogravimetric analysis (TGA) was carried out with a thermogravimetry-differential thermal analysis (TG-DTA) system (SDT 2960) at a heating rate of 10 ˚C min^{-1} under N_2 atmosphere from room temperature to 500 ˚C. The specific surface areas were calculated by gas sorption technique with a Micromeritics Flex3 analyzer based on BET method. All samples for ultraviolet-visible (UV-Vis) spectroscopy were prepared, sealed inside an argon filled glove box, and then analyzed with a

Cary- 60 UV-Vis spectrophotometer in the spectral range of 300-1000 nm. Li_2S_6 solution was prepared by dissolving sulfur and Li_2S at a molar ratio of 5:1 was added to an appropriate amount of 1, 3-dioxolane (DOL) and 1, 2-dimethoxy ethane (DME) and stirred at 65 ˚C for 24 h in an argon-filled glove box.

4.2.5 Battery assembly and electrochemical characterization:

The slurry for Li-S battery electrodes was prepared by mixing 80 % NMC-S / MC-S composite as active material, 10 % carbon black (Super P, Sigma-Aldrich) as conductive additive, and 10 % poly (vinylidene difluoride) (PVDF, Sigma-Aldrich) as a binder in N-methyl 2-pyrrolidone (NMP) to form a slurry. The slurry was then cast onto a carbon-coated aluminum foil, followed by drying at 60 ˚C under vacuum for 12 h. For Li-S batteries, the active mass loading of sulfur was controlled between 1.5 ~ 1.8 mg cm^{-2}. Meanwhile, for Li-S batteries, electrodes with high a sulfur loading about ~ 2.7, ~ 3.2 and ~ 4.6 mg cm^{-2} were also fabricated. Finally, the CR2032 coin-type cells were assembled inside an Ar-filled glove box and cycled at 1.7 - 2.8 V (1 C = 1672 mAh g^{-1} based on the active mass of sulfur) on a LAND CT2001A charge-discharge system. The electrolyte was 1.0 M lithium bis (trifluoromethanesulfonyl) imide (LiTFSI, 99.95%, Aldrich) and 0.1 M $LiNO_3$ in 1:1 (v/v) mixed solvent of 1, 3-dioxolane (DOL) and 1, 2-dimethoxy ethane (DME). The volume of electrolyte injected into the Li-S cells was controlled at about 10 µL mg^{-1}_{sulfur}. Polypropylene (Celgard 2400) were used as a separator for Li-S batteries. For the Li-S cells with NH_2-MOF@GO interlayer, the freestanding NH_2-MOF@GO membrane was inserted in between the sulfur cathode and polypropylene separators during battery fabrication. Electrochemical stability of NH_2-MOF@GO interlayer against Li-anode was tested by performing CV within the potential range of 1.7 - 2.8 V vs. Li/Li^+ at a scan rate of 0.2 mV s^{-1}. CV and EIS were checked with a Biologic VMP3, and all electrochemical experiments were carried out at 25 ˚C.

4.3 Results and Discussion

The synthetic route of NMC-S is schematically illustrated in **Figure 4.1**. The initial NH_2-MOF was prepared by a solvothermal reaction between $ZrCl_4$ as metal source, and 2-aminoterepthalic acid (NH_2-BDC) as the organic linker. Afterward, a ZrO_2@N-doped carbon (abbreviated as ZrO_2@NMC) composite was obtained *via* carbonization of the NH_2-MOF (**Figure 4.1**, middle panels). The metal centre of the MOF *in situ* converted into ZrO_2 by reacting with the carboxylate groups, and the amidogen groups of the linker provided N-dopant sites during pyrolysis. Furthermore, the ZrO_2 nanoparticles were removed by HF-etching, leaving an N-doped micro/mesoporous carbon (abbreviated as NMC) with high active surface area. Successively, sublimed sulfur was impregnated into NMC by a melt-diffusion method to obtain NMC-S (**Figure 4.1**, lower panels). Furthermore, we combined NH_2-MOF and GO to construct a free-standing NH_2-MOF@GO permselective membrane by a simple vacuum filtration technique (**Figure 4.1**, upper panels). The NMC-S cathode and NH_2-MOF@GO interlayer were integrated together to fabricate Li-S cells. X-ray diffraction (XRD) data in **Figure 4.2** confirmed the well-crystallinity of NH_2-MOF. After calcining at 800 ˚C under Ar flow, the diffraction peaks of NH_2-MOF completely disappeared, while the new peaks appeared can be assigned to ZrO_2 (JCPDS card no 00-007-0337), indicating the formation of ZrO_2@NMC. After the HF treatment, the extinction of ZrO_2 peaks confirms the successful etching, leaving the MOF-derived amorphous NMC skeleton. As shown in **Figure 4.2**, the XRD of NMC-S did not show any characteristic peak for sulfur, implying that the sulfur particles are amorphous and completely absorbed by the porous carbon structure.

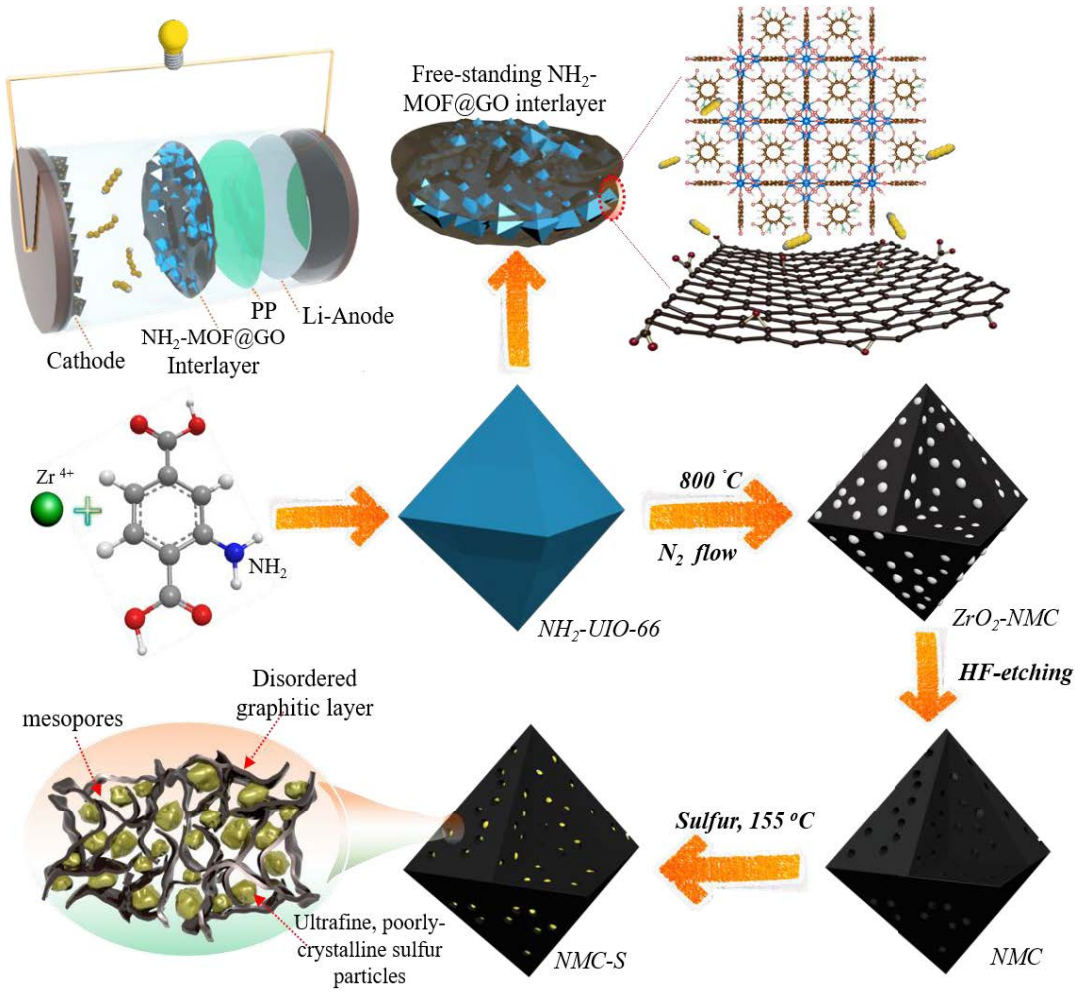

Figure 4.1 Schematic illustration of the Li-S cell with a NH_2-MOF@GO interlayer (upper panels), and the synthesis of NMC and NMC-S composite (middle and lower panels).

MC-S and NMC-S were examined with Raman spectroscopy analysis and displayed in **Figure 4.3**. In agreement with the XRD result, no typical Raman signal of sulfur was noticed in both the composites, indicating that the sulfur particles are perfectly impregnated into the carbon structure and are too small to be detected by Raman due to phonon confinement effect.[160] Two peaks appeared around 1,320 and 1,587 cm^{-1} are attributed to the D-band (disordered induced phonon mode) and G-band (graphite band) of the carbon structure. [161]

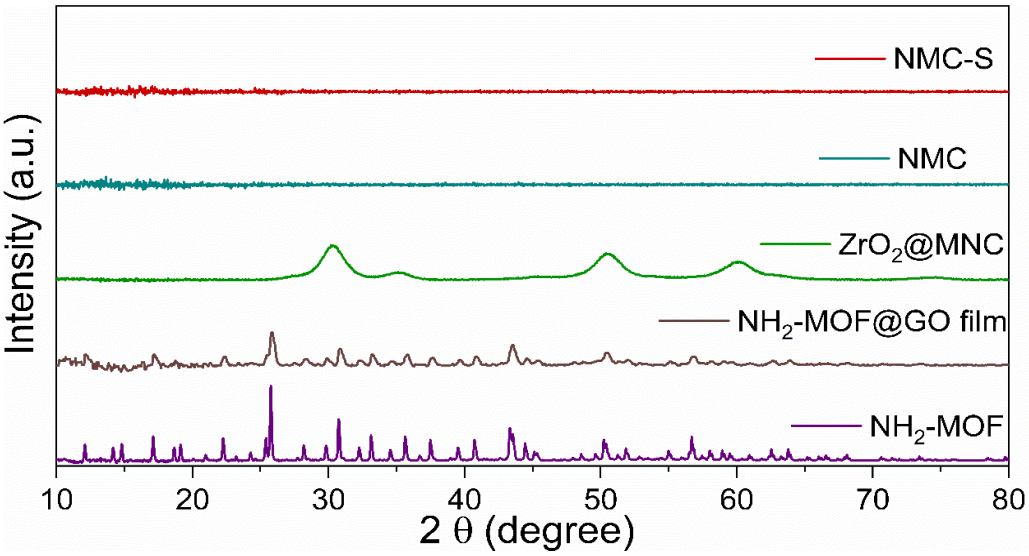

Figure 4.2 XRD pattern of the as-prepared samples.

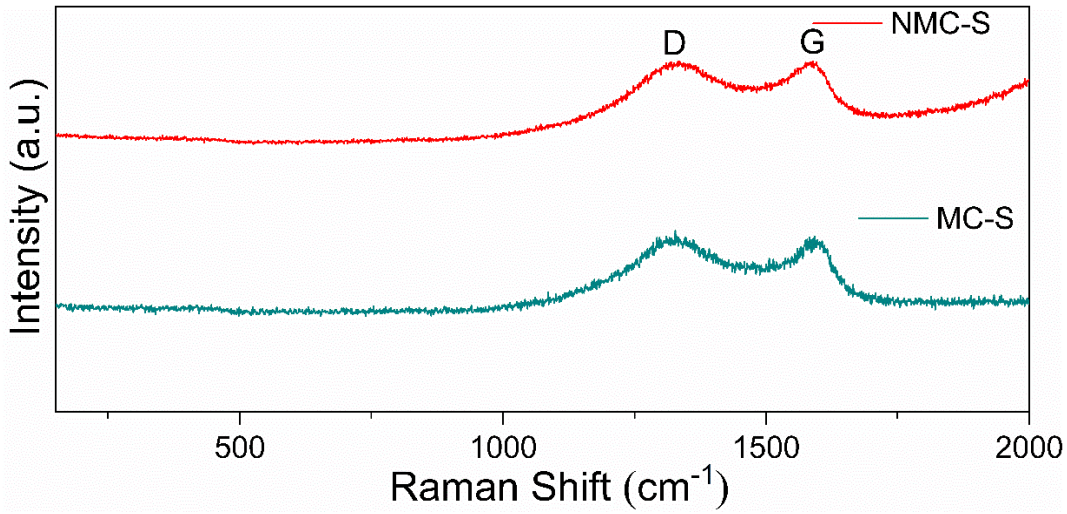

Figure 4.3 Raman spectra of the NMC-S and MC-S composites. No typical sulfur signals appeared in the spectrum for both the composites, confirming that the sulfur particles are completely impregnated into the carbon network.

All the samples were further characterized by Fourier transform infrared spectra (FT-IR, **Figure 4.4**). The FT-IR peaks for NH_2-MOF within 600 - 800 cm^{-1} are attributed to Zr-O_2 as longitudinal and transverse modes.[12] The peak at 1250 cm^{-1} corresponds to C-NH_2, while the peaks at 1080

and 1620 cm^{-1} are associated with -NH_2 rocking and scissoring vibrations, respectively.[3] For the NH_2-MOF@GO film, a new peak appearing around 1047 cm^{-1} belongs to the alkoxy C-O stretching vibration of GO.[142] The Brunauer-Emmett-Teller (BET) surface area of the as-prepared samples were obtained by recording nitrogen adsorption-desorption isotherms at 77K (**Figure 4.5a**).

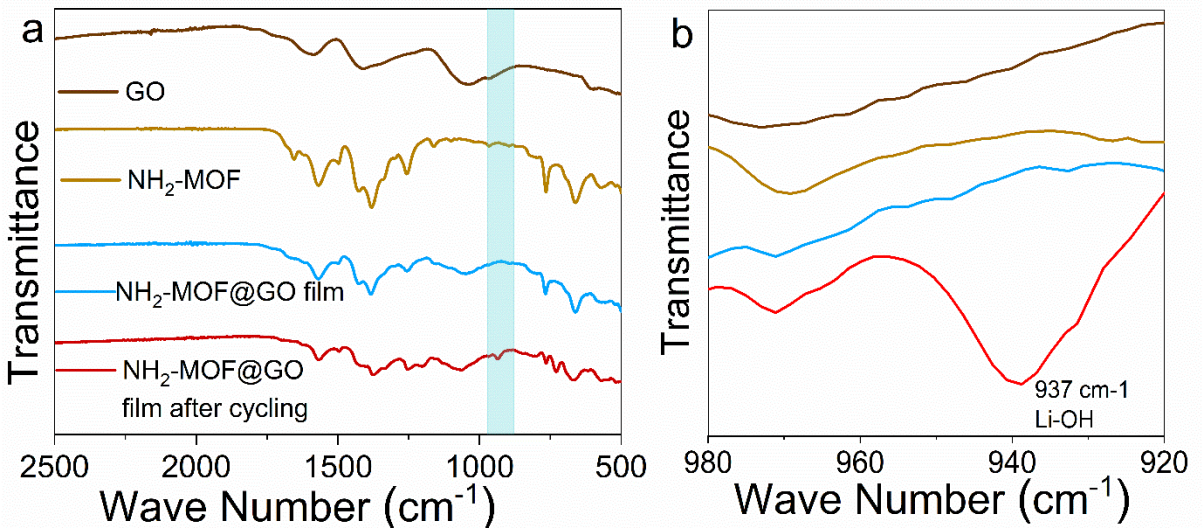

Figure 4.4 (a) FI-IR analysis of GO, NH_2-MOF, and NH_2-MOF@GO interlayer before and after cycling. (b) magnified FT-IR spectra in the region between 920 cm^{-1} to 980 cm^{-1}.

The BET surface area for NH_2-MOF was measured to be 618 m^2 g^{-1}. In contrast, after carbonization and successful removal of ZrO_2, the BET surface area for the NMC sample remarkably increased to 1347 m^2 g^{-1}. We also noticed that the nitrogen uptake for the NMC sample steeply increased at low relative pressure, indicating the presence of substantial micropore structures (< 2 nm). This observation was in accordance with the pore size distribution obtained from adsorption data calculated by the BJH method (**Figure 4.5b**), which showed inherent micropores with diameter centering at ~ 1.60 nm and enormous mesopores of about ~ 3.97 nm with a large pore volume of ~ 0.64 cm^3 g^{-1}. It is believed that the host material with high surface

area and abundant micro/mesopore network can endow enough exposed active sites for a substantial amount of active mass loading. Also, such a network provides a sophisticated electron-transfer pathway and superior structural stability for energy-storage applications.

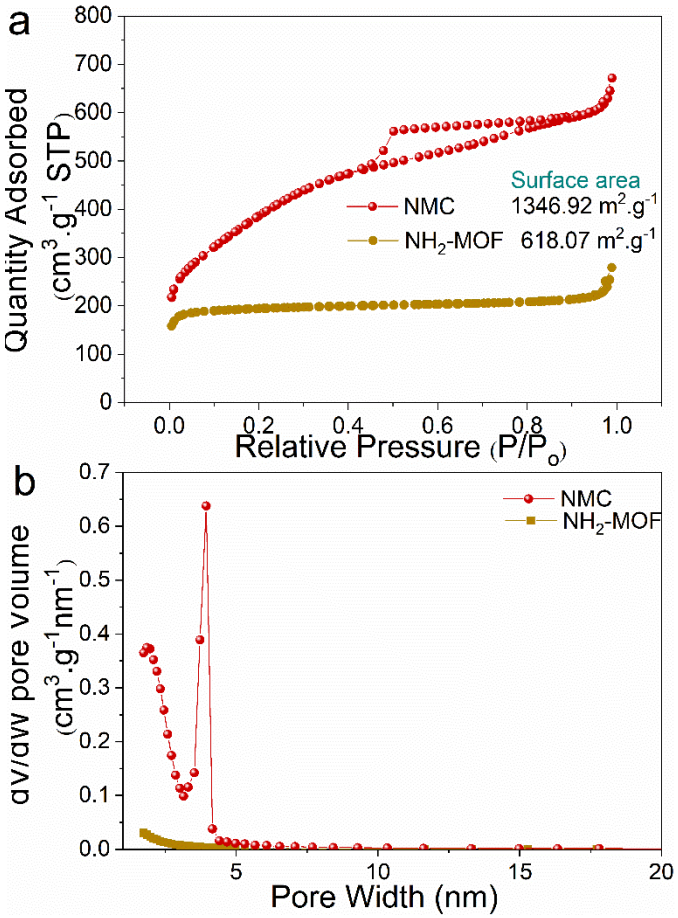

Figure 4.5 (a) N_2 adsorption-desorption isotherm of NH_2-MOF and NMC host and (b) BJH pore size distribution for NMC and NH_2-MOF.

The morphologies of the samples were investigated with scanning electron microscopy (FE-SEM) and transmission electron microscopy (TEM). The FE-SEM image of NH_2-MOF in **Figure 4.6a** reveals uniform octahedral shape with a narrow size distribution of ~ 200 nm. Thermal treatment before HF-etching did not destroy the well-defined octahedral morphology of NH_2-MOF and even maintained for NMC (**Figure 4.6b**). **Figure 4.6c** displays the resultant NMC after impregnating

sulfur. No large sulfur particles were noticed on the surface of the nano-octahedra, which manifests that the sulfur is uniformly infiltrated into the highly porous network of NMC. The TEM image of NMC-S in **Figure 4.6d** displays the octahedral morphology, which is consistent with the FE-SEM analysis. More importantly, no sign of agglomerated sulfur particles is noticed in- or outside the carbon-core.

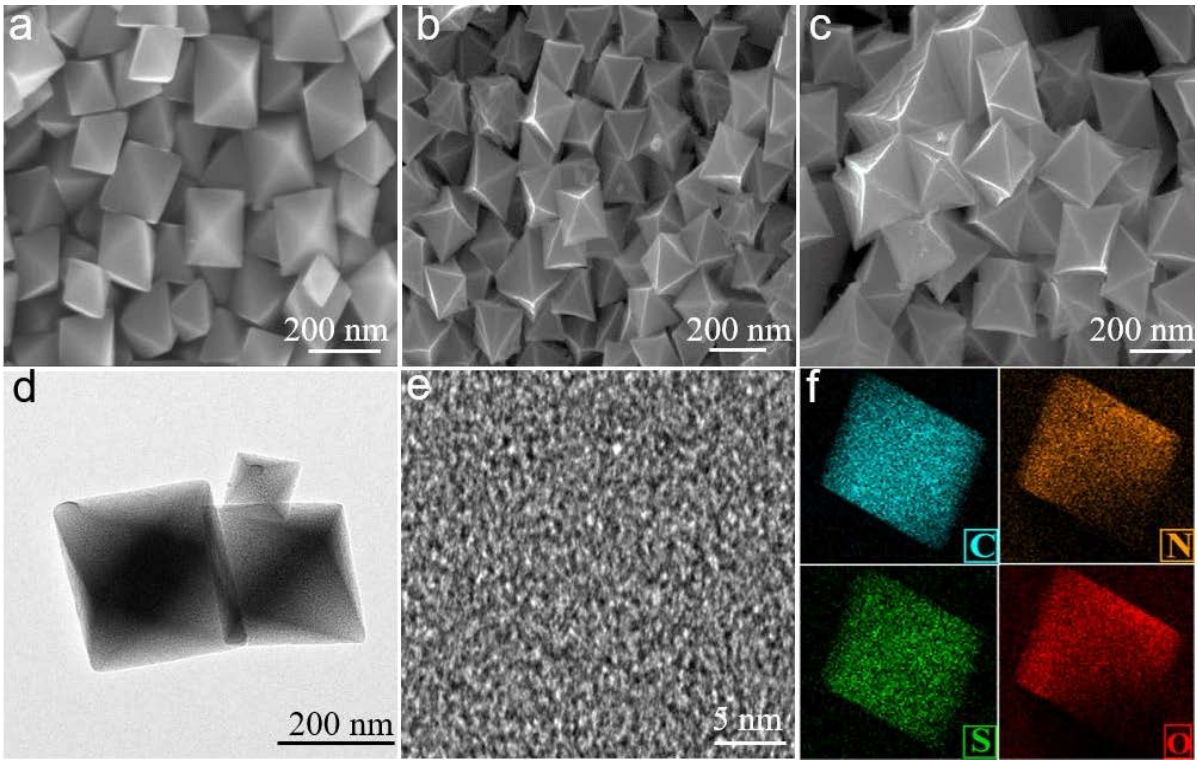

Figure 4.6 FESEM images of (a) NH_2-MOF, (b) NMC after thermal treatment and HF etching and (c) NMC-S composite. (d) TEM and (e) HRTEM images of NMC-S composite. (f) Elemental colour mapping of NMC-S displays a uniform distribution of C, N, S and O in the NMC-S composite.

This feature is crucial to realize a high-performance Li-S battery since poor capacity and irreversible capacity loss would occur if the active material agglomerates or non-uniformly covers the conductive matrix, which can block the charge-transfer and ion-transport. [162] Furthermore, no

crystalline sulfur particles were noticed in high-resolution TEM (HR-TEM, **Figure 4.6e**) image, which indicates that the sulfur particles are amorphous in nature and the same has been substantiated by the XRD results. It is worth mentioning that not only the ultrafine and poorly crystalline sulfur particles are obtained from the confinement of porous host, but also the extraordinary accessibility and stability endowed by the carbon shell could benefit the application of NMC-S as a cathode for Li-S battery applications. The elemental mapping of NMC-S (**Figure 4.6f**) confirms the uniform distribution of C, N, O, and S through the whole octahedra. To determine further chemical composition and valence of the composites, X-ray photoelectron spectroscopy (XPS) was performed. The XPS data of NH_2-MOF shown in **Figure 4.7a** confirm the presence of Zr, C, N, O. The N1s spectra for NH_2-MOF (**Figure 4.7d**) can be deconvoluted into two peaks: one peak at 398.6 eV can be assigned to -NH_2, while the other at 399.7 eV may originate from the interaction between the amidogen functionalities and protons. [163] The deconvoluted C 1s spectrum of NMC-S in **Figure 4.8a** shows four peaks at 284.8, 286.2, 287.8 and 289.3 eV, corresponding to C-C / C=C, C-O / C-N, C=O and O-C=O, respectively. [164] The magnified N 1s spectrum (**Figure 4.8b**) can be deconvoluted into three peaks: pyridinic N, pyrrolic N, and quaternary N with binding energies of 399.2, 400.4, and 401.9 eV, respectively. According to previous reports, such N-dopants present in the carbon skeleton not only increase the electronic conductivity for better sulfur utilization, but also act as active chemical sites to interact with polysulfides.[150] In the S 2p region of the NMC-S composite (**Figure 4.8c**), the S $2p_{3/2}$ (163.9 and 165.4 eV) and S $2p_{1/2}$ (165.1 and 166.6 eV) spin-orbit splitting are attributed to S-S and S-O species, respectively. [165]

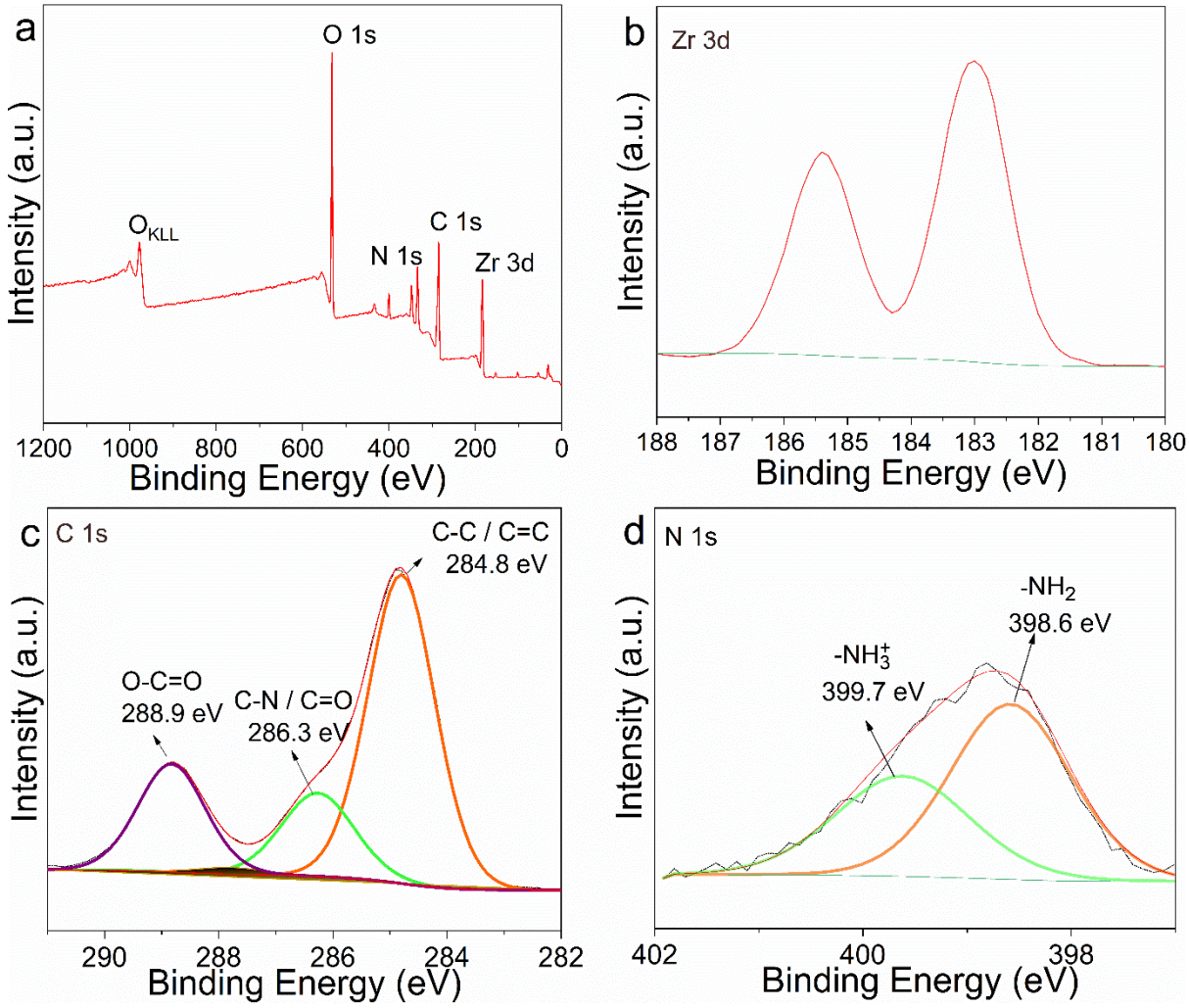

Figure 4.7 XPS analysis for NH_2-MOF: (a) XPS survey scan for (b) Zr 3d, (c) C 1s, and (d) N 1s regions.

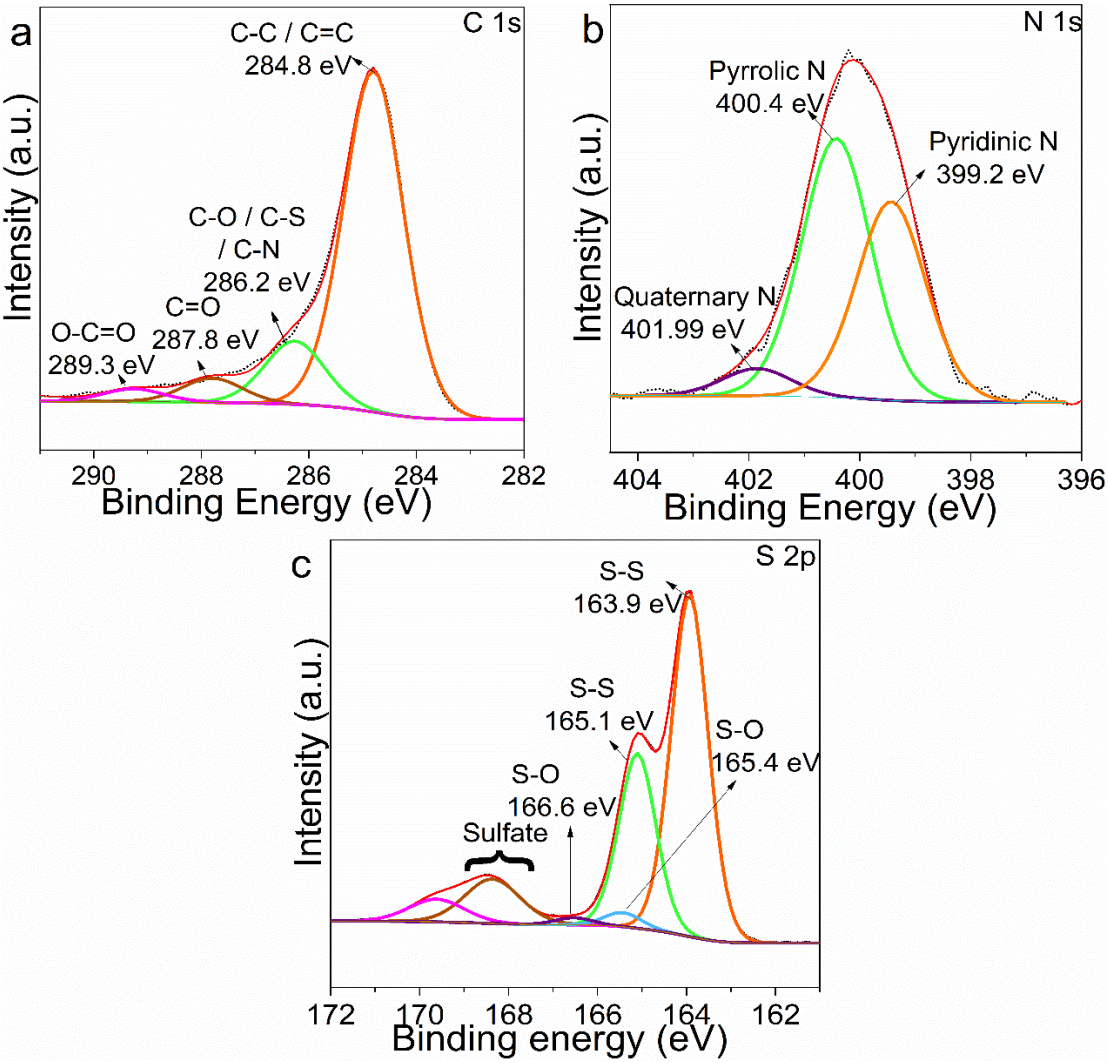

Figure 4.8 High-resolution XPS spectra of (a) C1s, (b) N 1s, and (c) S 2p for the NMC-S composite.

Another S 2p peak appearing around 168.4 eV can be ascribed to sulfate species formed by oxidation of sulfur in air. Thermogravimetric analysis (TGA), shown in **Figure 4.9,** revealed that the sulfur loadings of NMC-S and MC-S composites were as high as 68.1 and 65.6 wt.%, respectively.

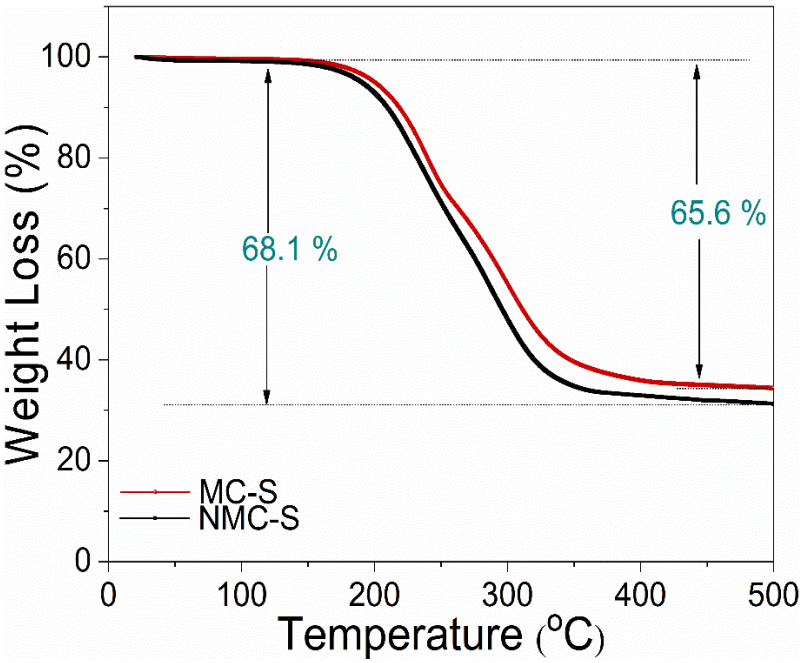

Figure 4.9 TGA analysis of as-prepared MC-S and NMC-S composites.

The fabrication of NH_2-MOF@GO free-standing membrane via vacuum filtration technique is shown in **Figure 4.10**. The stable aqueous dispersion of NH_2-MOF was first added to a stable GO suspension in ethanol/water. The NH_2-MOF@GO membrane was prepared by a filtration of the resulting homogeneous suspension through mixed cellulose ester filter paper, followed by air-drying and peeling off from the filter paper. The fracture edges of NH_2-MOF@GO membrane, when imaged with FE-SEM (**Figure 4.11a**), revealed a well-packed structure with a thickness about 14 µm. The magnified FE-SEM image (**Figure 4.11b**) of the cross-section shows a layer-by-layer (LBL) assembly between NH_2-MOF nano-octahedra and GO nanosheets. Interaction between the amidogen (-NH_2) moieties of the NH_2-MOF and oxygen-containing functional groups of GO serves as the driving force to construct LBL type assembly.

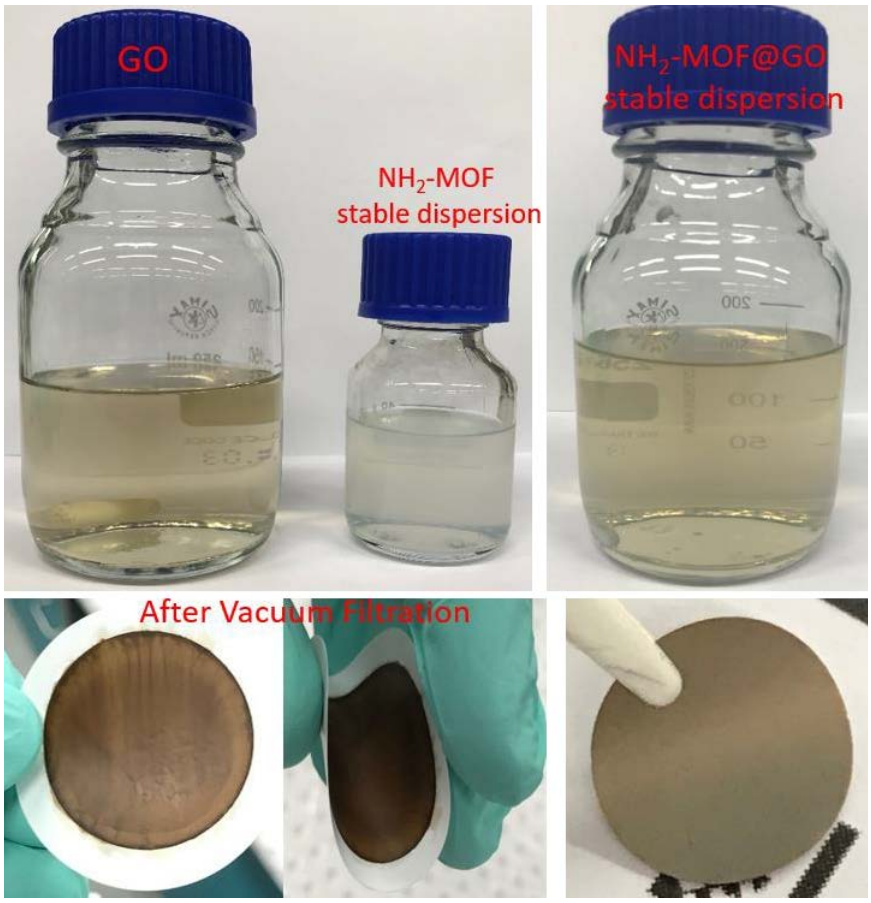

Figure 4.10 Optical images, demonstrating the fabrication techniques of free-standing NH_2-MOF@GO interlayer.

Notably, the NH_2-MOF particles alternatively stacked between GO layers not only prevent the stacking of GO sheets, but also induce enough porosity for electrolyte retention in the separator, which facilitates Li^+ diffusion during electrochemical cycling. The top surface of the separator in **Figure 4.11c** shows that the NH_2-MOF particles are distributed uniformly across the separator. This is further confirmed by the elemental colour mapping shown in **Figure 4.11d-i**. The corresponding elemental maps show the even distribution of the elementals Zr, N, which are from the NH_2-MOF.

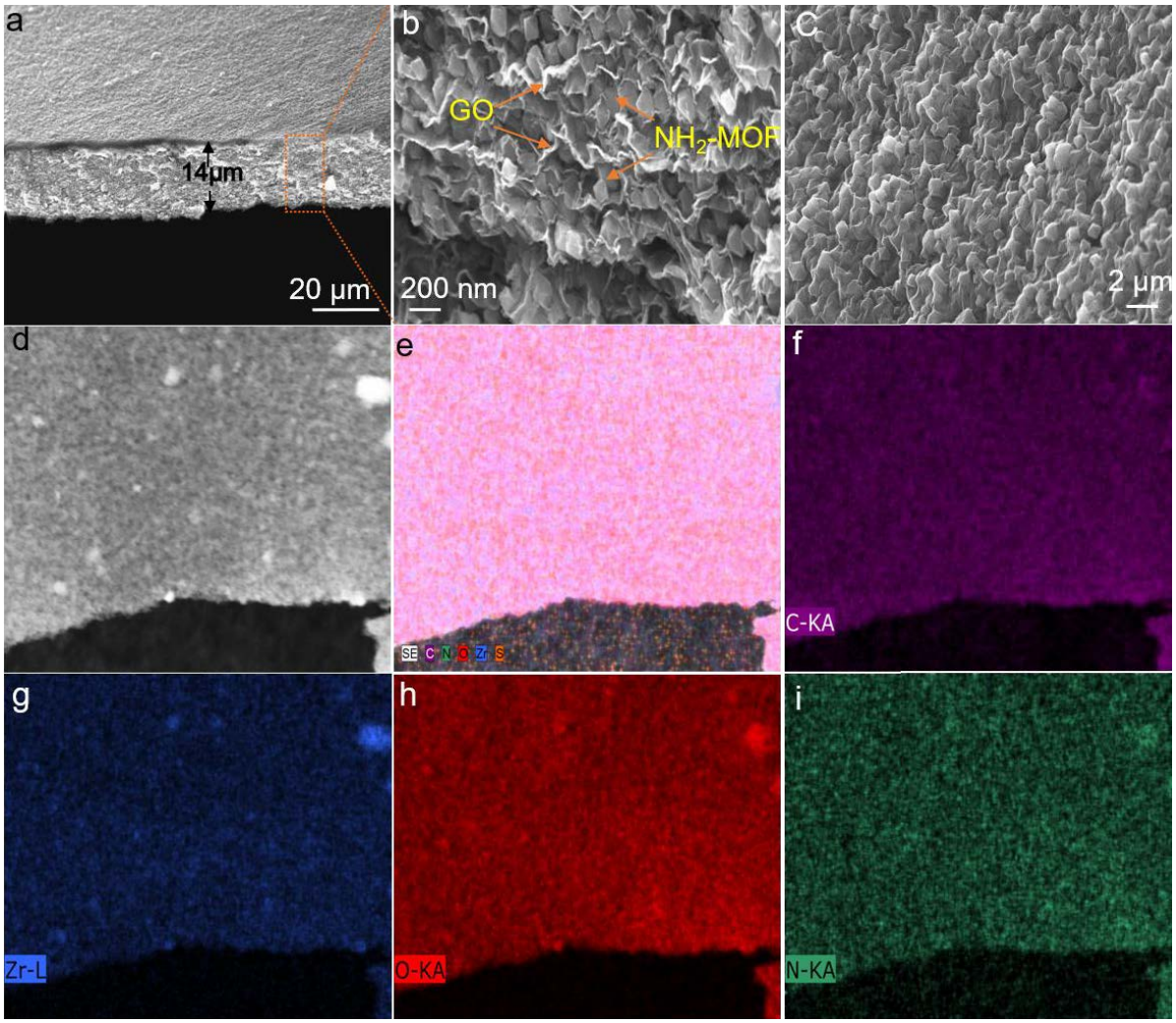

Figure 4.11 (a) FESEM image of freestanding NH_2-MOF@GO interlayer. (b) cross-section and (c) top surface morphologies of NH_2-MOF@GO interlayer. (d) FESEM and EDX elemental colour mapping of the free-standing NH_2-MOF@GO interlayer, showing a uniform distribution of (f) C, (g) Zr, (h) O and (i) N elements.

To demonstrate the adsorption capabilities of the as-prepared samples to polysulfide, an equal amount of NH_2-MOF@GO, NH_2-MOF, and NMC were separately immersed into the same amount of polysulfide solutions containing 2×10^{-3} M Li_2S_6 in 1,3 dioxolane/ dimethoxyethane. After

settling for a few hours, NH_2-MOF@GO thoroughly decolorizes the Li_2S_6 solution (inset of **Figure 4.12a**), indicating a stronger chemical binding interaction of NH_2-MOF@GO to polysulfide.

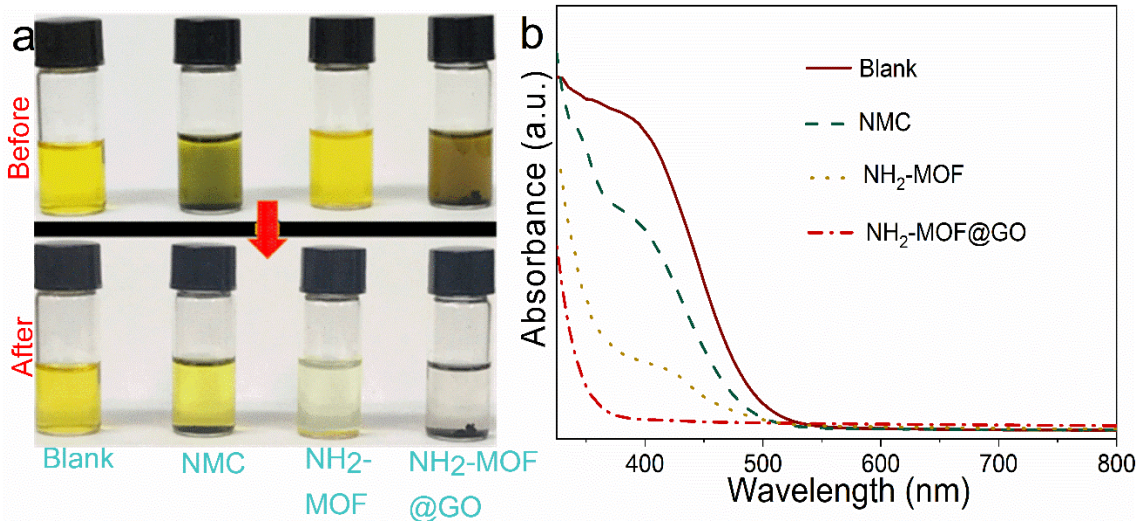

Figure 4.12 (a) Photograph and (b) UV-Vis absorption spectra of supernatant Li_2S_6 solution after the adsorption test.

NH_2-MOF/ Li_2S_6 solution also shows a significant change in colour, while the yellow colour of Li_2S_6 was still visible in NMC/ Li_2S_6. UV-vis spectra of the supernatants were also recorded to investigate the concentration changes of Li_2S_6 solutions after exposing to the adsorbents (**Figure 4.12b**). It can be seen that the absorption peak of Li_2S_6, which appears around 420 nm for blank Li_2S_6 solution, completely disappeared for NH_2-MOF@GO. In contrast, the Li_2S_6 absorption peak exists for both the NH_2-MOF and NMC, although the former displayed much reduction in peak intensity. Therefore, it appears that NH_2-MOF@GO can provide the strongest chemical binding to the polysulfide among all the samples due to the ample number of nucleophilic functional groups present in both the NH_2-MOF and GO. On the other hand, NH_2-MOF manifests better interaction with polysulfide compared to NMC sample, which can probably be attributed to the combined effect from the well-exposed surface -NH_2 groups and the metal centre of the NH_2-MOF, as both

have higher affinity to polysulfide. Furthermore, additional evidence for the chemical interaction between NH_2-MOF and Li_2S_6 is provided by the XPS analysis of NH_2-MOF before and after the Li_2S_6 adsorption test.

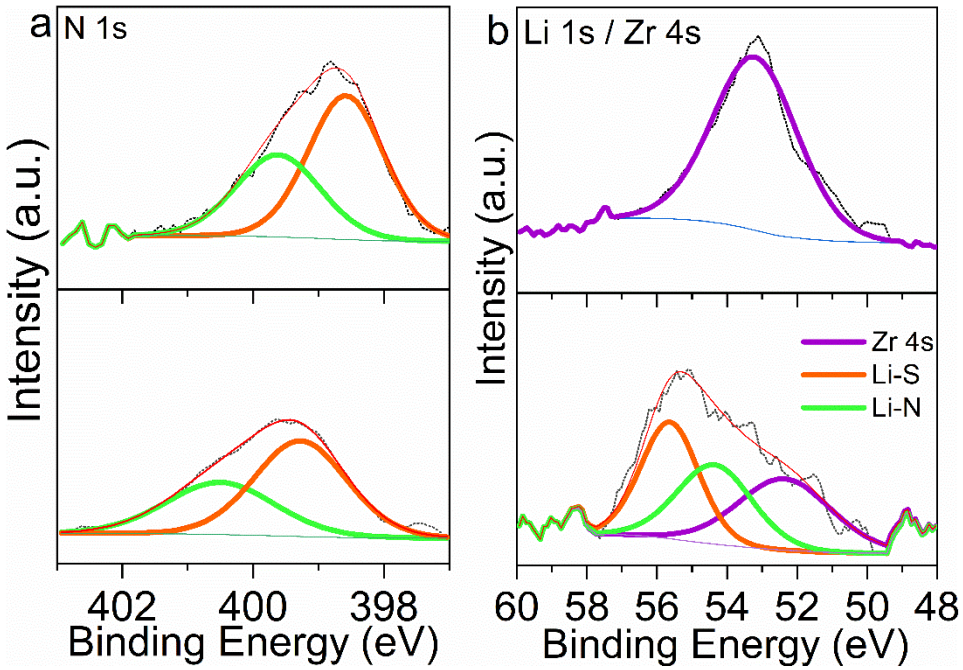

Figure 4.13 XPS spectra of the bare NH_2-MOF and Li_2S_6-treated NH_2-MOF, (a) N 1s, and (b) Li 1s / Zr 4s.

As shown in **Figure 4.13a**, the N 1s peak for NH_2-MOF is slightly moved to higher binding energy after exposing to Li_2S_6, indicating the interaction between Li^+ and -NH_2 functional groups. After the Li_2S_6 adsorption, the Li 1s and Zr 4s peak can be deconvoluted into three peaks (**Figure 4.13b**). The first peak located at 52.3 eV is identified as Zr 4s peak, which is shifted by 0.8 eV toward lower binding energy perhaps owing to the interaction between the Zr-metal of the NH_2-MOF and Li_2S_6. The other two peaks appearing at 55.3 and 54.5 eV can be attributed to Li-S and Li-N bonds, respectively.[166, 167] Electrochemical stability of NH_2-MOF@GO film, which is indispensable for the interlayer, was evaluated by cyclic voltammetry (CV). When tested against lithium, no peak was detected within 1.7 – 2.8 V (**Figure 4.14**), indicating the NH_2-MOF@GO

membrane is electrochemically stable to lithium within the operating voltage range. To elucidate the function of the NH_2-MOF@GO interlayer on controlling the growth of Li dendrites, cycling of symmetric Li//Li cells with different separators were performed under the same current density of 1 mA cm^{-2} and with a capacity limit of 1 mAh cm^{-2}.

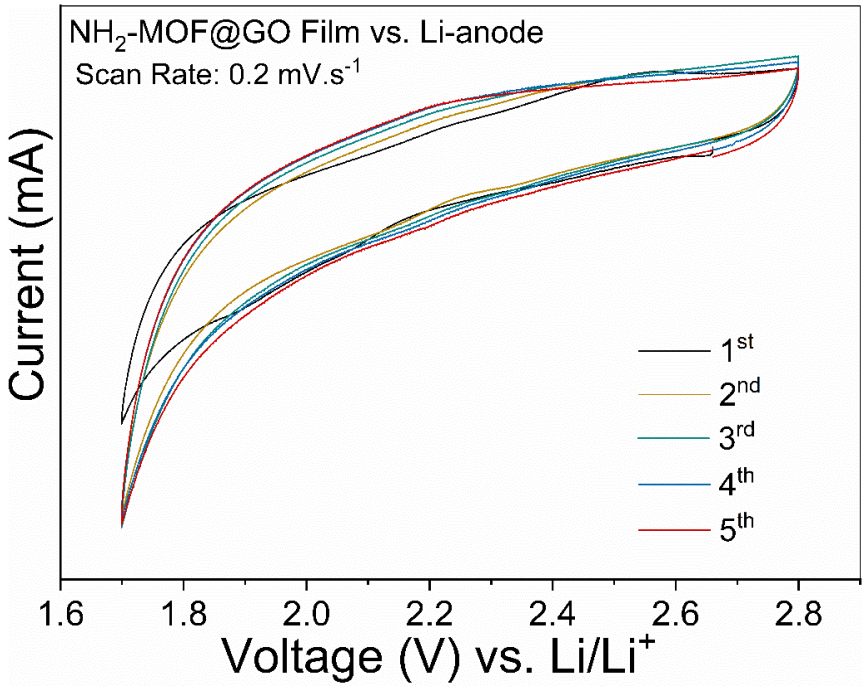

Figure 4.14 CV curves of NH_2-MOF interlayer for first five cycles when tested against Li-anode within the potential range of 1.7 - 2.8 V vs. Li/Li^+ at a scan rate of 0.2 mV s^{-1}.

As shown in **Figure 4.15**, for the symmetric cell without an interlayer, the hysteresis between the stripping/plating voltages increased just after 150 h, indicating degraded Li surface caused by uncontrollable Li dendrite growth and subsequent disruption and reformation of solid electrolyte interface (SEI) layers.

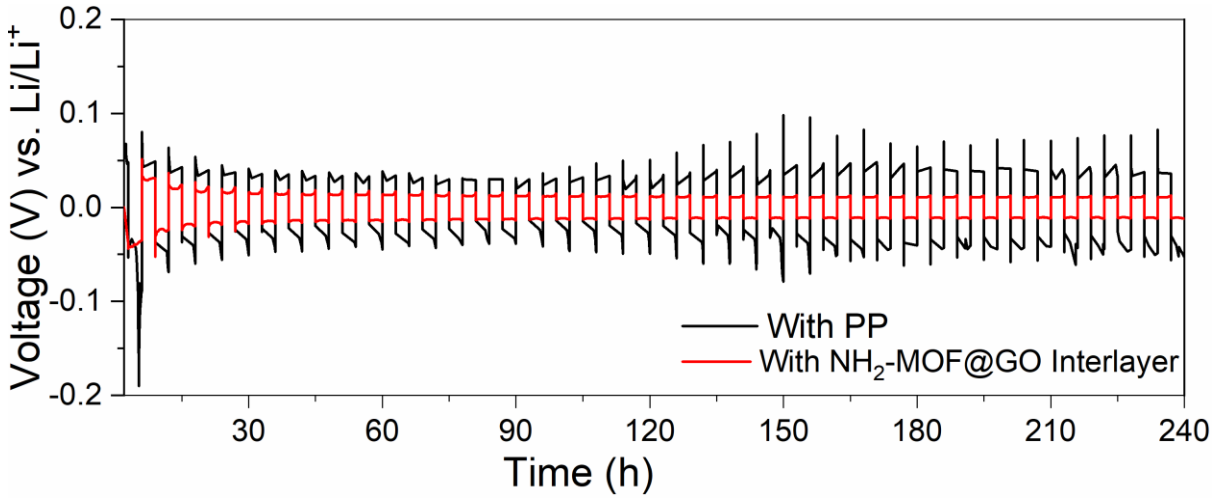

Figure 4.15 Voltage-time profile of Li//Li symmetric cell with an NH_2-MOF@GO interlayer at 1 mA cm^{-2} with a capacity of 3 mAh cm^{-2}.

In contrast, the symmetric cell with the NH_2-MOF@GO interlayer demonstrates much lower voltage fluctuation and remains stable up to 240 h, which manifests in a more stable SEI and uniform Li-ion flux directed by the NH_2-MOF@GO film. [168] Before applying the NH_2-MOF@GO membrane as an interlayer for Li-S batteries, it is important to explore whether Li^+ can be diffused through the membrane, whilst it has already been proven that such unique combination can trap the polysulfide in both physical and chemical ways.

To elucidate this phenomenon, CV measurements of Li-S cells with and without the NH_2-MOF@GO interlayer at scan rates of 0.12 to 2.0 mV s^{-1} were conducted (**Figure 4.16a-d**) and are summarized in **Table 4.1**.

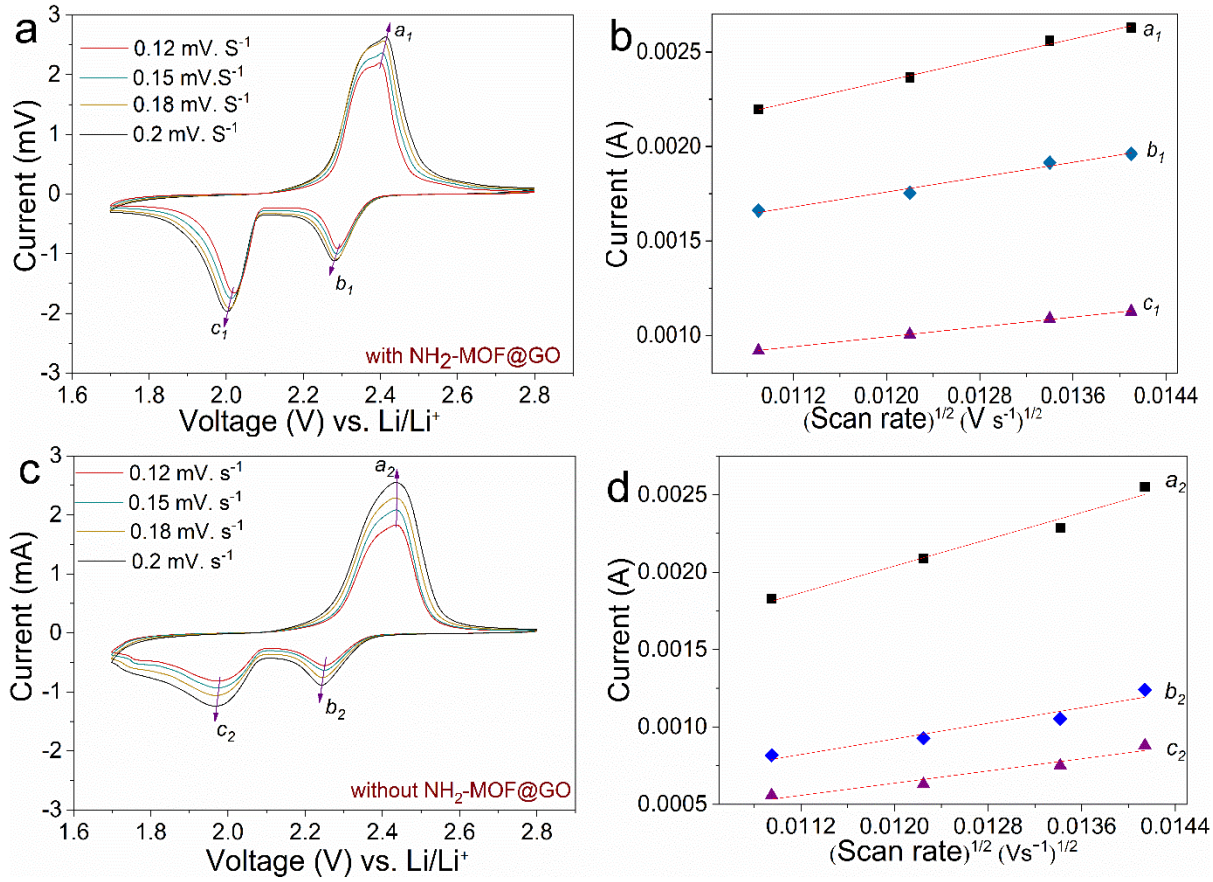

Figure 4.16 CVs at different scan rates and corresponding linear fits of the peak currents of Li-S batteries (a, b) with and (c, d) without the NH_2-MOF@GO interlayer.

The Li^+-ion conductivity of PP, with and without the NH_2-MOF@GO interlayer, was also measured by recording electrochemical impedance spectroscopy (EIS, **Figure 4.17**) and is given in **Table 4.1**. As it can be seen, the introduction of NH_2-MOF@GO as interlayer has a negligible effect on Li^+ diffusion and conductivity across the separator, rather blocking polysulfide from escaping to anode compartment. Therefore, we are confident that NH_2-MOF@GO separator would be an ideal ion sieve, allowing Li ions to pass through while preventing the escape of polysulfide into the anodic compartment.

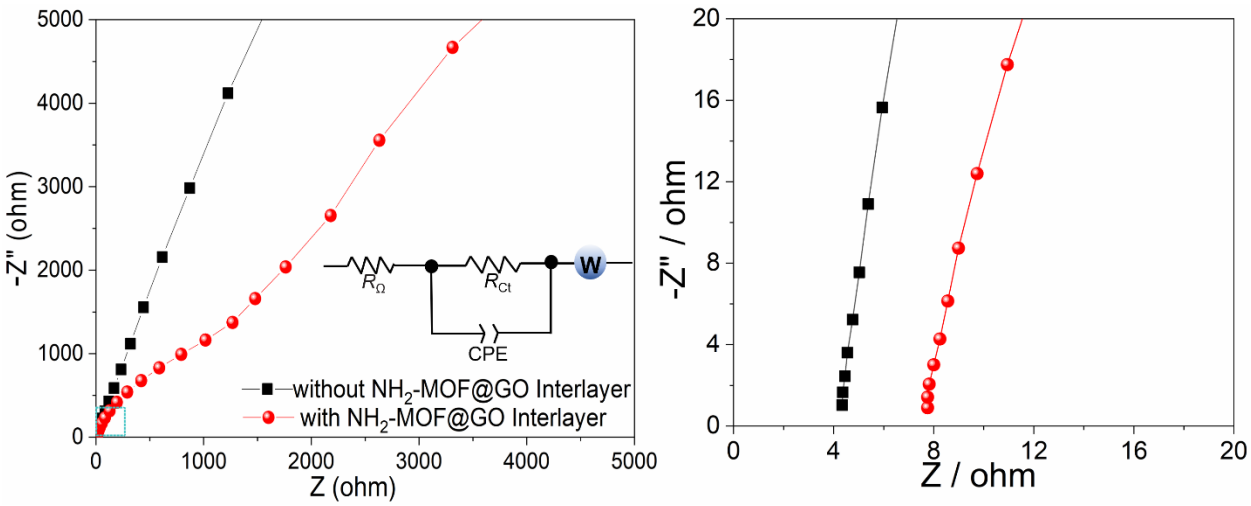

Figure 4.17 EIS spectra of Li-S batteries with different separators.

Table 4.1 Summary of the electrochemical parameters of PP separators with and without the NH_2-MOF@GO interlayer

	Ionic Conductivity (mS cm ^{1})	(*a*) D_{Li+} ($cm^2 s^{-1}$)	(*b*) D_{Li+} ($cm^2 s^{-1}$)	(*c*) D_{Li+} ($cm^2 s^{-1}$)
Pristine Separator (PP)	0.318	2.96×10^{-8}	6.16×10^{-9}	1.08×10^{-8}
With NH_2-MOF@GO Interlayer	0.261	1.80×10^{-8}	3.49×10^{-9}	8.86×10^{-9}

Figure 4.18 demonstrates the CV curves of the cell with NMC-S cathode and NH_2-MOF@GO interlayer at 0.2 mV s^{-1} within the potential window of 1.7 - 2.8 V vs. Li/Li^+. During the first cathodic scan, two reduction peaks were observed at around 2.27 and 2.01 V. The first reduction peak at 2.27 V is attributed to the reduction of S_8 to soluble S_8^{2-}, and then to S_6^{2-} and S_4^{2-}. The peak at 2.01 V is due to the reduction of soluble polysulfides to insoluble Li_2S_2 / Li_2S_2. Meanwhile, a strong oxidation peak appearing around 2.39 V is due to the conversion of Li_2S / Li_2S_2 into elemental S_8.[3] Most importantly, all the peaks for consecutive cycles were perfectly superimposed to each other, confirming stable electrochemical reaction.

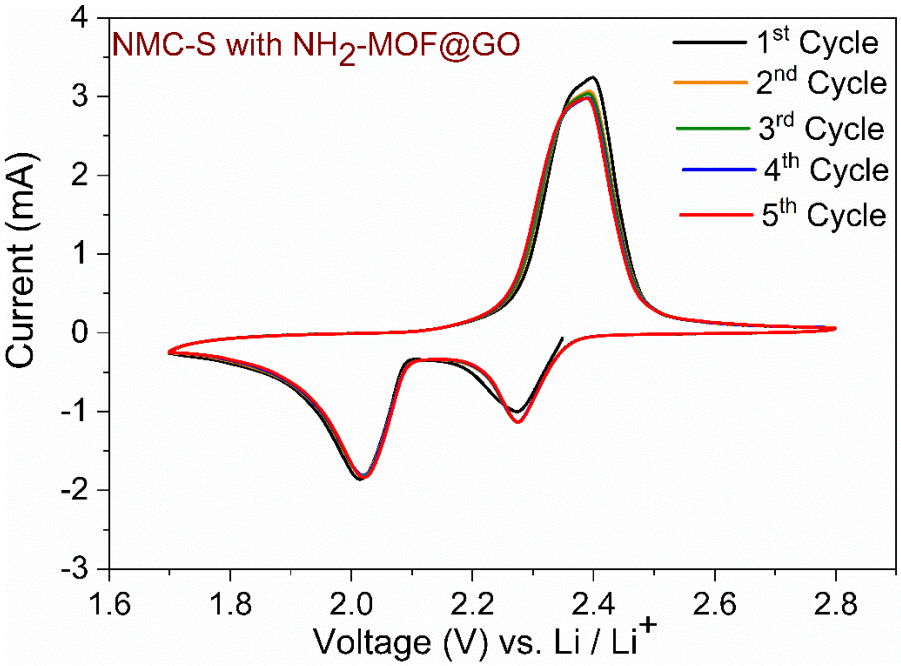

Figure 4.18 The CV data of the NMC-S cathode with NH_2-MOF@GO interlayer at 0.2 mV s^{-1}.

The galvanostatic discharge/charge profiles of the Li-S cell with the NMC-S cathode and NH_2-MOF@GO interlayer at different current densities are displayed in **Figure 4.19a**. Like CV curves, the discharge profile shows two plateaus, corresponding to the multi-step reduction of elemental S_8 to the final product Li_2S_2 / Li_2S. With the NH_2-MOF@GO interlayer, the Li-S battery maintains two distinct plateaus even when tested at a very high current rate of 3C. There was no significant increase in voltage polarization with increased current densities. This indicates a smooth electrochemical reaction of the Li-S battery with NH_2-MOF@GO interlayer. In contrast, the Li-S cells with the NMC-S cathode and PP separator show a significant voltage polarization (**Figure 4.19b**), which deteriorate further for MC-S cathodes with similar kind of separators (**Figure 4.19c**). **Figure 4.19d** displays the rate performances of the Li-S batteries with different separators.

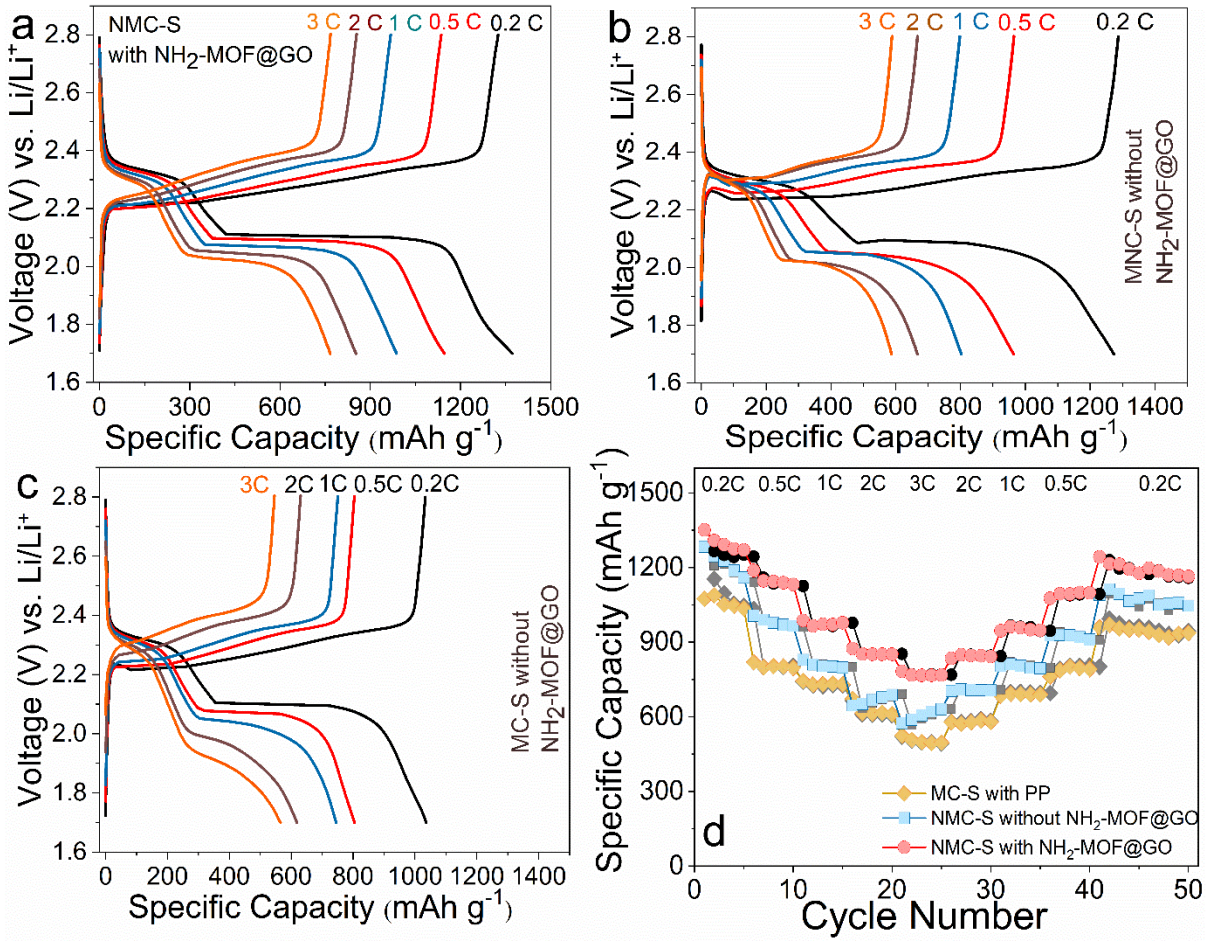

Figure 4.19 Galvanostatic discharge-charge profiles of (a) NMC-S with NH_2@MOF interlayer, (b) NMC-S with PP separator and (c) MC-S cathodes with the PP separator under different current densities. (d) Rate performances of as prepared cathodes with or without NH_2-MOF interlayer.

The NMC-S cathode with the NH_2-MOF@GO interlayer delivers high reversible capacities of 1318, 1146, 985, 862 and 769 mAh g^{-1} at 0.2, 0.5, 1, 2 and 3 C rates, respectively. This is remarkably higher than that with both the NMC-S and MC-S cathodes with the PP separator under the same current densities. More importantly, the Li-S cell with NH_2-MOF@GO interlayer retained almost 94.2 % of the initial capacity when the current rate was reversed back to 0.2C. The cycling performances of MC-S and NMC-S electrodes with or without the interlayer were evaluated at 0.5C rate and are represented in **Figure 4.20**. The NMC-S cathodes with the NH_2-

MOF@GO interlayer delivered a much higher discharge capacity of 1,155 mAh g^{-1} compared to 968 mAh g^{-1} when cycled only with the PP separator and retained almost 83.5 % (vs. 66.8 % with only PP separator) after the consecutive 200 cycles. On the other hand, the MC-S electrode with the PP separator exhibits an initial capacity of 873 mAh g^{-1} and retained only 61.3 % after the same number of cycles. The N-dopant sites present in the NMC-S cathode are beneficial for improving the redox reaction, reversibility of the system, and partial immobilization of the soluble polysulfides. [150]

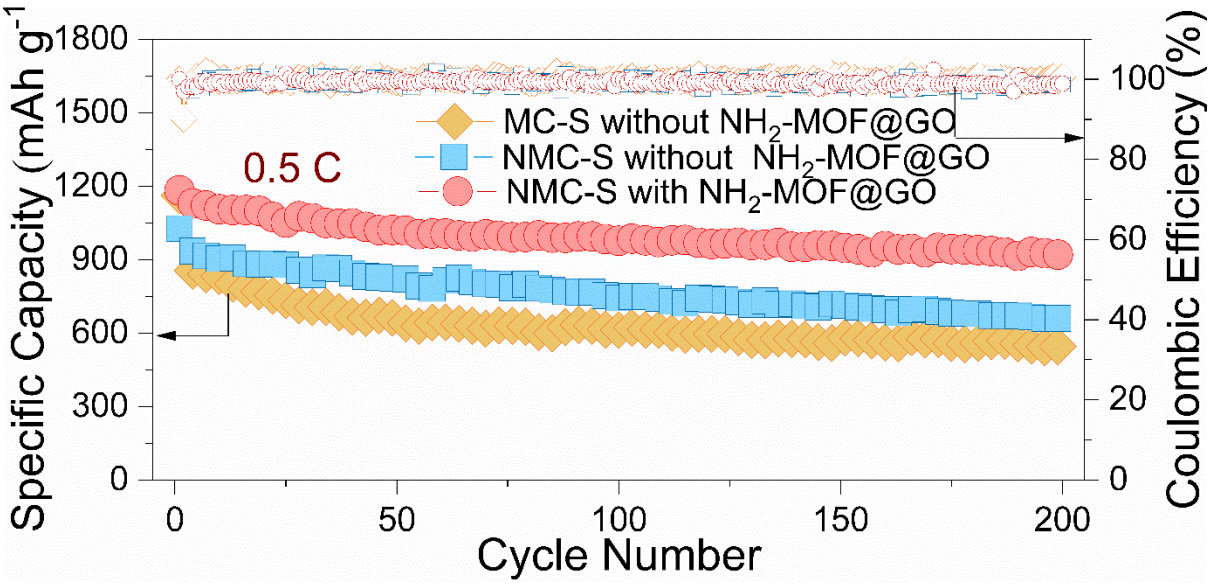

Figure 4.20 Cycling performance of MC-S and NMC-S cathodes with/without NH_2-MOF@GO interlayer at 0.5C rate.

The cell with the NH_2-MOF@GO interlayer also rendered long-term cycling stability at 1 C rate (**Figure 4.21a**). Initially, the cell delivered an average reversible capacity of 1015 mAh g^{-1} and after extensive 500 cycles, a capacity of 792 mAh g^{-1} was still preserved, corresponding to a cyclic decay rate of only 0.043 %. The Coulombic efficiency was maintained at about ~ 100 % all over the cycling. By contrast, NMC-S and MC-S electrodes with the pristine PP separator demonstrated low capacities of 849 and 822 mAh g^{-1}, respectively. After 500 cycles, the capacities decreased to

602 (0.060% decay) and 571 mAh g^{-1}(0.062 % decay), respectively. Targeting a practically viable Li-S system, cells with higher sulfur loadings were tested at a high rate of 0.5 C rate (**Figure 4.21b**). Remarkable reversible capacities of 1109, 977, and 825 mAh g^{-1} were obtained with the high sulfur loadings of 2.5, 3.2 and 4.6 mg cm^{-2}. The corresponding areal capacities can be estimated as 2.77, 3.13 and 3.86 mAh cm^{-2}, respectively. After 150 cycles, 81.5, 82.9 and 82.5 % of their initial capacity were recovered.

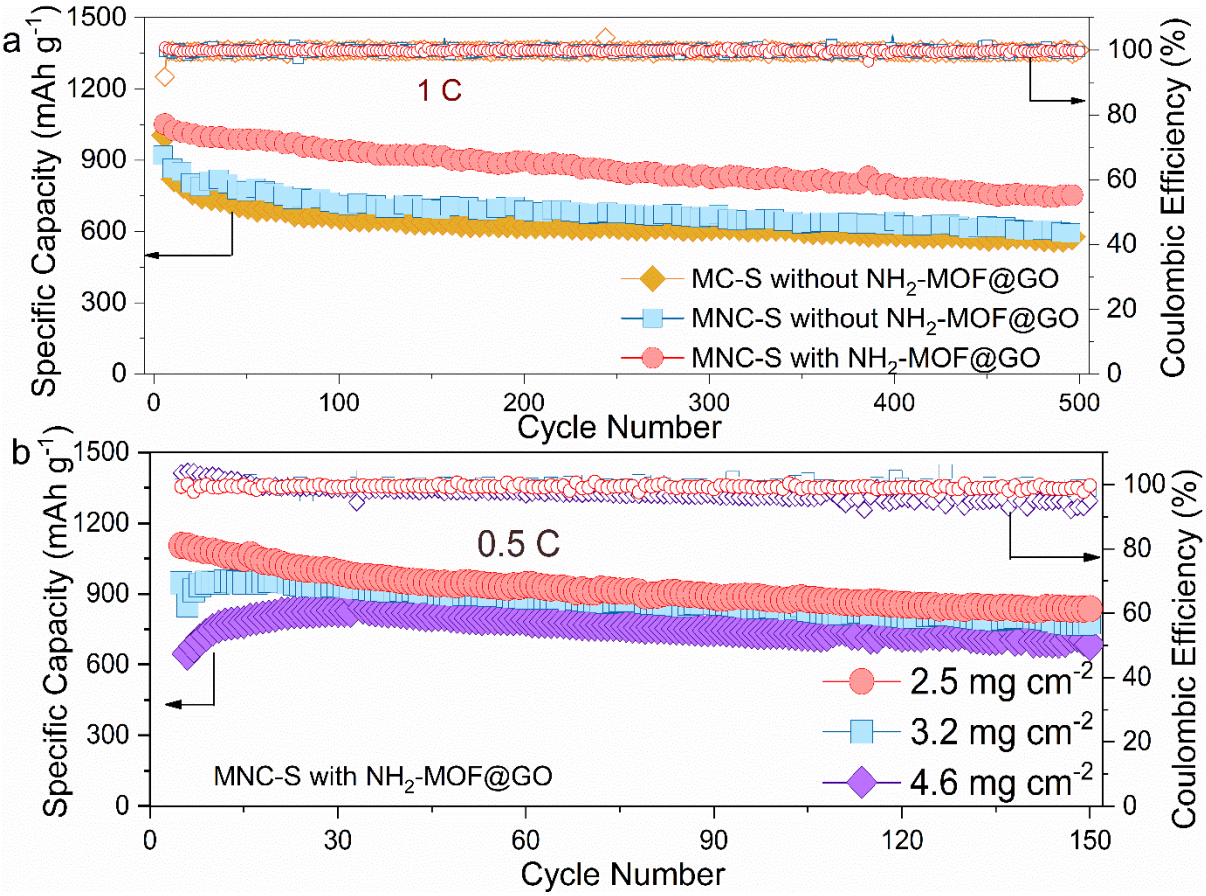

Figure 4.21 (a) long-term cycling performances of as-prepared cathodes at 1C rate with and without the NH_2-MOF@GO interlayer (b) Cycling performances of NMC-S cathode with NH_2-MOF@GO/PP/Li cells with high sulfur loadings at 0.5C rate.

Even when the Li-S cell is resting, the elemental sulfur can steadily converted into soluble polysulfide. Henceforth, polysulfide shutting, and consequent capacity decay could happen even

under the static condition. Thereafter, is it important for a viable Li-S system to be efficient enough to avert such 'self-discharge' issues. To investigate the self-discharge behavior of the Li-S cells with the PP/NH_2-MOF@GO and PP separators, NMC-S cathodes with different separators were first discharged-charged for 10 cycles at 0.3C rate and then the batteries were rested for 7 days.

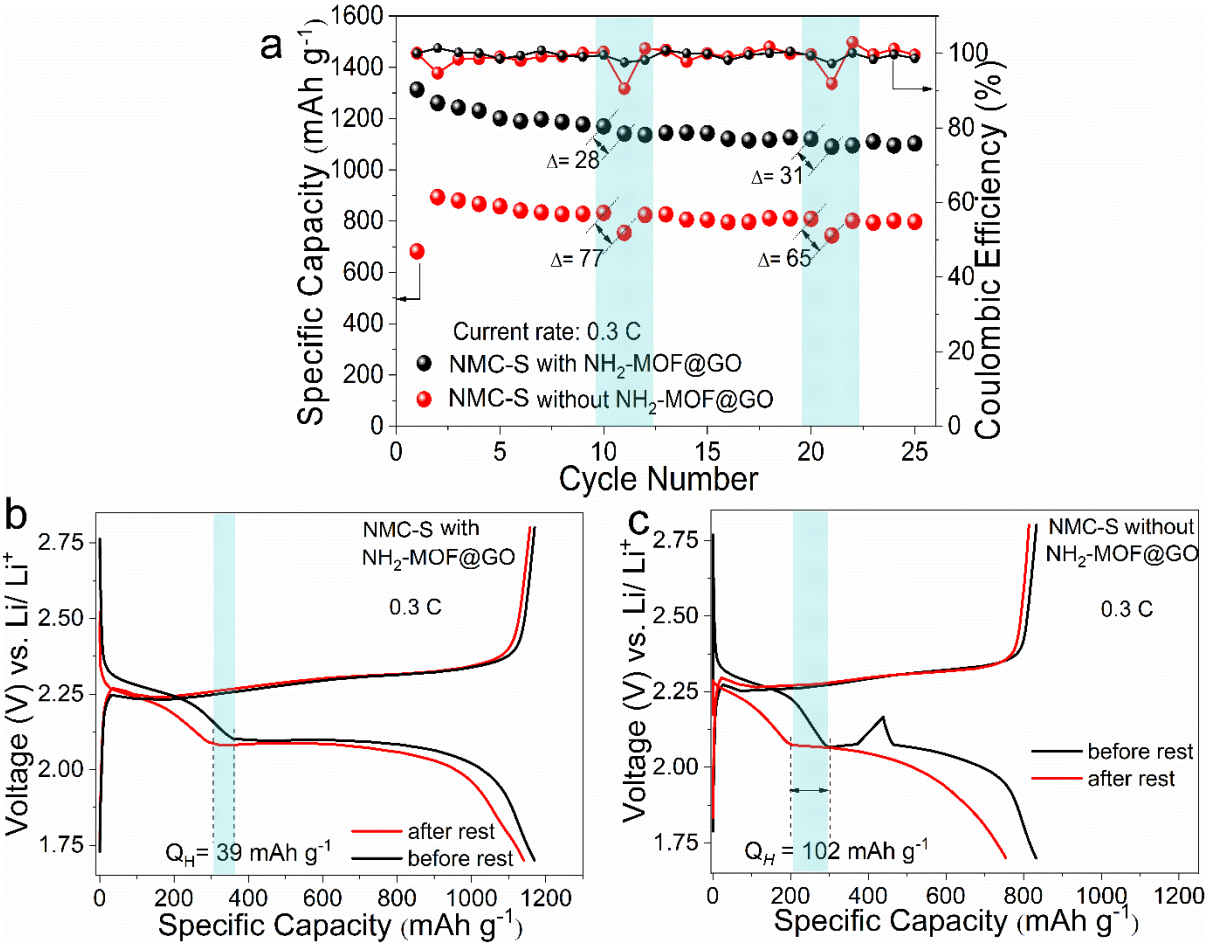

Figure 4.22 (a) Cycling performances, (b) and (c) discharge/charge profiles of Li-S batteries with and without the NH_2-MOF@GO interlayer at 0.3C rate before/after resting, respectively.

After 7 days of rest, the whole process was repeated. Before/after both the resting periods, the irreversible capacity loss for the Li-S cell with NH_2-MOF@GO interlayer was noticed to be much lower than that of the cell with the PP separator (**Figure 4.22a**). More importantly, the upper plateau discharge capacity (Q_H), which is attributed to the formation and subsequent diffusion of

polysulfides, has reduced significantly for the cell with PP ($\Delta Q_H \approx 102$ mAhg^{-1}) than the cell with NH_2-MOF@GO ($\Delta Q_H \approx 39$ mAhg^{-1}) interlayer, indicating severe self-discharge in the PP-based cell when it is irrelevant for NH_2-MOF@GO based cell (**Figure 4.22c**). Besides, a sudden drop in Coulombic efficiency and a large increase in voltage hysteresis were also noticed for the PP-based cell before/after rest. This remains almost unaltered for the cell with NH_2-MOF@GO interlayer. These observations further validate that the NH_2-MOF@GO interlayer has effectively prohibit the self-discharge and illustrate a stable, smooth electrochemical reaction.

In order to demonstrate that the NH_2-MOF@GO interlayer could inhibit the polysulfide shuttling, and simultaneous degradation of the anode, Li-S cells with different separators were disassembled after 200 consecutive cycles and the cycled Li anodes were characterized with FE-SEM. The surface of the cycled Li anode (**Figure 4.23a**) with the NH_2-MOF@GO interlayer is found to be as smooth without any significant Li dendrite growth. This is because the NH_2-MOF@GO separator can provide a homogeneous Li^+ flux at the interface of the separator and the Li anode. Besides, the sulfur content on the anode of the Li-S cell with the interlayer is as low as 1.27%, validating an efficient inhibition of polysulfide shuttling. In sharp contrast, a mosey lithium growth with distinctively high porosity was noticed for cycled Li anode in Li-S cells without the interlayer (**Figure 4.23b**). The sulfur content on such anode surface is as high as 10.58%, indicating uninterrupted polysulfide migration through the macropores of the PP separator. Moreover, such high surface area deposits continuously react with the electrolyte and the polysulfide, causing further degradation in electrochemical performance.

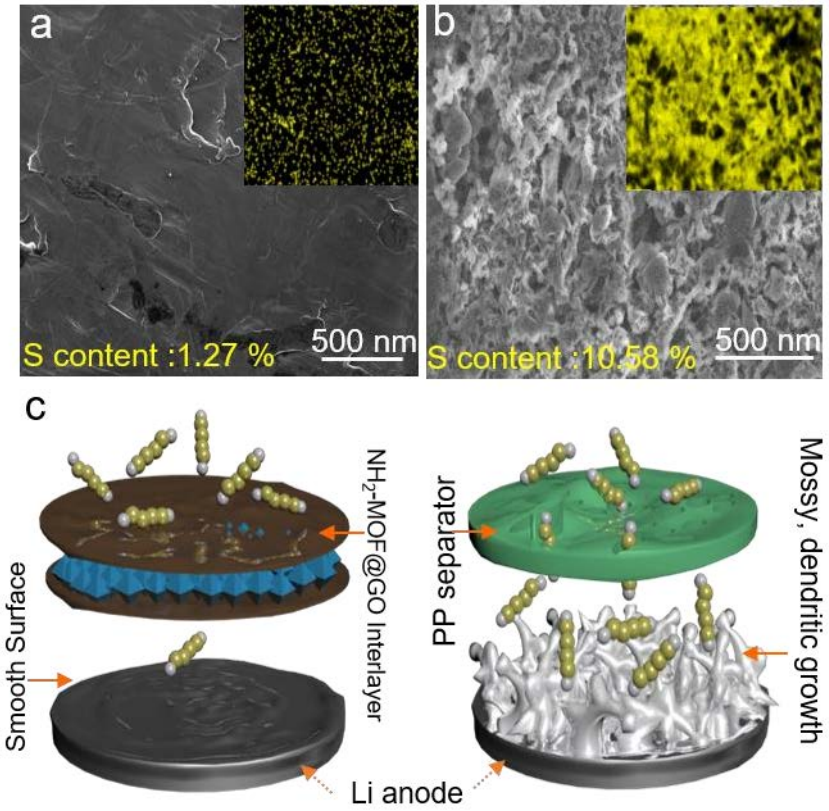

Figure 4.23 SEM images of Li-metal (a) with and (b) without NH_2-MOF@GO interlayer after 200 cycles. c) A comparison of polysulfide diffusion and Li-anode stability with and without the NH_2-MOF@GO interlayer.

The NH_2-MOF@GO interlayer was further analysed with FE-SEM, EDS, and FT-IR studies to investigate the microstructure and chemical compositional changes occurring during electrochemical testing. The FE-SEM images of the cycled membrane in **Figure 4.24a-b** shows the morphology has not changed significantly, where both the GO nanosheets and NH_2-MOF particles are still visible. Moreover, elemental maps (**Figure 4.24c**) reveal a strong sulfur signal on the surface of the separator, indicating effective polysulfide trapping. Meanwhile, an FTIR peak (**Figure 4.4b**) at around 937 cm^{-1} is attributed to Li-OH,[122] probably formed by the exposure of Li_2S to moisture during sample handling.

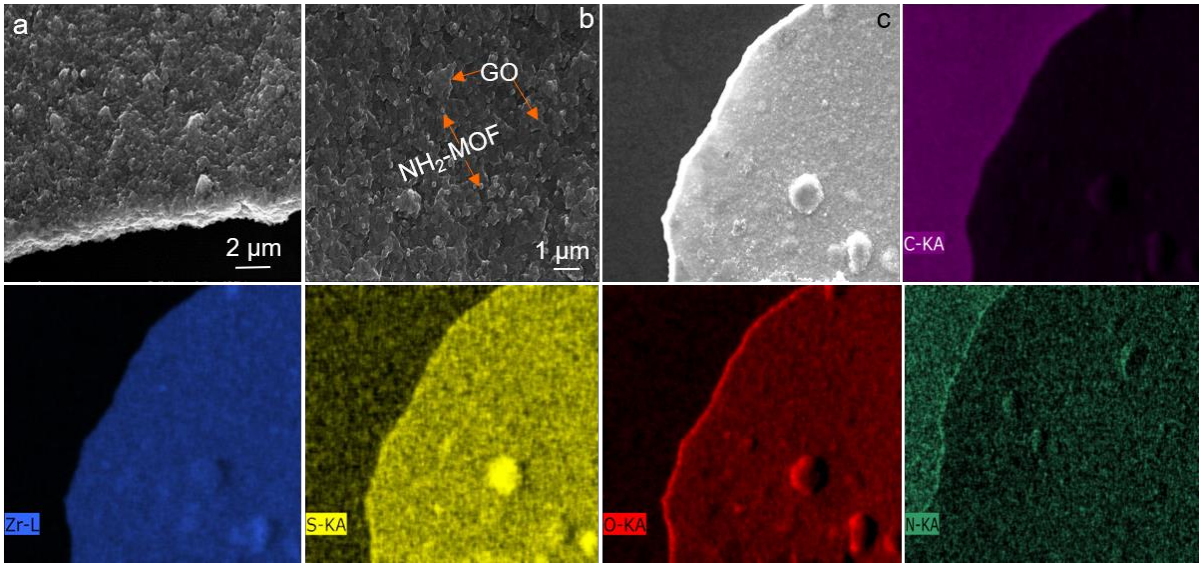

Figure 4.24 (a-b) FE-SEM images and (c) EDX elemental colour mapping of the NH_2-MOF@GO interlayer, confirming deposition of elemental sulfur after cycling in a Li-S cell.

4.4 Conclusion

In summary, we have synthesized a micro/mesoporous N-doped carbon from NH_2-MOF and utilized this porous structure as a sulfur-host for Li-S batteries. This highly porous structure not only provides enormous active sites for a substantial amount of active mass loading, but also endows a sophisticated electron-transfer pathway for ultrafine sulfur particles for better sulfur utilization, improved electrolytic penetration, and superior structural stability. Owing to gradual polysulfide diffusion, we have designed a NH_2-MOF@GO based interlayer for Li-S battery systems. The alternatively stacked NH_2-MOF nano-octahedra and GO nanosheets can function as a perfect ionic sieve restraining polysulfide by both physical and chemical ways, while having a negligible influence on the transfer of Li^+ ions across the separator. At the same time, uniform Li^+ flux generated through the separator-anode interface efficiently retarded the dendrite growth. The batteries with the NH_2-MOF@GO interlayer exhibited stable cycling performance including a high

reversible capacity of 1318 mAh g^{-1} at 0.2 C rate, 1155 mAh g^{-1} at 0.5 C rate with 80.3% capacity retention after 200 cycles.

Chapter 5

Rationally Designed Freestanding Bilayer Cathode with Polar Electrocatalyst for Efficient Polysulfides Conversion and High-performance Lithium-Sulfur Batteries

5.1 Introduction

Rechargeable lithium-sulfur (Li-S) batteries have received ever-increasing attention as next-generation energy storage devices for their high theoretical specific energy density, which is 3-5 times higher than traditional lithium-ion batteries (LIBs).[2] Unlike simple intercalation electrochemistry in LIBs, Li-S batteries involve a multielectron conversion reaction (S_8 + 16 Li ⟶ 8 Li_2S), resulting in a high theoretical capacity of (1672 mAh g^{-1}) and high energy density (2600 Wh g^{-1}) at an average potential of ~ 2.2 V (vs Li/Li^+). [80, 169] In addition, with the benefits of natural abundance, cost affordability and low toxicity, sulfur has a potential for large scale commercial application. Nonetheless, there are many challenges that needs to be addressed for developing efficient sulfur-based cathodes in the Li-S battery system. For instance, insulating sulfur and its reduced product (Li_2S / Li_2S_2) incudes limited active material utilization and sluggish reaction kinetics. The large volumetric expansion (≈ 80%) of sulfur during lithiation leads to the electrode pulverization and rapid capacity decay. More importantly, high solubility of lithium polysulfide intermediates (Li_2S_x, $4 \leq x \leq 8$) also results in an irreversible capacity loss and severe parasitic reactions with the lithium anode, which further diminishes the electrochemical performances of the Li-S battery.[170,171]

To address these issues as mentioned earlier, various strategies have been explored by many research groups. One such example is the use of suitable host that can offer physical confinement or chemical binding to the active materials. For instance, mesoporous carbon,[172] graphene,[173, 174] carbon nanotubes [175] can physically trap the lithium polysulfides. Nonetheless, weak interaction between nonpolar carbon and polar lithium polysulfides may not be enough to suppress lithium

polysulfides diffusion. On the contrary, polar materials such as, hetero-atom doped carbon,[176, 177] transition metal oxides/ nitrides/ sulfides [178- 186] could offer chemical interaction to the migrating lithium polysulfides and is more effective than simple physisorption. However, it is worth mentioning that whether physical or chemical adsorption, the kinetics of polysulfide conversion reactions via liquid (Li_2S_x, $4 \leq x \leq 8$)-solid (Li_2S_2/Li_2S) phase is very difficult to control just through these adsorption strategies. Such sluggish kinetics of lithium polysulfides conversion leads to the accumulation of lithium polysulfides into electrolyte, which results rapid diffusion of lithium polysulfides towards the Li-anode, further worsening the shuttle effect.[187] Other examples involve the insertion of an interlayer in between the cathode and the separator to reduce the lithium polysulfides migration.[188- 190] Nonetheless, introduction of an additional component not only increase the overall cell resistance of the whole system but also affects the diffusion of electroactive species through the interlayer.[191] Recently, metallic polar hosts or electrocatalysts have been used extensively as they can significantly improve the electrochemical performances of Li-S batteries by moderating the lithium polysulfides redox reaction kinetics. [192- 195]

Herein, we present a freestanding bilayer cathode to maximize the sulfur utilization and reduce the "shuttling effect" by controlling redox kinetics of lithium polysulfides conversion. The top layer of this novel cathode is composed of nickel and nitrogen co-doped graphene nanosheets (donated as NiNG) and the bottom part contains mixed phase NiNG and carbon nanofiber (CNF). Benefitting from the bilayer structure, this cathode can maximize the sulfur loading as high as 8 mg cm^{-2}. In addition, the electronegative nitrogen atoms can interact with the Li^+ through forming $N \cdot\cdot Li_2S_x$ structure, which can retard the lithium polysulfides diffusion. [196] More importantly, the metallic nickel nanoparticles grafted on nitrogen-doped graphene improve the electric conductivity of the cathode to guarantee high sulfur utilization and accelerate the kinetics of lithium

polysulfides conversion reaction. [197] Therefore, bilayer NiNG@CNF host is the ideal structure to maximize the sulfur loading and utilization, catalyse the polysulfide conversion, and minimize the shuttling phenomenon, showing outstanding electrochemical performance for both Li-S batteries.

5.2 Experimental Section

5.2.1 Synthesis of NiNG and NG:

$NiCl_2$, 6 H_2O (2 mL, 5 mL mg^{-1}) aqueous solution was added dropwise into the homogeneous graphene oxide (50 mL, 1 mg mL^{-1}) suspension under vigorous stirring and ultrasonicated for additional 30 min. The dispersion was then quickly frozen in liquid nitrogen and subjected to freeze-dry at -40 ˚C. The obtained $NiCl_2$@GO powder was then heated at a rate of 10 ˚C min^{-1} to 750 ˚C under a gas flow of 100 sccm Ar + 50 sccm NH_3 and kept at the same temperature for another 1 h to get NiNG nanosheets.

N-doped graphene (NG) was prepared in a similar way except that $NiCl_2$, 6 H_2O was not added.

5.2.2 Cathode fabrication:

First, NiNG and mixed NiNG / CNF suspensions were tip-sonicated separately in isopropanol (IPA) for 30 min to form stable dispersions. Both the suspensions were then vacuum-filtered alternatively on cellulose filter paper to obtain bilayer NiNG@CNF cathodes. The top layer of the NiNG@CNF cathode is composed of only NiNG nanosheets and the bottom layer consists mixed phhase NiNG and CNF. The weight ratio of NiNG to CNF was controlled at 1:3. The freestanding films were compressed and punched and into circular discs 1 cm in diameter.

5.2.3 Preparation of 1 M Li_2S_6 catholyte:

To prepare 1 M Li_2S_6 polysulfide catholyte, stoichiometric amounts of elemental sulfur (S_8) and anhydrous Li_2S (99.9%, Acros Organics) were mixed in electrolyte containing 1 M LiTFSI and 0.2 M $LiNO_3$ in dimethoxyethane (DME, Acros Organics): 1,3-dioxolane (DOL, Acros Organics)

(1:1, by volume). The mixture was then heated at 65 ˚C and stirred for 2 days in an argon filled glovebox. Finally, the dark red solution of Li_2S_6 polysulfide catholyte was obtained for experimental use.

5.2.4 Symmetric cell assembly and measurements:

For symmetric cell, two identical electrodes were used as working and counter electrode. 5 µL 1M Li_2S_6 catholyte was injected into both electrodes. In addition, 8 µL blank electrolyte was dropped onto separator. Then, cyclic voltammetry (CV) measurements were carried out using electrochemical workstation (VMP3, Bio-logic) between -1.4 to 1.4 V at scan rate of 5 mV s^{-1}.

5.2.5 Electrochemical cell assembly:

All the coin-type cells (C2032) were assembled in an argon-filled glovebox with lithium foil as anode. For cathode, appropriate amount of 1 M Li_2S_6 catholyte was injected into the bottom layer of the cathode. Polypropylene membrane (Celgard 2500) was used as a separator and inserted between cathode and anode. The electrolyte was 1 M LiTFSI dissolved in DME: DOL (1:1, by volume) with 0.2 M $LiNO_3$ additive, and the electrolyte/sulfur (E/S) was maintained at 12 for Li-S cells with sulfur loadings of 2 mg cm^{-2}. Low E/S ratio was also controlled at 7 for the Li-S cells with high sulfur loadings of 4, 6 and 8 mg cm^{-2}.

5.2.6 Materials characterizations and electrochemical analysis:

Scanning electron microscopy (SEM) and Energy dispersive X-ray spectroscopy (EDX) were carried out on a FEI Quanta 650 equipped with a Bruker EDX system. High-angle annular dark-field scanning transmission electron microscopy (HAADF-STEM) and high-resolution TEM (HR-TEM) were taken with FEI Titan G2 80-200 TEM/STEM with ChemiStem technology operating at 200 kV. XPS spectra were obtained with a Kratos Axis Ultra DLD spectrometer with monochromatic Al Kα radiation. A custom designed stainless-steel transfer chamber was used to

transfer the air- and moisture-sensitive samples under argon to the XPS instrument. Nitrogen adsorption and desorption isotherms were analysed with a Micromeritics Flex3 analyzer based on BET method. All electrochemical experiments were performed using coin-type C2032 cells. The assembled cells were placed to rest for 30 min before electrochemical testing. For regular Li-S cell, cycling voltammetry (CV) were recorded using an electrochemical workstation (VMP3, Bio-logic) between 1.7 – 2.8 V at various scan rates (0.12 – 2.0 mV s^{-1}). The galvanostatic discharge/ charge experiments were conducted on a cell cycler (Arbin Instruments) between 1.8 – 2.8 V at various cycling rates (0.2 C – 3 C). All capacities are based on mass of sulfur.

5.2.7 Calculation of Li^+ Diffusion Coefficient (D_{Li^+}):

The Li^+ diffusion coefficient (D_{Li} in cm^2 s^{-1}) can be calculated from CV curves at different scan rates using the Randles-Sevcik equation (Equation S1).

$$I_p = 2.69\times10^5\, n^{3/2} A\, D_{Li}^{1/2}\, v^{1/2}\, C_{Li} \qquad \text{(Equation S1)}$$

where I_p (A) stands for the peak current, n is the number of electrons involved in the reaction, A (cm^2) represents the surface area of the electrode, v (V s^{-1}) is the scan rate, and C_{Li} (mol L^{-1}) is the Li ion concentration.

5.3 Results and discussion

NiNG sample was synthesized by thermal treatment of a mixture of graphene oxide (GO) and Nickel (II) chloride ($NiCl_2$) under ammonia (NH_3) and argon (Ar) gas flow. In a typical synthesis, certain amount of $NiCl_2$ was added to a stable GO dispersion under vigorous stirring and ultrasonication. Subsequently, the composite was freeze-dried and annealed under ammonia flow to obtain the final product. During the annealing process, nitrogen atom was doped into graphene through the decomposition of ammonia gas. In the meantime, the residual $NiCl_2$ transforms to metallic nickel nanoparticles anchored onto graphene nanosheets. The co-existence of ultrafine

nickel nanoparticles and nitrogen-doped graphene presents the following advantages. First, the highly conductive NiNG can improve the sulfur utilization, which is one of the primary limitations in Li-S battery. Secondly, the sluggish reaction kinetics of polysulfide conversion and their subsequent migration has also been well addressed with such integrated NiNG structure. The synergistic effect between nickel nanoparticles and nitrogen dopants in NiNG provide a favourable microenvironment to restrain the lithium polysulfides. The polar nitrogen elements can offer better "fasten centres" for migrating lithium polysulfides, while the metallic nickel centres maybe serve as a catalyst to accelerate the conversion kinetics of lithium polysulfides (demonstrated in **Figure 5.1**).

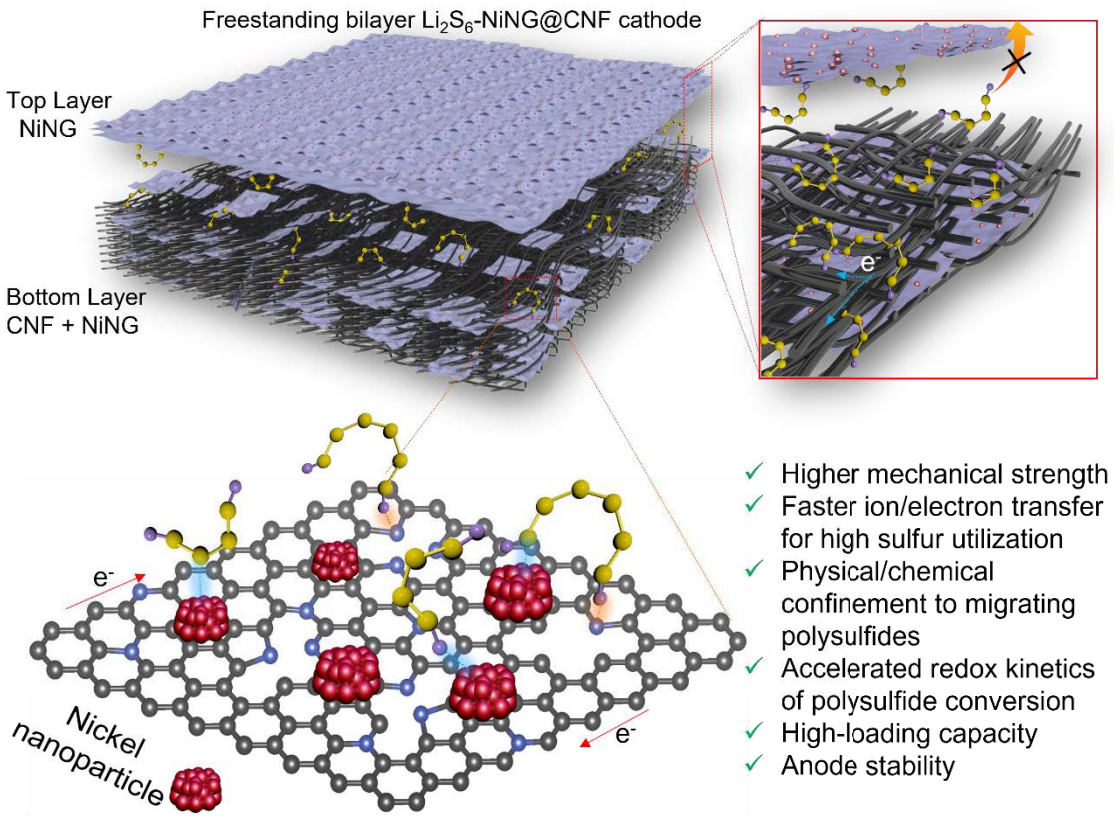

Figure 5.1 Schematic illustration showing structural benefits of bilayer Li_2S_6-NiNG@CNF cathode (upper panel) and improved redox reaction kinetics by NiNG electrocatalyst (lower panel).

The chemical composition and valence of the NiNG composite were detected by X-ray photoelectron spectroscopy (XPS). In the N 1s spectrum (**Figure 5.2a**), there are two peaks centred at 397.6 and 399.8 eV, corresponding to pyridinic and pyrrolic nitrogen, respectively. [198] In Ni 2p spectrum (**Figure 5.2b**), two characteristics peaks located at 854.4 and 871.8 eV, corresponding to Ni 2p3/2 and Ni 2p1/2, respectively, which can be assigned to metallic nickel element. [199]

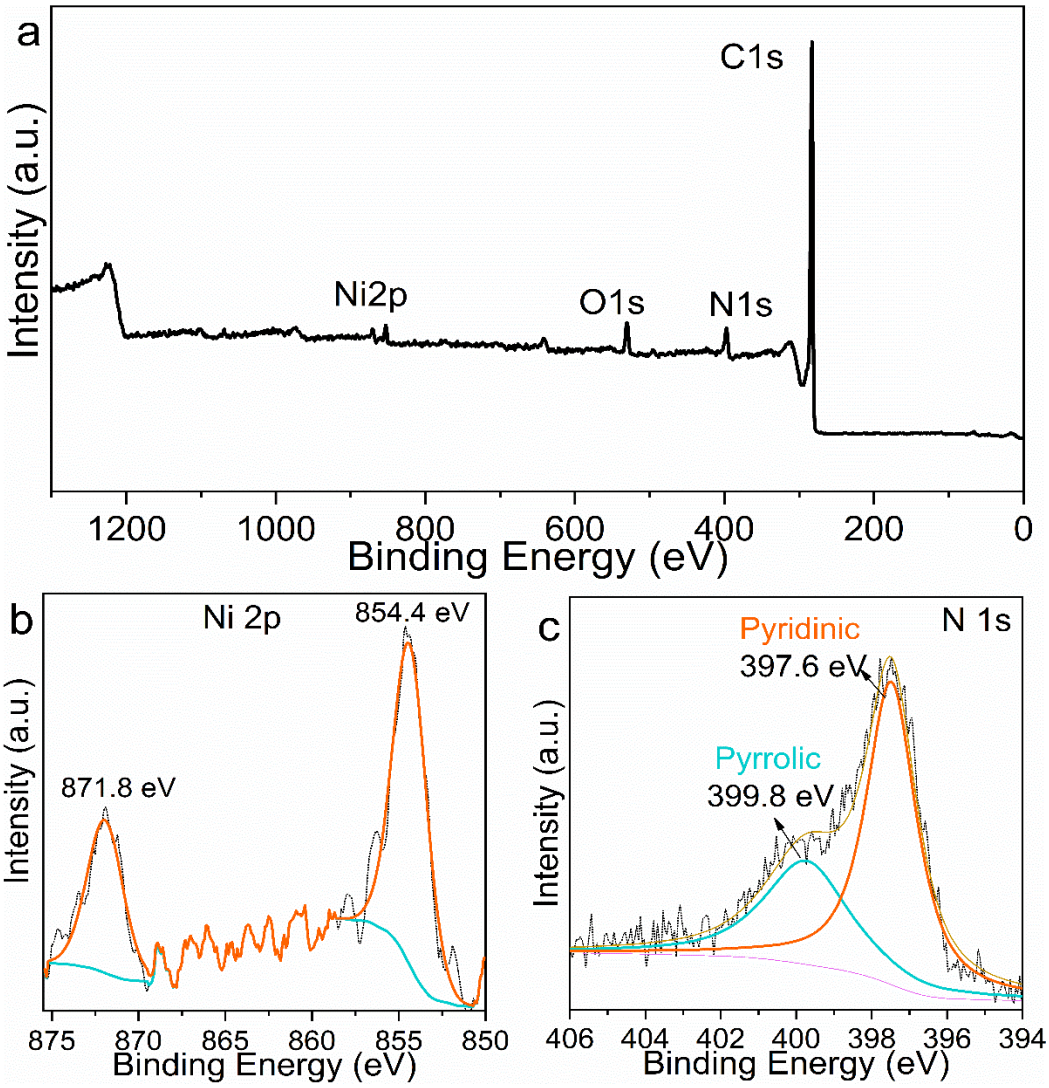

Figure 5.2 (a) XPS survey of NiNG sample. High-resolution XPS spectra (b) N 1s and (c) Ni 2p of pristine NiNG.

N_2 adsorption-desorption isotherm presented in **Figure 5.3a** shows that NiNG sample has a large specific surface area (Brunauer- Emmett- Teller) of 171 m^2 g^{-1}. Large specific surface area of a catalyst is highly desirable as the electrocatalytic reaction occurs only when the polysulfides are adsorbed on the catalyst surface.

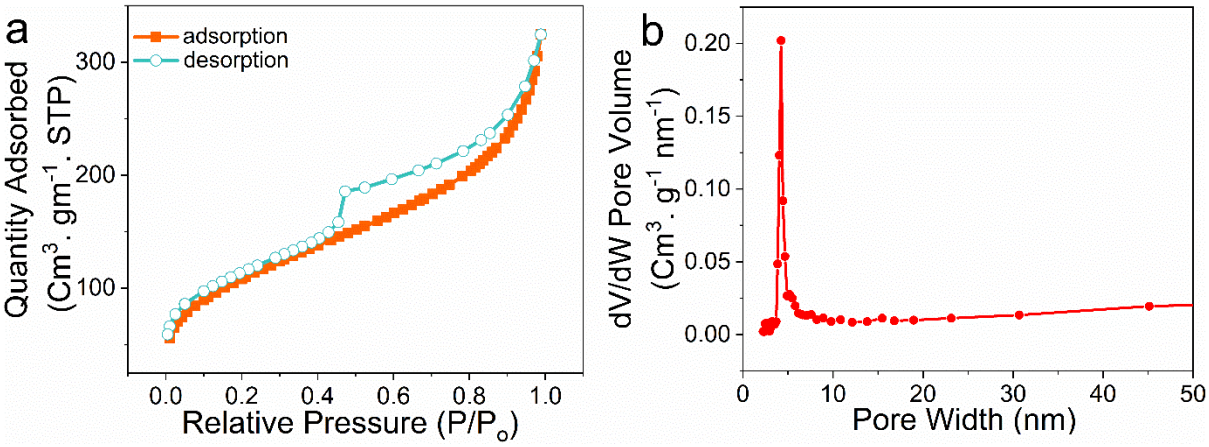

Figure 5.3 (a) N_2 adsorption-desorption curves and (b) BJH pore size distribution for Ni-NG nanosheets.

The detailed surface morphology of Ni-NG sample was studied by high-angle annular dark-field scanning transmission electron microscopy (HAADF-STEM) and high-resolution TEM (HR-TEM). **Figure 5.4a** displays HAADF-STEM of Ni-NG nanosheet, where the nickel nanoparticles (appeared as bright spots) uniformly dispersed on the graphene support are seen. HR-TEM image in **Figure 5.4b** reveals the nickel nanoparticle with a size of approximately 12 nm. The oxygen-containing functional groups on the GO sheets may serve as heterogeneous nucleation sites during the initial stages of the reaction, facilitating the formation of small nickel nanoparticles. HAADF-STEM image and EDX elemental colour mapping of NiNG nanosheet also confirm presence of nitrogen and nickel elements (**Figure 5.4c**). TEM image in **Figure 5.4d** shows the wrinkled surface

of NG nanosheets without any nickel particle. HAADF-STEM and elemental mapping of NG sample in **Figure 5.4d-e** demonstrates the successful doping of nitrogen.

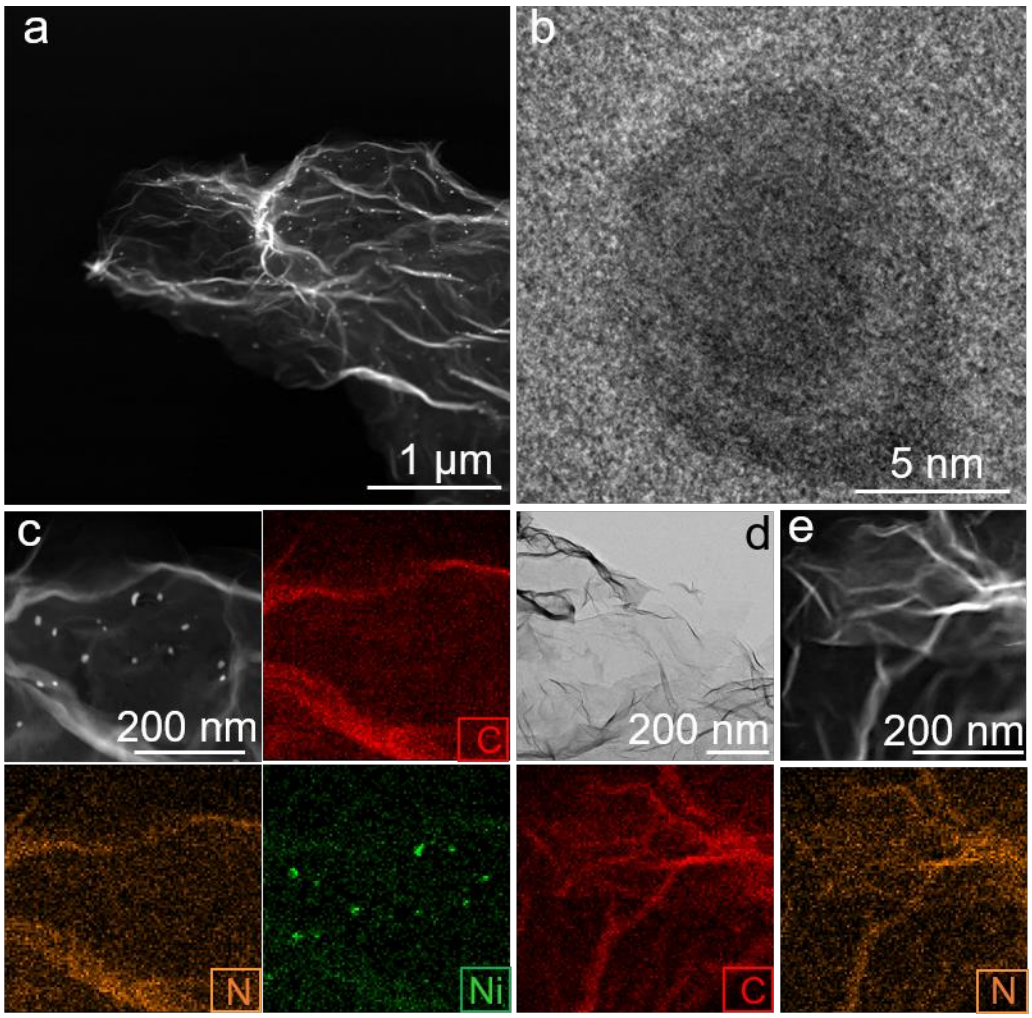

Figure 5.4 Detailed morphological characterizations of NiNG: (a) HAADF-STEM, (b) HR-TEM and (c) STEM image with corresponding elemental mappings of C, N and Ni. (d) TEM and (e) STEM images of NG sample with corresponding elemental mappings of C and N elements.

The as-synthesized NiNG composite was then combined with CNF via a two-step vacuum filtration method to fabricate bilayer NiNG@CNF cathode. In the first step, the bottom layer was prepared by ultrasonicating mixed phase NiNG/CNF in isopropanol and filtering. In the second step, a stable dispersion of NiNG in isopropanol was filtered through the CNF layer to obtain the

bilayer structure. After carefully drying, the freestanding cathode was compressed and cut into 10 mm circular disk. Such a rationally designed cathode imparts multiple benefits to enhance performance of the Li-S battery. First, the entangled CNF network enhances the overall mechanical strength of the cathode and buffer the volume change in active materials during electrochemical reactions. It also provides a physical support to the NiNG top layer. Secondly, conductive CNF/NiNG matrix (bottom part) provides fast ion/electron transfer pathways, benefitting efficient electrochemical utilization of active material and its high-loading capability. Meanwhile, the NiNG topping which also function as an interlayer, not only immobilize the lithium polysulfides in both physical and chemical ways but also trigger the rapid reduction/oxidation of adsorbed lithium polysulfides before they migrate to anode compartment. Beside these unique structural and catalytic benefits, this freestanding cathode excludes the use of toxic solvents (such as N-methyl pyrrolidone), inactive binder, conductive additives, and current collectors. The digital photographs of free-standing NiNG @CNF cathodes with a diameter 10 mm are shown in **Figure 5.5a**. Colour difference of the layer clearly indicate the bilayer structure of the cathode. A cross-sectional scanning electron microscopy (SEM) image showing the stacking morphology of NiNG@CNF cathode is presented in **Figure 5.5b**. The cross-sectional image reveals, a thin layer of NiNG nanosheets with the thickness of ~ 3 μm is overlaid on the NiNG/CNF support. The thickness of the support layer was carefully controlled around ~ 30 μm. Individual SEM images of top and bottom components are displayed in **Figure 5.5c** and **Figure 5.5d**, respectively. Graphene like morphology revealed in **Figure 5.5c** confirms only NiNG nanosheets are present at the top layer while SEM image of the bottom layer (**Figure 5.5d**) ensures the co-existence of both NiNG nanosheets and CNF.

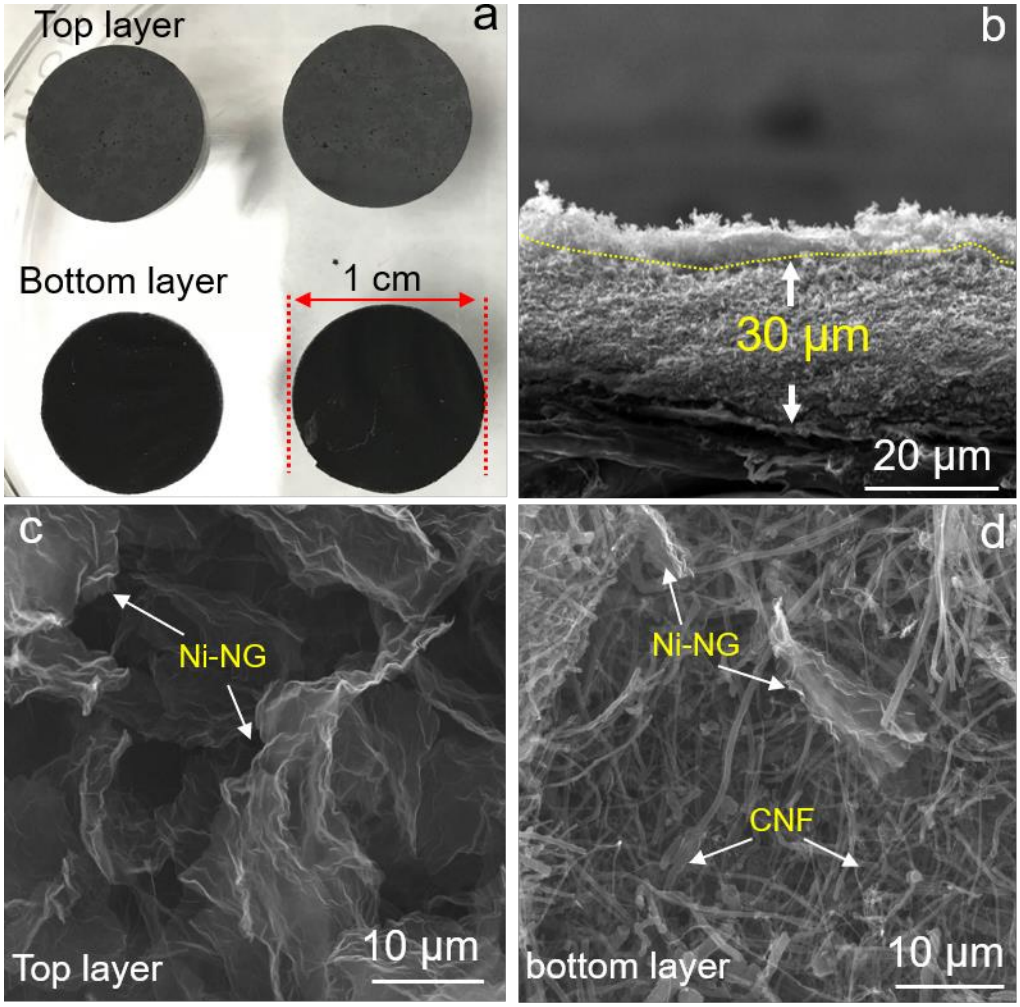

Figure 5.5 (a) photographs of NiNG@CNF cathode, SEM images displaying (b) cross-section, (c) top layer (NiNG layer) and (d) bottom layer (NiNG/CNF layer) of bilayer NiNG@CNF cathode.

To explore the catalytic behaviour of nickel and nitrogen centres of NiNG, certain amount of NiNG sample was dispersed and stirred in Li_2S / ethanol solution for overnight. The NiNG sample was then collected by filtration and repeatedly washed with anhydrous ethanol to remove the excess Li_2S. The obtained product was then dried thoroughly and subjected to XPS analysis. The whole process was carefully carried out inside an Ar-filled glovebox. As demonstrated in **Figure 5.6a**, N 1s spectrum shows an apparent upshift by +1.1 eV after Li_2S is adsorbed on Ni-NG owing to the s-p orbital interaction between Li and N. Similarly, the Li 1s spectrum in **Figure 5.6c**, can

be deconvoluted into two peaks. Peak fitting around 55.4 eV is attributed to Li-N bond, also confirming Li and N atom interaction. [200]

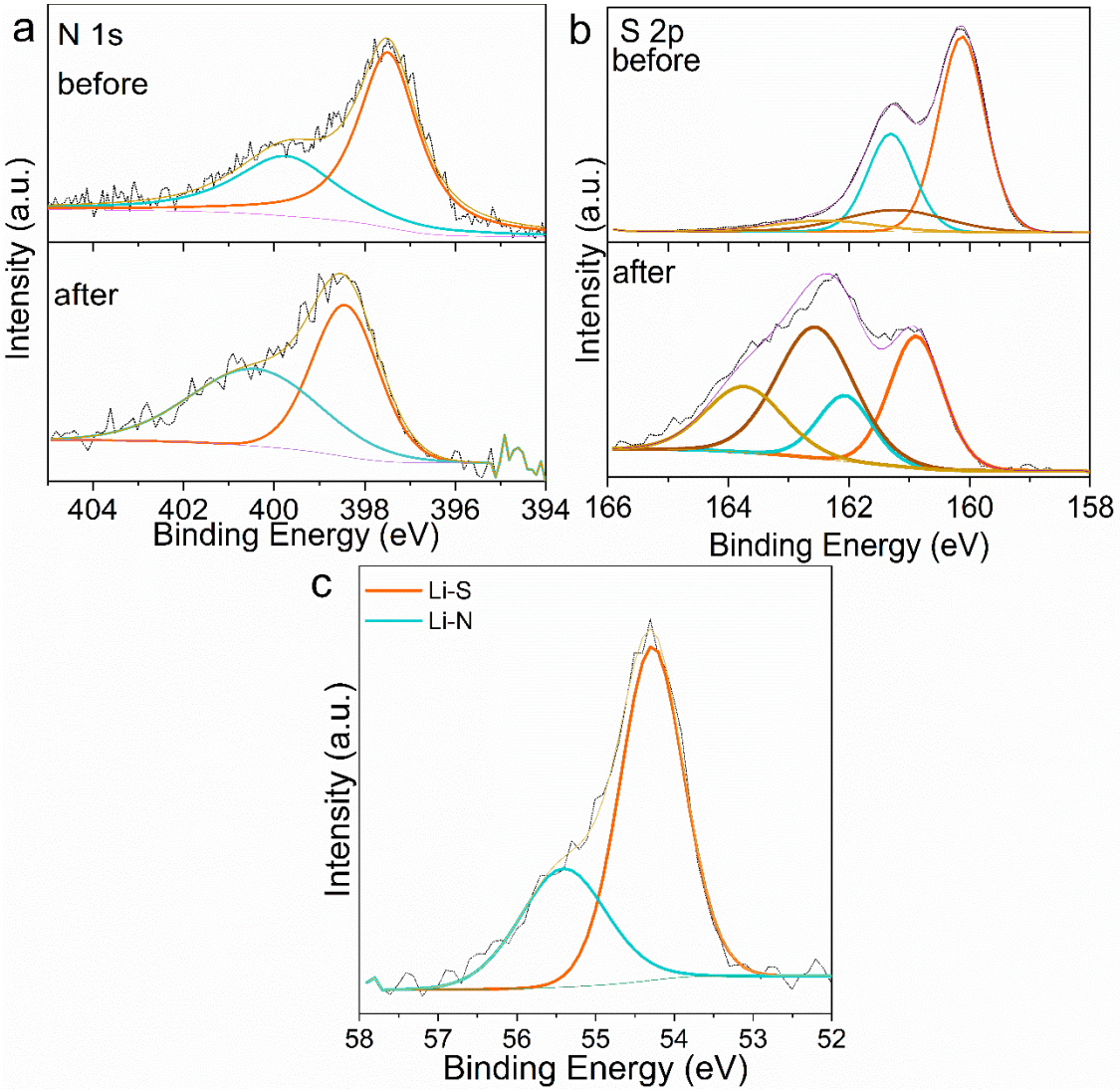

Figure 5.6 High resolution XPS spectra (a) N 1s, (b) S 2p and (c) Li 1s of NiNG sample before and after the adsorption towards Li_2S.

S2p region (**Figure 5.6b)**, peaks at 160.1 and 161.3 eV can be ascribed to S $2p_{3/2}$ and S $2p_{1/2}$ of commercial Li_2S powder. After treating with NiNG, the S $2p_{3/2}$ peak of Li_2S is shifted to a higher binding energy by + 0.8 eV, which is attributed to the interaction with metallic nickel element of NiNG.

To evaluate the electrocatalytic effect of as-prepared cathodes on the performance of Li-S batteries, coin cells with Li_2S_6-NiNG@CNF, Li_2S_6-NG@CNF and Li_2S_6-CNF cathodes were assembled. Appropriate amount of 1M Li_2S_6 catholyte was injected into the bottom part of our bilayer cathode and tested against lithium anode. The impact of NiNG catalyst on the electrochemical reaction is investigated by the cyclic voltammetry (CV) at a scan rate of 0.2 mV s^{-1}. As shown in **Figure 5.7**, Li_2S_6-NiNG@CNF, Li_2S_6-NG@CNF and Li_2S_6-CNF electrodes show two cathodic peaks and one anodic peak, corresponding to two-step reduction of sulfur to Li_2S_2 / Li_2S and reverse oxidation reaction of Li_2S_2 / Li_2S to sulfur.

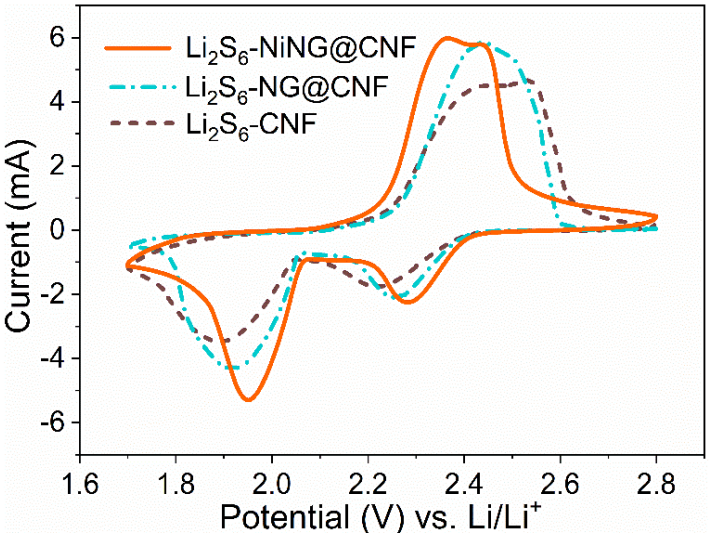

Figure 5.7 CV profiles of Li_2S_6-NiNG@CNF, Li_2S_6-NG@CNF, and Li_2S_6-CNF cathodes at a scan rate of 0.2 mV s^{-1}.

It is noteworthy that the cell employing Li_2S_6-NiNG@CNF cell demonstrates higher peak current and low potential difference (0.45 V in Li_2S_6-NiNG@CNF vs. 0.53 V in Li_2S_6-NG@CNF vs. 0.60 V in Li_2S_6-CNF) between cathodic and anodic peaks as compared to the cells utilizing Li_2S_6-NG@CNF and Li_2S_6-CNF electrodes. This suggests accelerated redox kinetics of polysulfide conversion in Li-S cell with Li_2S_6-NiNG@CNF cathode due to the catalytic effect of NiNG.

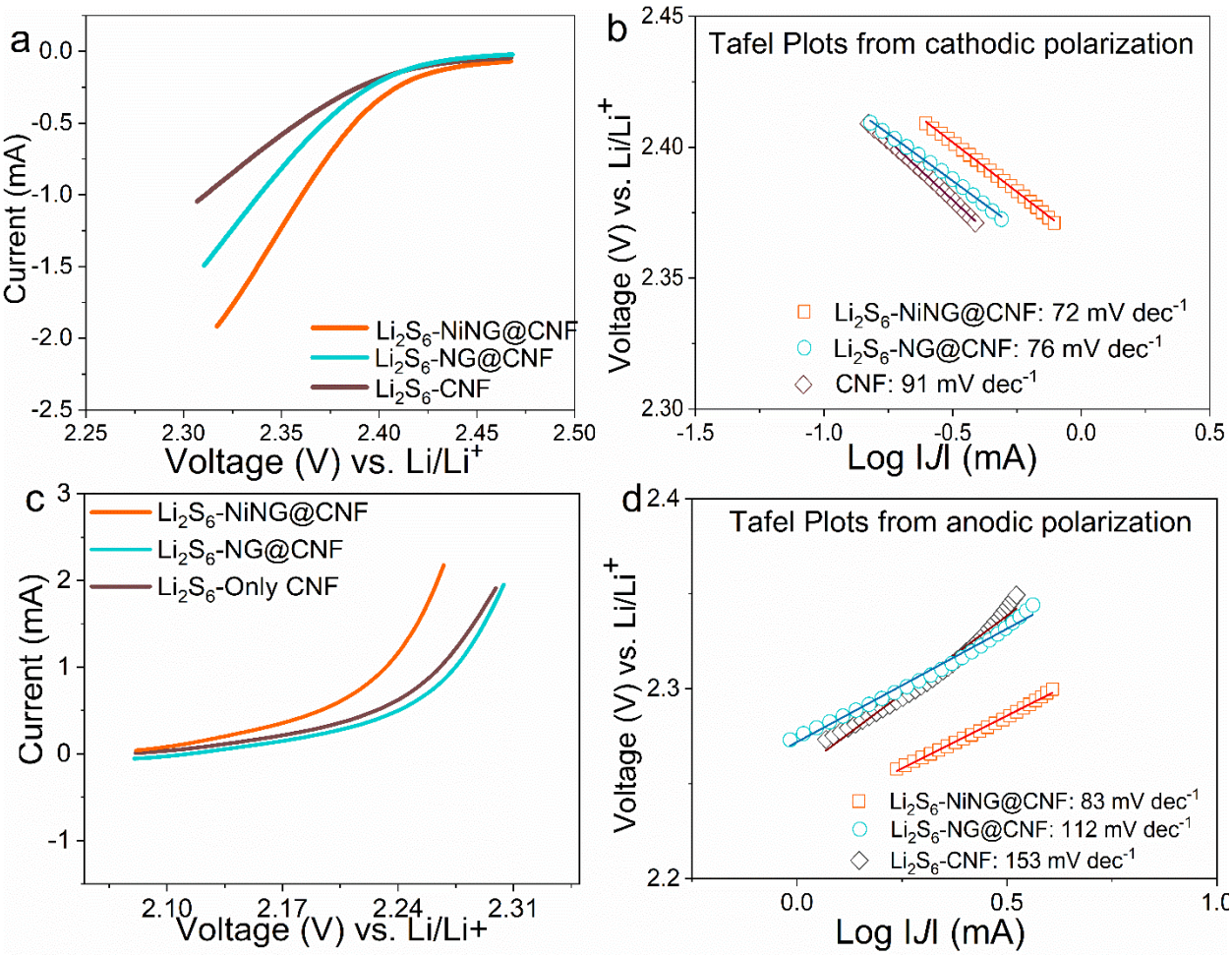

Figure 5.8 Comparison of (a) cathodic polarization curves and (b) corresponding Tafel plots. (c) anodic polarization curves and (d) corresponding Tafel plots.

Such trends are more evident in the comparison of their polarization curves. Tafel plots were obtained from cathodic polarization curve (**Figure 5.8a**) and anodic polarization curve (**Figure 5.8c**) to illustrate the catalytic effects on the charge-transfer kinetics during polysulfide conversion reactions. As shown in **Figure 5.8b** and **5.8d**, Li_2S_6-NiNG@CNF cathode demonstrates Tafel slope of 72 and 83 mV dec^{-1} in the reduction and oxidation processes, respectively, much smaller than those of Li_2S_6-NG@CNF and Li_2S_6-CNF cathodes. This clearly manifests the accelerated polysulfide conversion kinetics in presence of NiNG catalyst. The electrocatalytic behaviour of NiNG is also investigated by constructing symmetric cells containing two identical electrodes with

Li_2S_6 catholyte, and cyclic voltammetry (CV) was conducted between -1.4 to 1.4 V at 5 mV s^{-1}. The signals appeared in the CV scan are mainly attributed to the redox reactions of Li_2S_6 with a minimal contribution from capacitive current, as evident by the negligible current in Li_2S_6-free symmetric cell. As shown in **Figure 5.9**, the Li_2S_6-Ni-NG@CNF electrode displays four intense peaks at -0.606, 0.227, 0.621 and -0.270 V. As mentioned earlier, all these peaks are arising from the reduction / oxidation reactions of Li_2S_6 / S species. In sharp contrast, the redox peaks obtained in NG catalyst and CNF are broad and low in current density with significant voltage hysteresis.

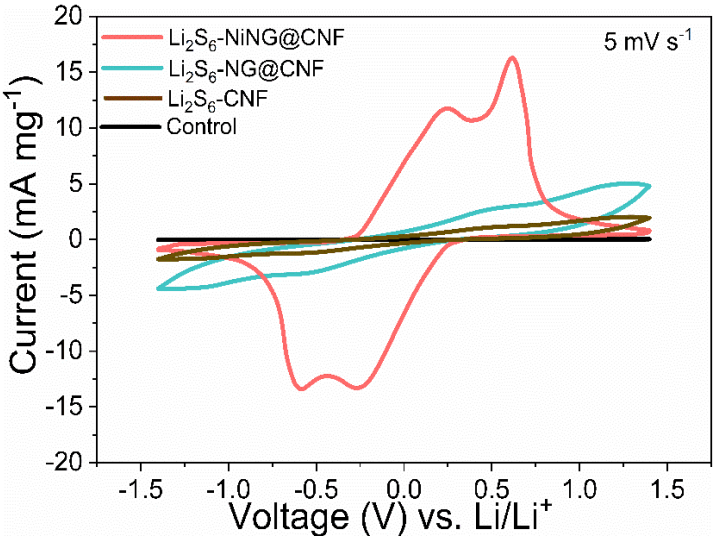

Figure 5.9 CV curves of symmetric cells at a scan rate of 5 mV s^{-1}.

This observation indicates that the catalytic property of NiNG is superior to NG and CNF over lithium polysulfides transformation reactions. To elucidate the internal resistance of as-prepared electrodes, *in-situ* electrochemical impedance spectroscopy (EIS) was performed for the second cycle. The cells were galvanostatically discharged and charged at a rate of 0.1C, and simultaneously internal resistance of the cells were recorded by EIS at different cut-off potential. As shown in **Figure 5.10**, the charge transfer resistance (R_{ct}) of Li_2S_6-NiNG@CNF electrode always remain lower than Li_2S_6-NG@CNF and Li_2S_6-CNF electrodes, indicating that the NiNG

nanosheets enable much faster charge transfer kinetics, which significantly enhances the redox kinetics of lithium polysulfides. It is worth to mention that, when the Li_2S_6-CNF electrode were discharged from its complete charged state to 2.1 V (vs. Li/Li^+), ohmic resistance (R_Ω) increased by a value of 8 Ω. This is attributed to severe migration of polysulfides from the Li_2S_6-CNF cathode and dissolution into electrolytes, resulting increase of the viscosity of the electrolyte medium. In contrast, the R_Ω value of Li_2S_6-NiNG@CNF cathodes remain unchanged during the analysis, demonstrating minimal dissolution of lithium polysulfides. During both the discharge/charge process, the Warburg diffusion of Li_2S_6-NiNG@CNF cathode is steeper than Li_2S_6-NG@CNF cathode, particularly than Li_2S_6-CNF electrode, indicating improved Li^+ ions conduction (**Figure 5.11**). Furthermore, Li^+ diffusion coefficient (D_{Li^+}) at the anodic (a) and cathodic (b, c) peaks of the Li-S cell with NiNG are, respectively, 2.1×10^{-6}, 3.6×10^{-7}, and 8.1×10^{-7} cm^2 s^{-1} (**Table 5.1**), which are much higher than the Li-S cell without NiNG layer. Such enhanced Li^+ ion diffusion coefficient of Li_2S_6-NiNG@CNF cathode manifests a favourable electrochemical environment and accelerated redox kinetics contributed by the catalytic effect of NiNG during discharge/charge process. To demonstrate the role of NiNG top layer in prevention of self-discharge, cells with and without NiNG top layer were kept under static condition while monitoring the open circuit voltage (OCV).

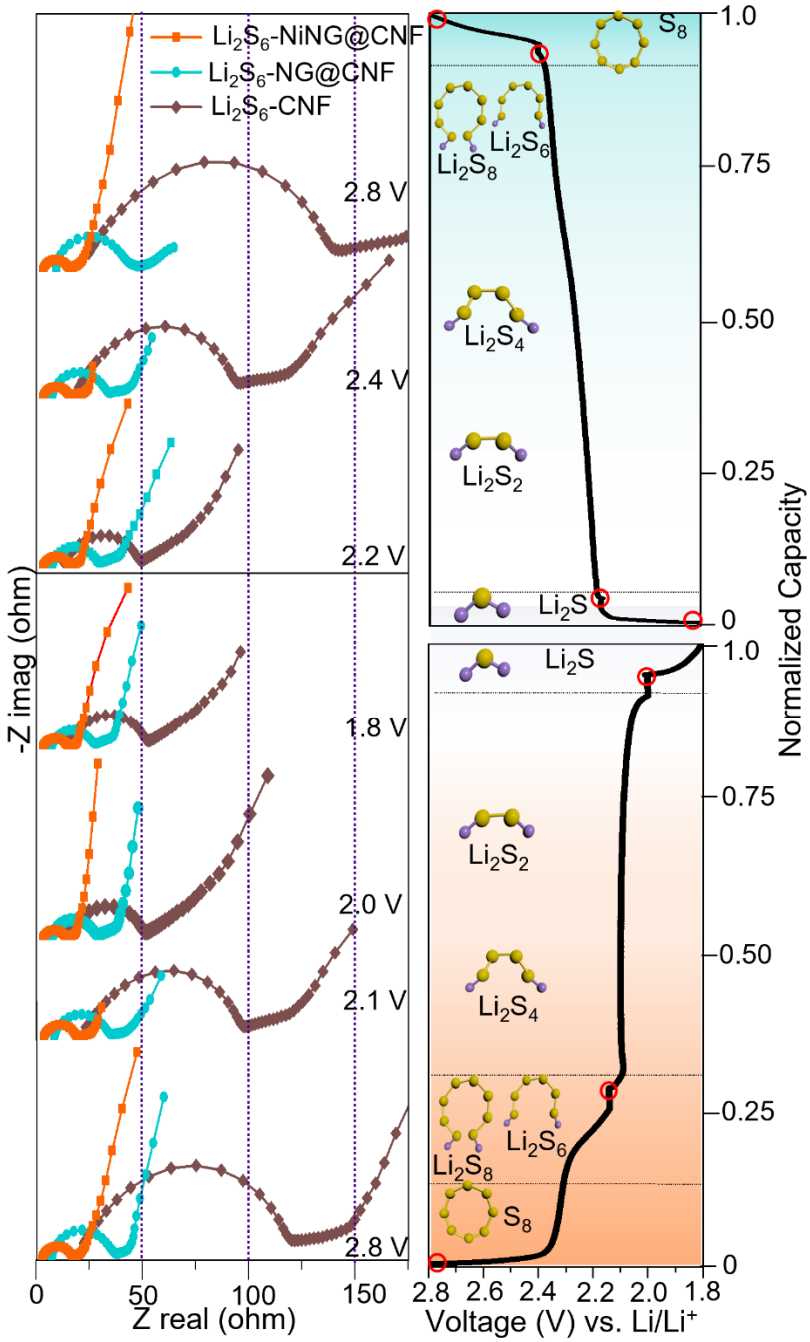

Figure 5.10 The Nyquist plots of as-prepared electrodes derived from in-situ EIS from 2nd cycle. The discharge/charge process was carried out at 0.1 C rate.

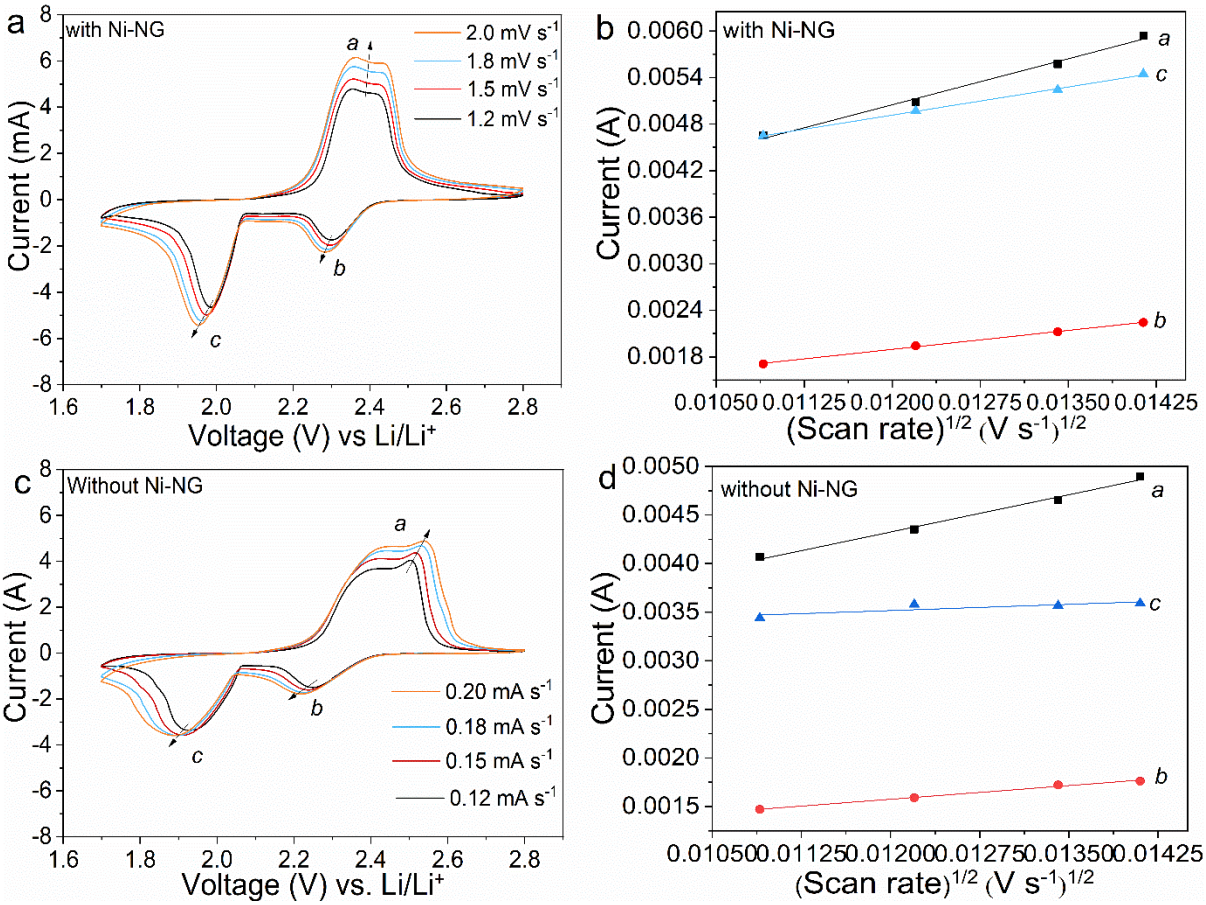

Figure 5.11 CVs at different scan rates and corresponding linear fits of the peak currents of Li_2S_6 based Li-S batteries (a, b) with and (c, d) without NiNG electrocatalyst.

Table 5.1 Summery of Li^+-diffusion coefficient (D_{Li^+}) values of as-prepared Li-S cathodes with and without Ni-NG electrocatalyst.

	D_{Li^+} (*a*)	D_{Li^+} (*b*)	D_{Li^+} (*c*)
Without NiNG	9.02×10^{-7}	1.2×10^{-7}	2.4×10^{-8}
With NiNG	2.1×10^{-6}	3.6×10^{-7}	8.1×10^{-7}

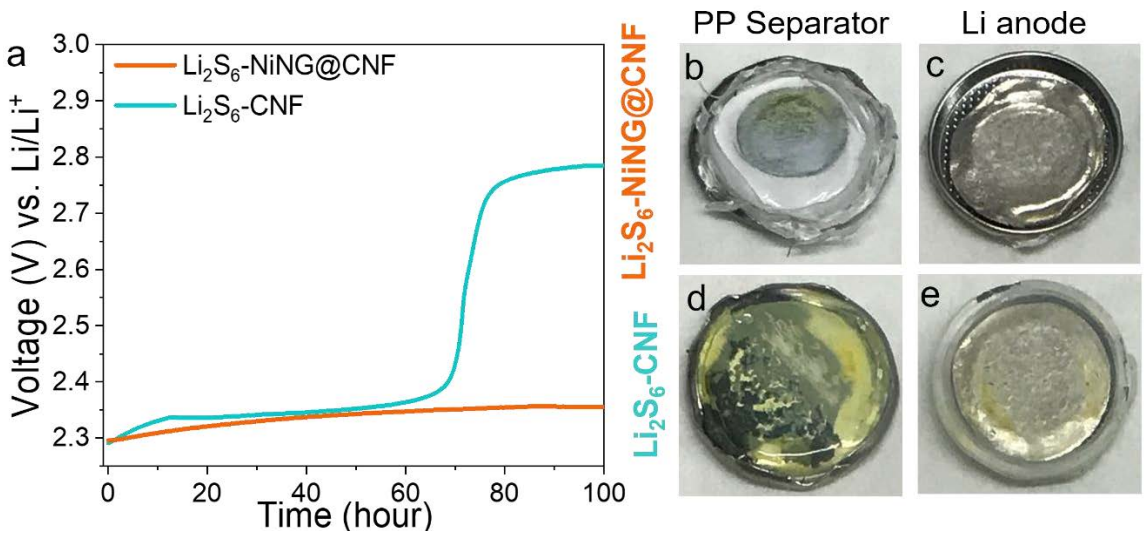

Figure 5.12 (a) Comparison of changes in open circuit potential (OCV) of Li-S cells with Li_2S_6-NiNG@CNF and Li_2S_6-CNF electrodes before and after 100 h of rest at room temperature. Digital photographs of PP separator and Li-anodes after 100 h rest (b, c) Li_2S_6-NiNG@CNF and (d, e) Li_2S_6-CNF electrodes.

As shown in **Figure 5.12a**, OCV of the Li-S cell without NiNG topping sharply increased to 2.68 V (vs. Li/Li^+) just after 60 h of resting time. This can be attributed to the uncontrolled dissolution of polysulfides from the Li_2S_6-CNF cathode, therefore, the overall potential of the cell is mainly contributed by the Li-anode. On the other hand, OCV in Li_2S_6-NiNG@CNF cell remained constant throughout the analysis, indicating very minimal polysulfides dissolution from the bilayer Li_2S_6-NiNG@CNF cathode. This is further confirmed by disassembling the Li-S cells after their resting period. As displayed in **Figure 5.12b-d**, the deep yellow polysulfides can be easily discerned on the surface of the separator paired with Li_2S_6-CNF cathode, indicating severe polysulfide dissolution into the electrolytes. In contrast, the separator paired with bilayer Li_2S_6-NiNG@CNF cathode is much cleaner, only a small amount of polysulfide could be visible, suggesting the polysulfide dissolution and self-discharge were effectively suppressed. **Figure 5.13a** demonstrates

the galvanostatic discharge-charge curves of Li_2S_6-NiNG@CNF, Li_2S_6-NG@CNF, and Li_2S_6-CNF electrodes at 0.2 C.

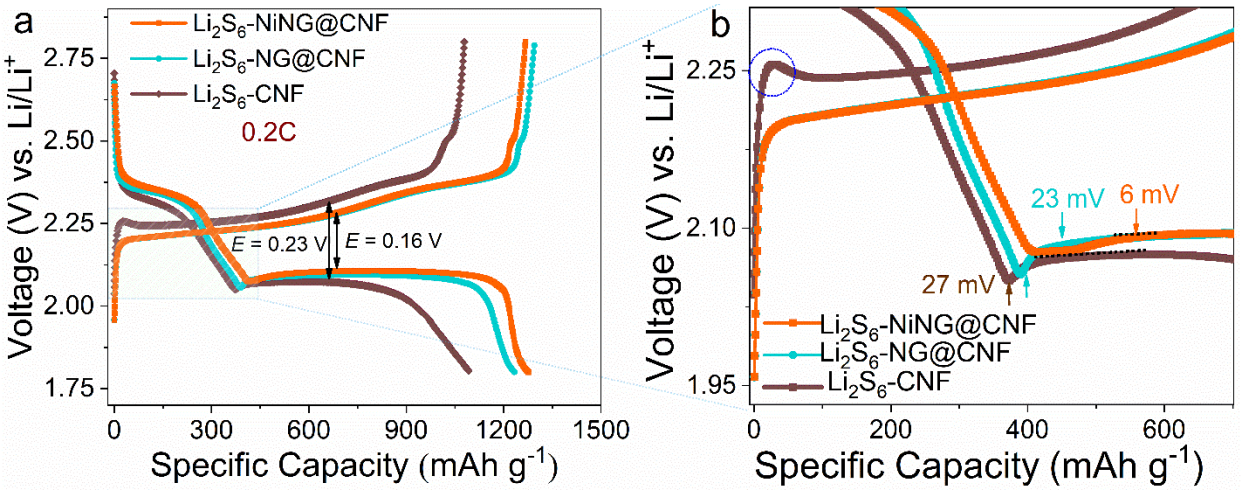

Figure 5.13 (a, b) Galvanostatic discharge/charge curves of Li_2S_6-NiNG@CNF, Li_2S_6-NG@CNF and Li_2S_6-CNF electrodes at 0.2 C.

We found the Li_2S_6-CNF electrode shows large voltage hysteresis of 270 mV between discharge and charge plateaus, which is 110 mV higher than the same for Li_2S_6-NiNG@CNF and Li_2S_6-NG@CNF electrodes (**Figure 5.13b**). This observation clearly indicates slow redox kinetics of sulfur species on less conductive CNF surfaces. In addition, a voltage peak appeared at ≈ 2.25 V (marked by blue circle in **Figure 5.13b**) in the charge profile also supports the low conductivity of Li_2S_6-CNF electrode. During charging, such voltage peak could appear as a result of insufficient electrical conductivity of the cathode, when some overpotential is required to drive the oxidation of insulating Li_2S_2/Li_2S to liquid lithium polysulfides. [201] On contrary, no voltage peak was observed for Li_2S_6-NiNG@CNF and Li_2S_6-NG@CNF electrode at that potential of charging, indicating smooth redox reactions on highly conductive NiNG and NG matrixes. However, we also notice that the overpotential shown by Li_2S_6-NiNG@CNF electrode at Li_2S nucleation point is as low as 6 mV compared to 23 and 27 mV for Li_2S_6-NG@CNF and Li_2S_6-CNF electrodes,

respectively (**Figure 5.13b**). This result establishes the enhance Li_2S nucleation kinetics enabled by NiNG network. Cycling stability is an important indicator to evaluate the property of Li-S batteries. When cycled at 0.2 C, the Li_2S_6-NiNG@CNF cathode produced a high reversible discharge capacity of 1272 mAh g^{-1} compared to 1253 mAh g^{-1} of Li_2S_6-NG@CNF cathode and obtained higher capacity retention rate (~89.4 % in Li_2S_6-NiNG@CNF vs. ~53 % in Li_2S_6-NG@CNF) after 100 consecutive cycles (**Figure 5.14**). Both the composite cathodes demonstrated improved electrochemical performances than the control Li_2S_6-CNF cathode, which yielded a discharge capacity of 983 mAh g^{-1} under same current density and retained only 105 mAh g^{-1} (11 % capacity retention) after 90 cycles. The severe capacity fading in Li_2S_6-CNF cathodes can be ascribed to the uncontrolled dissolution and migration of lithium polysulfides. To gain an insight of electrochemical process, the capacity-potential profiles of the as-prepared cathodes at 0.2C are analysed. All Li-S cells based on the Li_2S_6-NiNG@CNF, Li_2S_6-NG@CNF and Li_2S_6-CNF (**Figure 5.15 a-c**) exhibit the typical two-plateau discharge curves through the prolonged cycling.

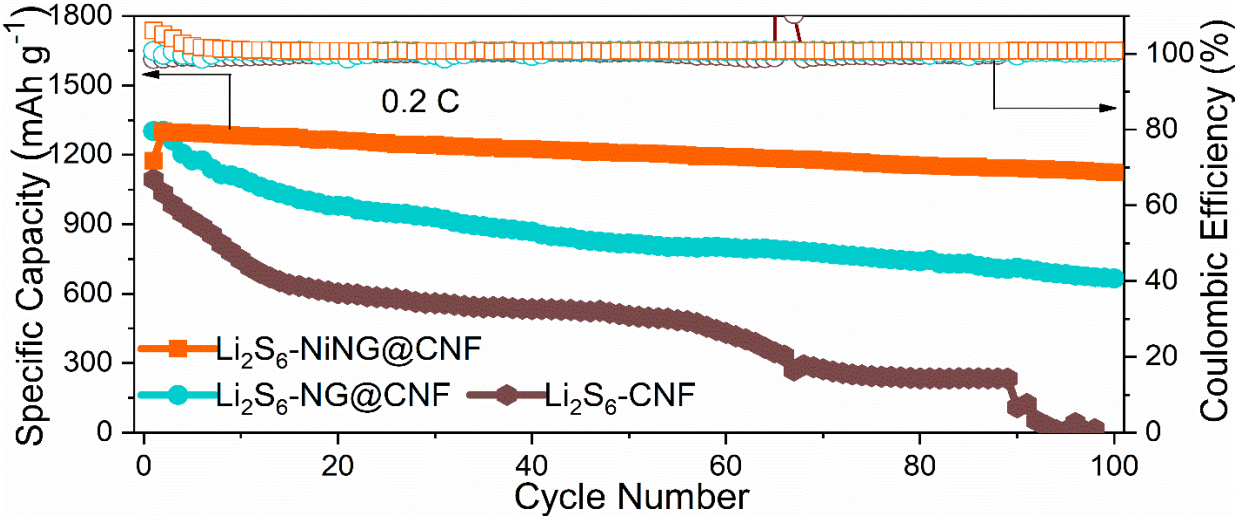

Figure 5.14 comparison of cycling performances and coulombic efficiency of as-prepared electrodes at 0.2 C.

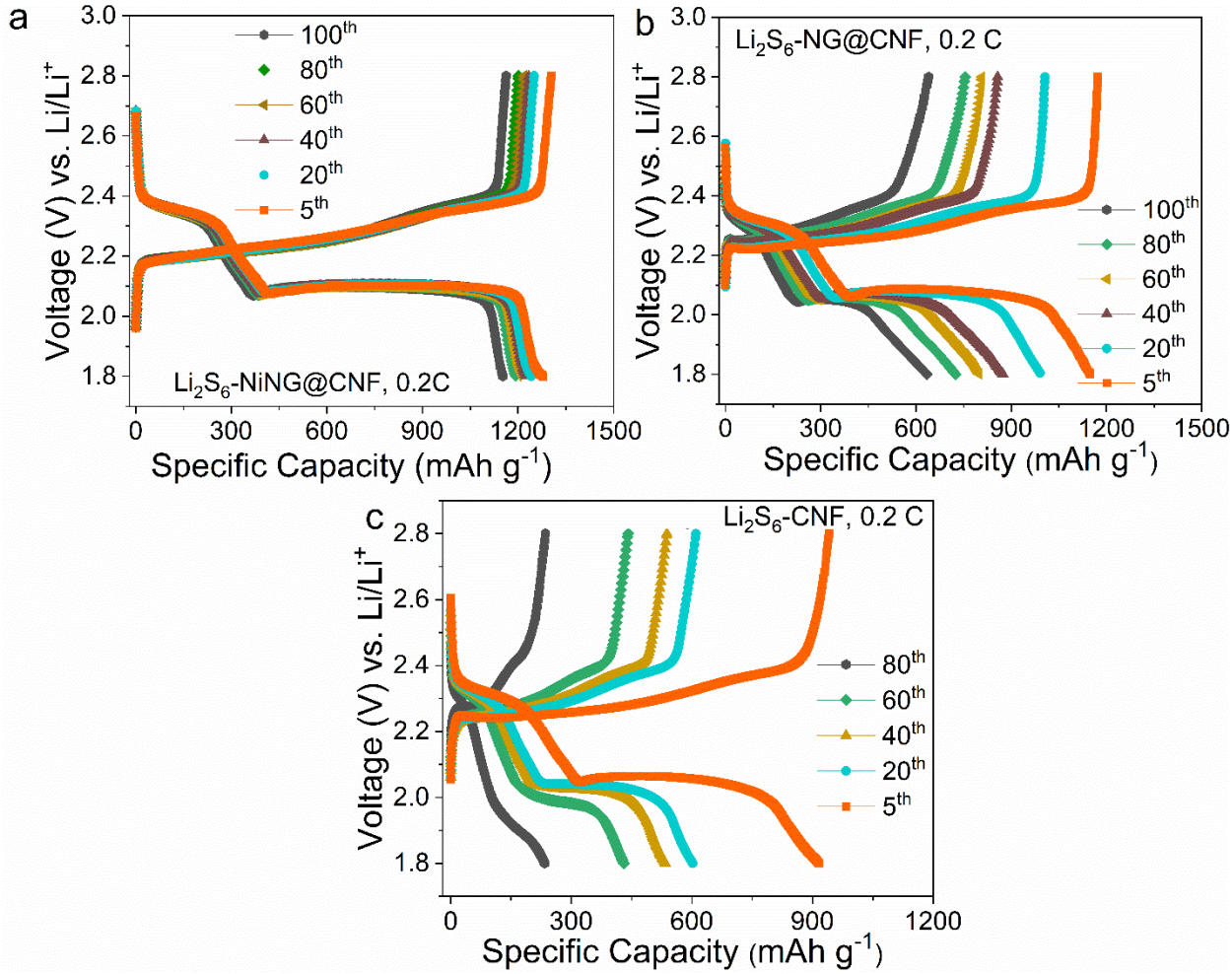

Figure 5.15 Voltage profiles of Li-S cells with (a) Li_2S_6-NiNG@CNF, (b) Li_2S_6-NG@CNF and (c) Li_2S_6-CNF electrodes at 0.2 C over 100 cycles.

During the discharge, solid sulfur is firstly get reduced to liquid long-chain polysulfides, forming higher plateau region at ≈ 2.3 V. The newly formed lithium polysulfides are highly soluble into electrolytes and can cause notorious "shuttling effect". Therefore, the capacity obtained at higher plateau (Q_H) is highly related to the lithium polysulfides trapping ability of the host. On the other hand, the lower plateau region at ≈ 2.05 V is attributed to the liquid-solid phase transformation of lithium polysulfides to Li_2S_2/ Li_2S. Such transformation requires a high energy of activation due to insulating nature of Li_2S_2/ Li_2S. Thus, the capacity generated at lower plateau (Q_L) can be moderated by the electrical conductivity and electrocatalytic properties of the host. **Figure 5.16**

displays a comparative study of Q_H and Q_L values for different cathodes as a function of their cycle number. As can be seen, the Q_H and Q_L values in the Li-S cell with Li_2S_6-NiNG@CNF electrodes shows higher discharge capacities and excellent capacity retention over 100 cycles, implying high sulfur utilization, minimal lithium polysulfides dissolution and improved polysulfides conversion over Ni-NG electrocatalyst.

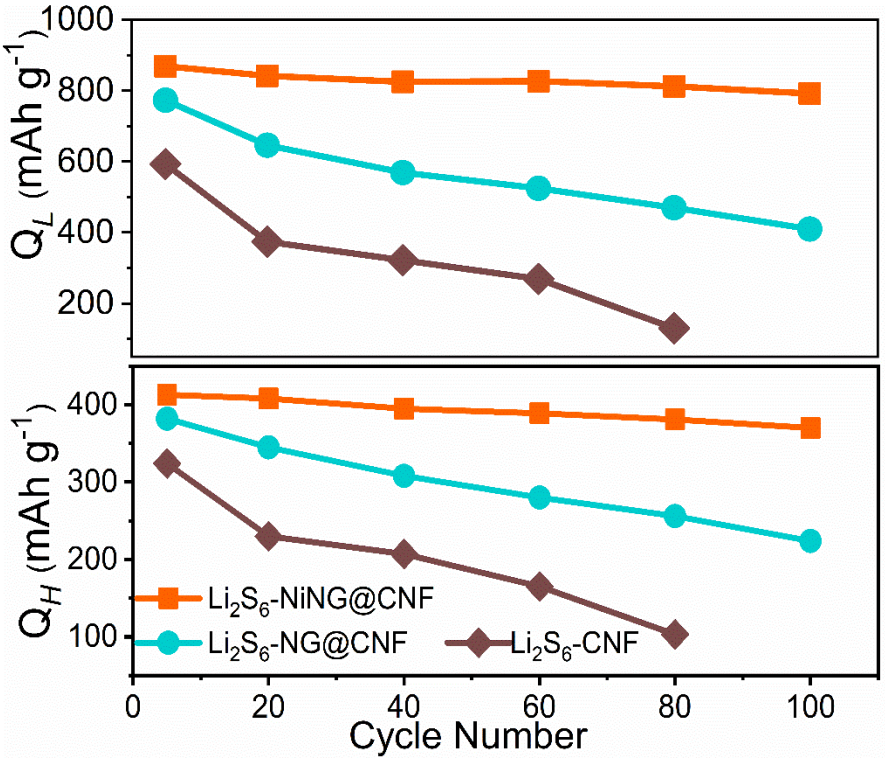

Figure 5.16 Comparisons of upper plateau capacity (Q_H) and lower plateau capacity (Q_L) as a function of cycle number.

The enhanced redox-reaction kinetics and excellent electrochemical reversibility in Li_2S_6-NiNG@CNF cathode is also reflected in the superior rate capability, in **Figure 5.17a**. At 0.2 C, the Li_2S_6-NiNG@CNF electrode is able to deliver a high discharge capacity of 1262 mAh g^{-1}. When the current density raised to 0.5 C and 1C, the discharge capacities are still stabilized at 1128 and 1012 mAh g^{-1}, respectively. Even at high rate of 3 C, the reversible discharge capacity

could reach as high as 848 mAh g^{-1}. More importantly, when the current rate is shifted back to 0.2 C, the Li_2S_6-NiNG@CNF cathode restores almost 91 % of its initial capacity, which is much higher than the capacity retention value (74 %) of Li_2S_6-NG@CNF cathode. This result signifies that the Li_2S_6-NiNG@CNF cathode has better rate tolerance, probably attributed to low charge transfer resistance and excellent electrocatalytic properties of NiNG nanosheets.

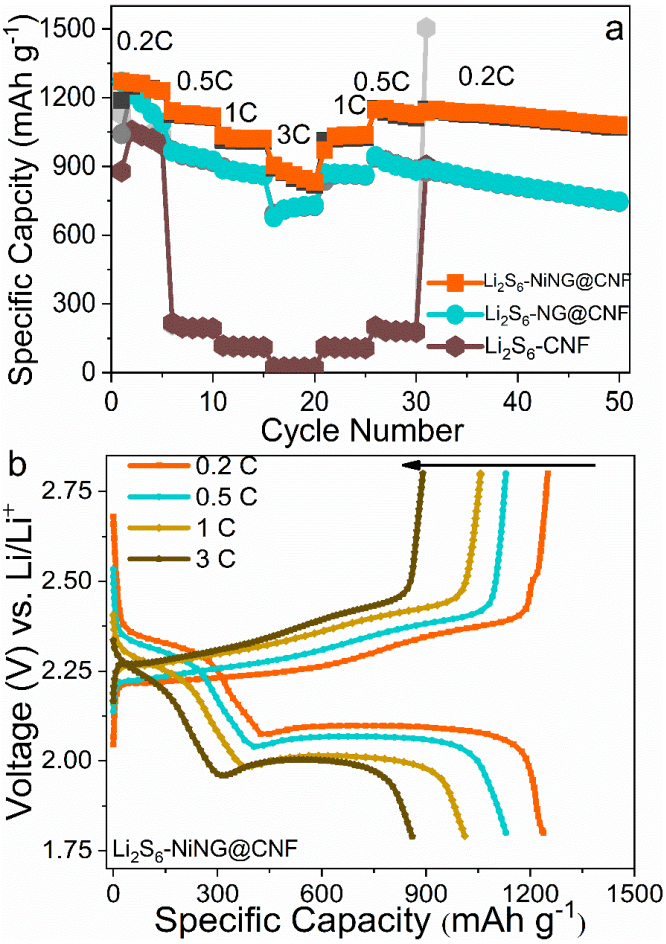

Figure 5.17 (a) rate performances at different current densities of Li-S cells with Li_2S_6-NiNG@CNF, Li_2S_6-NG@CNF and Li_2S_6-CNF cathodes. (b) Discharge/charge profiles of Li-S cell with Li_2S_6-NiNG@CNF electrodes at different current rates.

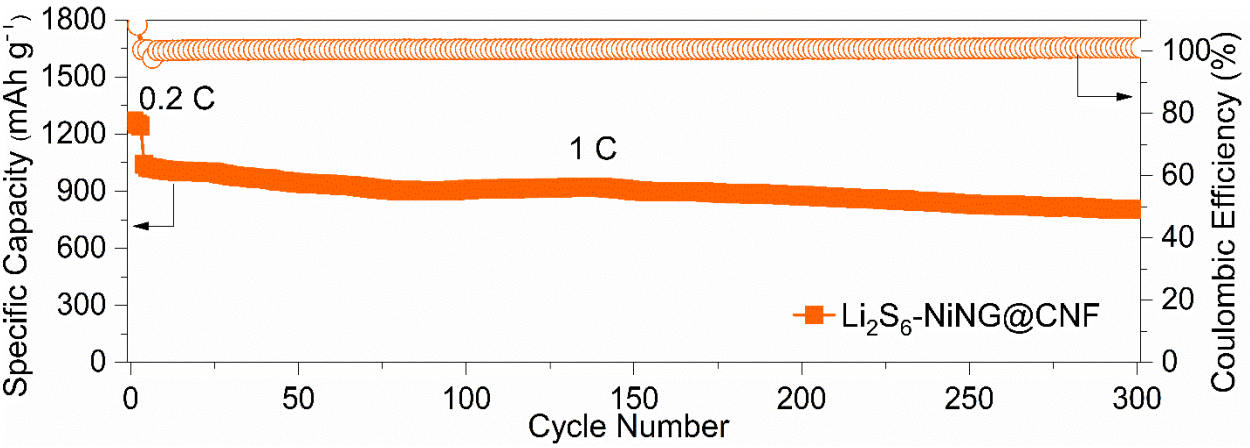

Figure 5.18 long-term cycling performance of the cell with Ni-NG@CNF cathode at a current rate of 1 C.

Figure 5.17b illustrates the galvanostatic discharge-charge curves of Li_2S_6-NiNG@CNF cathodes at different current densities. The graphs able to demonstrate two distinct plateaus even under high current rates. Furthermore, long-term cycling under high current rate has also been performed for Li_2S_6-NiNG@CNF electrode. As shown in **Figure 5.18**, the Li-S cell with Li_2S_6-NiNG@CNF cathode delivers an initial discharge capacity of 1012 mAh g^{-1} at 1 C and retain 805 mAh g^{-1} after 300 cycles, corresponding to capacity fading rate of as low as 0.06 % per cycle. Post Cycling SEM characterization of Li-anodes provide additional evidence of controlled polysulfide shuttling when paired with Li_2S_6-NiNG@CNF cathode. After 100 cycles, the morphologies of the Li-anode in Li_2S_6-NiNG@CNF cell display a relatively uniform and smooth surface (**Figure 5.19a-b**) with very low sulfur content of only 2.23%. In sharp contrast, mossy growth of SEI and highly porous Li-anode was noticed for Li_2S_6-CNF cathode after similar number of cycling, and the sulfur content can be measured to be as high as of 17.18%, indicating severe shuttling of polysulfides into anodic compartment.

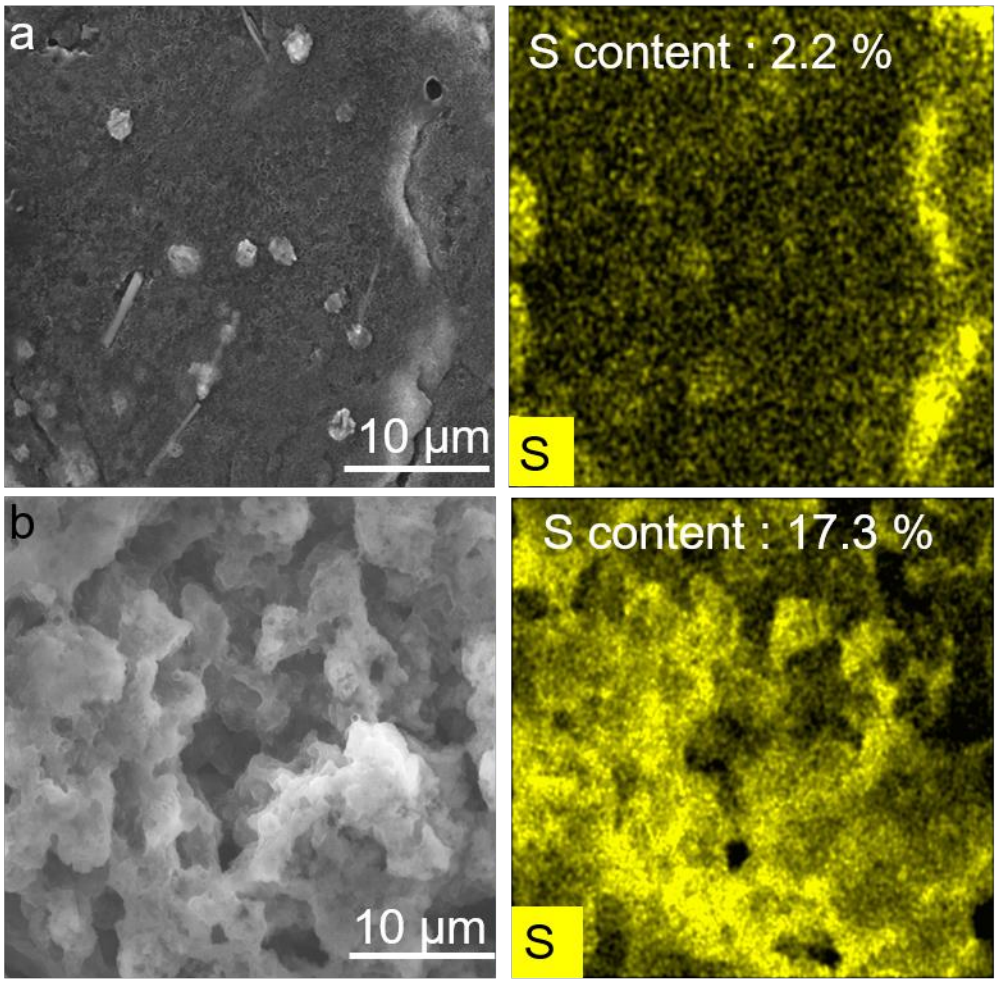

Figure 5.19 SEM images and EDX sulfur mapping of Li-metal surfaces after 100 cycles with (a) Li_2S_6-NiNG@CNF and (b) Li_2S_6-CNF electrodes.

The high sulfur loadings and low electrolyte volume/ sulfur mass ratio (E/S) is crucial to practical applications of Li-S batteries. In light of this, cyclability of the Li_2S_6-NiNG@CNF cathodes with high sulfur loadings and low electrolyte amounts are investigated. To understand the variation of electrochemical performance in the Li_2S_6-NiNG@CNF cathode at various E/S ratios, cells were made with sulfur loading of 4 mg cm^{-2} and E/S was varied from 12 µL mg^{-1} to 7 µL mg^{-1}. When cycled at 0.2 C, the Li-S battery with E/S ratio 7 µL mg^{-1} exhibits a reversible capacity of 951 mAh g^{-1} compared to 1043 mAh g^{-1} of the Li-S cell with E/S ratio 12 µL mg^{-1} (**Figure 5.20**).

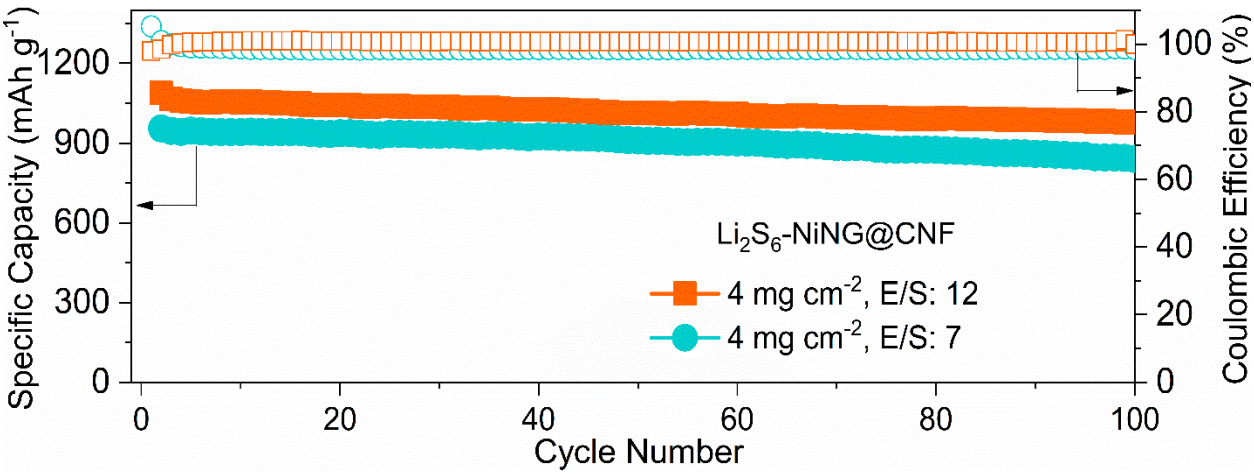

Figure 5.20 Cyclability of Li_2S_6-NiNG cathode at 0.2 C rate with different Electrolyte/Sulfur ratios (E/S: 7 and 12 µL mg^{-1}_{Sulfur}) are compared. Sulfur mass of tested electrodes are 4 mg cm^{-2}.

This can be ascribed to sluggish reaction kinetics under low E/S condition.[202] Nevertheless, the capacity retention value after 100 cycles under both E/S condition is almost comparable (88 % for E/S: 7 vs. 91 % for E/S:12), implying high sulfur utilization and enhanced redox kinetics enabled by the highly conductive NiNG network even under lean electrolyte condition. Furthermore, the cycling stability of Li_2S_6-NiNG@CNF cathodes with higher sulfur loadings (4, 6 and 8 mg cm^{-2}) have been performed at 0.1 C. The E/S ratio for all these cells were controlled to be 7 µL mg^{-1}. As shown in **Figure 5.21a** the Li_2S_6-NiNG@CNF cathodes deliver an initial reversible capacity of 4.3 (1102 mAh g^{-1}) and 5.8 mAh cm^{-2} (961 mAh g^{-1}) at 0.1C with a sulfur loading of 4 and 6 mg cm^{-2}, respectively and retain 4.11 (1053 mAh g^{-1}) and 5.08 mAh cm^{-2} (841 mAh g^{-1}) after 100 cycles. When the sulfur loading was further increased to 8 mg cm^{-2}, the Li-S cell still approaches a high reversible capacity of 6.8 mAh cm^{-2} (822 mAh g^{-1}) and recovered 97 % of its initial capacity after 50 cycles (**Figure 5.21b**). The galvanostatic discharge-charge profiles in **Figure 5.21c** demonstrates no significant voltage hysteresis between discharge-charge curves even with high sulfur loadings.

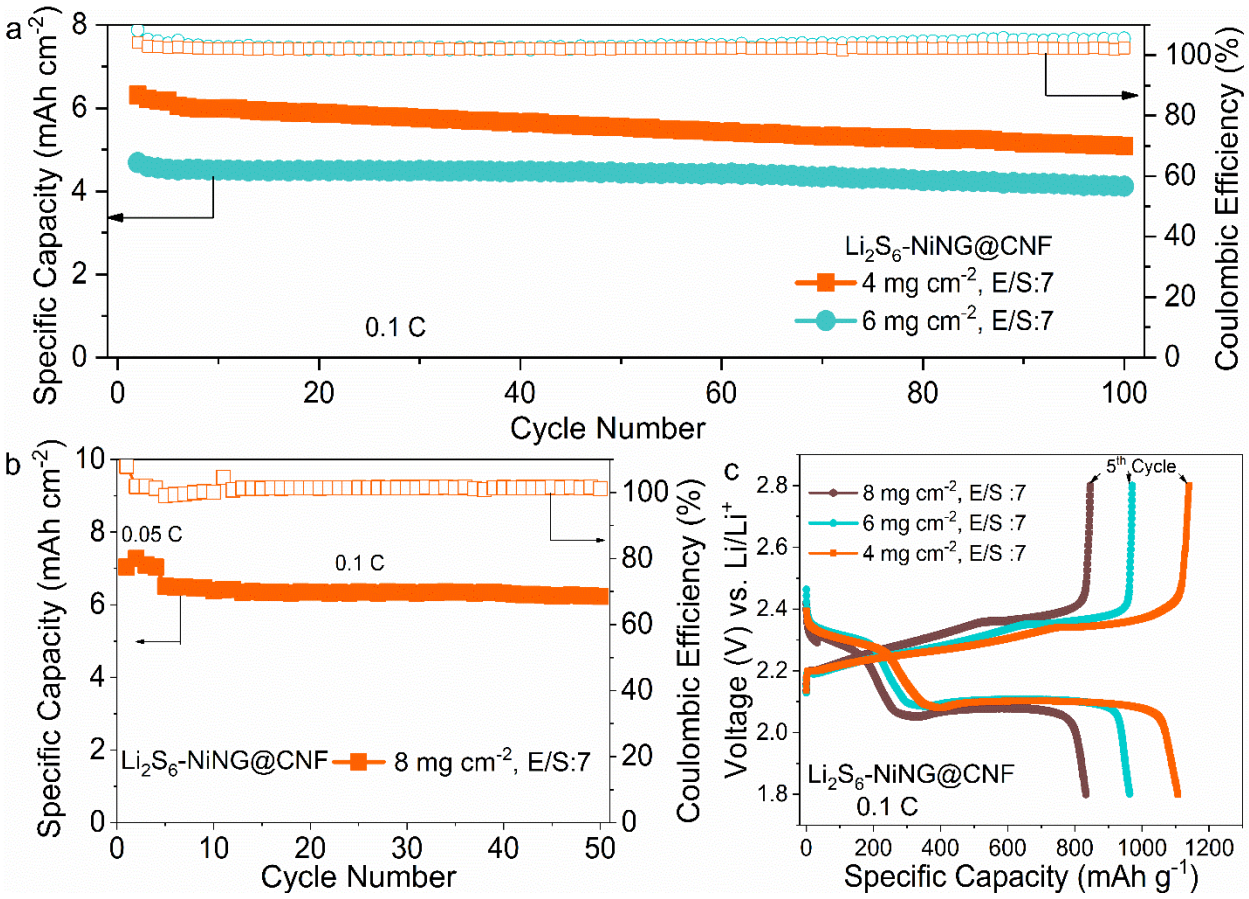

Figure 5.21 (a) Comparison of cycling performance of Li_2S_6-NiNG@CNF cathode with sulfur mass 4 and 6 mg cm $^{-2}$ at current rate of 0.1 C. E/S ratio of both Li-S cells are controlled at 7 µL mg^{-1}_{Sulfur}. (b) Cycling performance of Li_2S_6-NiNG@CNF cathode with high sulfur loading (8 mg cm $^{-2}$) and low E/S (7 µL mg^{-1}_{Sulfur}) at 0.1 C. First 4 discharge/charge cycles were tested at 0.05 C. (c) Galvanostatic discharge/charge curves of Li-S cells with different sulfur mass and same E/S at 0.1 C.

5.4 Conclusion

In summary, we developed a freestanding bilayer cathode consisting of carbon nanofiber (CNF) and nickel and nitrogen co-doped graphene (NiNG). The bottom component of this cathode is composed of mixed phase CNF and NiNG while the top component is made of only NiNG. Benefitting from the unique structural design, this bilayer cathode not only improves the utilization

of active material and high-loading capability but also provides physical / chemical confinement to the escaping polysulfides. More importantly, the NiNG electrocatalyst is polar enough to trap the polysulfides and facilitate their redox conversion during extensive cycling and ensures anode stability. Accordingly, the cycling stability and rate-capability of Li-S cells with Li_2S_6-NiNG@CNF cathode has significantly improved compared to the cells with Li_2S_6-NG@CNF and Li_2S_6-CNF electrodes. In terms of electrochemical performance, this Li_2S_6-NiNG@CNF bilayer cathode exhibits a high specific capacity (1272 mAh g^{-1} at 0.2 C), superior rate-capability (848 mAh g^{-1} at 3C) and long-term cycling stability (only 0.06% capacity decay per cycle over 300 cycles). Moreover, this bilayer cathode could achieve high sulfur loadings (4-8 mg cm^{-2}) and exhibit excellent electrochemical performances even under lean electrolyte condition

Chapter 6

Conclusion and Future Prospective

6.1 Conclusion

In this thesis, different cathode structures were developed to improve the electrochemical performances of Li-S batteries. With this aim, various nanostructured cathodes have been explored to address the practical issues of Li-S batteries such as, insulating nature and volume expansion in active materials, low active material utilization, and intermediate polysulfide dissolution / shutting.

First, a new class of sulfur active material was developed by inverse vulcanization between two eco-friendly sources, sulfur and squalene. Covalent bonding between squalene (organic moiety) and sulfur molecules effectively suppresses the active material dissolution and migration during consecutive charge-discharge process. With such merit, the sulfur-rich copolymer (SP) demonstrates superior electrochemical performances as compared to that of elemental sulfur. For further improvement in electrochemical performances, SP was combined with two-dimensional graphene (G) and three-dimensional graphene-carbon nanotubes (G-CNT) matrixes. The three-dimensional SP@ G-CNT composite shows high discharge capacity value, improved cycling stability and excellent rate performances compared to that of two-dimensional SP@G. This is attributed to the 3D interlinked Sp^2 G-CNT network, which not only improve the 3D electrically conductivity of the composite for better active material utilization, but also enhance the polysulfide entrapment capability and acts as a mechanical buffer against the huge volume change of active material.

Second, a nitrogen-doped mesoporous carbon (NMC) with hierarchical pore architecture was synthesized for high performance Li-S batteries. The materials contain nanopores (< 2 nm) and mesopores (2 – 4 nm), derived from carbonization of porous amine (NH_2)-functionalize metal organic frameworks (NH_2-MOFs). Subsequently, sublimed sulfur was infused into the porous

NMC by simple melt-diffusion method. Through the synergistic effect of nanopores and mesopores, the porous matrix can endow an exceptionally high ion–accessible surface area and low ion diffusion barrier. This conductive host not only improve the active materials utilization but also alleviate the large volume change of sulfur during electrochemical reaction. Besides, the successful N-doping can provide an additional interaction to the migrating lithium polysulfides. Exploiting the interaction between amidogen (NH_2) groups of NH_2-MOFs and the surface functional groups of graphene oxide (GO), a layer-by-layer (LBL) assembled membrane (NH_2-MOF-GO) was prepared by simple vacuum filtration technique and was utilized as an interlayer in between the cathode and the separator (PP). This freestanding permselective membrane can interact to the migrating lithium polysulfides in both physical and chemical ways. Therefore, the newly configured interlayer not only suppress the polysulfide migration, but also ensure the lithium anode stability. As a result, compared with the NMC-S/PP, this rationally designed NMC-S/NH_2-MOF-GO cell shows an obviously improved electrochemical performance, including discharge capacity and high-capacity retention.

Third, a sophisticated bilayer cathode structure was fabricated to increase the sulfur loading, active material utilization and the enhance areal capacity. A simple vacuum filtration technique was adopted to fabricate the freestanding and flexible bilayer cathode. Bottom layer of this cathode consists carbon nanofiber (CNF) and nickel nanoparticles decorated nitrogen-doped graphene (NiNG). The top layer is composed of only NiNG. The integrated CNF and Ni-NG matrixes in the bottom layer not only host the active material but also ensure their high utilization efficiency. Besides, intertwined CNF network possesses abundant void spaces to buffer the volume expansion of the active material. With the presence of nickel nanoparticles, the top NiNG layer accelerates the polysulfide conversion kinetics and effectively block the polysulfide migration. To maximize

the potential of this bilayer host, Li_2S_6 / electrolyte solution (catholyte) was used as active material due well-dispersibility of the catholyte and drop-casted onto bottom layer of the bilayer host. Benefitting from such advantageous structural features, the bilayer Li_2S_6-NiNG@CNF cathodes demonstrates low voltage polarization, improved cycling stability and excellent rate performance. In addition, high sulfur loading up to 8 mg cm^{-2} and an areal capacity of 6.8 mAh cm^{-2} were achieved at low electrolyte to sulfur (E/S) ratio of 7 µL mg^{-1}.

Overall, the work demonstrated in this thesis mainly focused on nanostructure design of cathodes and improving the electrochemical performance of Li-S batteries. Various strategies were adopted, such as developing new-class of sulfur active material; using nitrogen-doped porous carbon as sulfur host, functionalized-MOF interlayer design and implicating electrocatalysts to accelerate the redox kinetics have been strategically explored to address the various issues of cathode. Different physical and electrochemical studies have been conducted to understand the relationship among the physical properties of the cathode, the cell configuration, and the electrochemical performances. In this context, the findings of this doctoral work on cathode modification and understanding the contribution of such 'Smart' cathodes for improving the electrochemical performances will be beneficial to realize high-performance lithium-sulfur batteries.

6.2 Future Prospective

After Li-Ion battery, lithium-sulfur battery have emerged as most promising candidate for long-range EVs and HEVs. However, several issues like, insulating nature and volume expansion in active material; dissolution and shuttling of intermediate polysulfides; and anode degradation still exist. Therefore, it is essential to circumvent these challenges to avail practical application of lithium-sulfur batteries. Regarding this we will provide some suggestions for future work:

For cathode, nitrogen atom doped porous carbon should be preferred as sulfur host to overcome the low conductivity and the volume expansion of sulfur. Besides, such dopant sites can interact to the escaping polysulfides and retard their migration to a certain extent. However, high surface area and high porosity of the host also lead to the less compact electrode structure. Therefore, more electrolytes will be required to sufficiently wet all the electrode surfaces. This will increase the electrolyte/sulfur (E/S, $\mu L\ mg^{-1}$) ratio and reduce the overall energy density values of the Li-S cell. On that context, a systematic study is required for the optimization of the surface area and porosity of the sulfur host to obtain improved electrochemical performances at low E/S ratio. Considering the commercial feasibility, such sulfur composite can be combined with a conductive additive (such as Ni nanoparticles) with electrocatalytic activity. Therefore, such conductive additives not only improve the electronic conductivity of the electrode for better sulfur/polysulfide utilization, but also accelerate the polysulfide conversion reaction kinetics. With such cathode modifications, dissolution and shuttling of polysulfides can be minimized. The low electrolyte/sulfur (E/S) ratio is crucial to increase the overall energy density values of Li-S cells. Excess electrolyte uptake will add considerable weight to the Li-S cell and reduce the specific energy density. In this thesis, the minimum E/S value we have reached is 7 $\mu L\ mg^{-1}$. However, E/S $\leq$ 5 $\mu L\ mg^{-1}$ can also be pursued. To achieve a safe and high energy Li-S battery, the effective utilization and protection of highly reactive lithium metal is also important. Regarding this, stabilizing the anode by coating of an artificial layer or some facile interlayer design could also be explored. To our best knowledge, a perfect combination of rationally designed cathode and stable anode is crucial for high-performing, long-lasting lithium-sulfur batteries.

APPENDIX: NOMENCLATURE

Abbreviations/Symbols	Full name
a.u.	Arbitrary unit
Ar	Argon
BET	Brunauer-Emmett-Teller
BJH	Barrett-Joyner-Halenda
CB	Carbon black
CNT	carbon nanotube
CV	Cyclic Voltammetry
C-rate	Current rate
DI	de-ionized
DMC	Dimethyl carbonate
EC	Ethylene carbonate
EIS	Electrochemical Impedance Spectroscopy
EVs	Electric vehicles
FESEM	Field-Emission Scanning Electron Microscopy
FTIR	Fourier transform infrared spectroscopy
g	Gram
rGO	Reduced Graphene oxide
h	Hour
Hz	Hertz
I	Intensity

HEVs	Hybrid electric vehicles
HRTEM	High-resolution transmission electronic spectroscopy
JCPDS	Joint Committee on Powder Diffraction Standards
Li	Lithium
LIBs	Lithium-ion Batteries
M	Molar concentration
mA h g^{-1}	Milli ampere hour per gram
min	Minute
mm	Millimeter
nm	Nanometer
NMP	1-methyl-2-pyrrolidinone
PC	Propylene carbonate
PTFE	Polytetrafluoroethylene
PVDF	Poly(vinylidene difluoride)
R_{ct}	Charge transfer resistance
R_{Ω}	Ohmic resistance
SAED	Selected area electron diffraction
SEI	Solid Electrolyte Interface
SEM	Scanning electron Microscopy
TEM	Transmission electron microscopy
TGA	Thermogravimetric analysis
XRD	X-ray diffraction
°	Degree

Ω	Ohm
°C	Degree Celsius
Z_w	Warburg impedance

References

(1) Ji, X.; Nazar, L. F. Advances in Li-S Batteries. *J. Mater. Chem.* **2010**, *20* (44), 9821–9826.

(2) Bruce, P. G.; Freunberger, S. A.; Hardwick, L. J.; Tarascon, J. M. Li-O_2 and Li-S Batteries with High Energy Storage. *Nat. Mater.* **2012**, *11* (1), 19–29.

(3) Wild, M.; O'Neill, L.; Zhang, T.; Purkayastha, R.; Minton, G.; Marinescu, M.; Offer, G. J. Lithium Sulfur Batteries, a Mechanistic Review. *Energy Environ. Sci.* **2015**, *8* (12), 3477–

(4) Ji, X.; Lee, K. T.; Nazar, L. F. A Highly Ordered Nanostructured Carbon-Sulphur Cathode for Lithium-Sulphur Batteries. *Nat. Mater.* **2009**, *8* (6), 500–506.

(5) Peng, H. J.; Zhang, Q. Designing Host Materials for Sulfur Cathodes: From Physical Confinement to Surface Chemistry. *Angew. Chemie - Int. Ed.* **2015**, *54* (38), 11018–11020.

(6) Pang, Q.; Tang, J.; Huang, H.; Liang, X.; Hart, C.; Tam, K. C.; Nazar, L. F. A Nitrogen and Sulfur Dual-Doped Carbon Derived from Polyrhodanine@Cellulose for Advanced Lithium-Sulfur Batteries. *Adv. Mater.* **2015**, *27* (39), 6021–6028.

(7) Schneider, A.; Suchomski, C.; Sommer, H.; Janek, J.; Brezesinski, T. Free-Standing and Binder-Free Highly N-Doped Carbon/Sulfur Cathodes with Tailorable Loading for High-Areal-Capacity Lithium-Sulfur Batteries. *J. Mater. Chem. A* **2015**, *3* (41), 20482–20486.

(8) Hart, C. J.; Cuisinier, M.; Liang, X.; Kundu, D.; Garsuch, A.; Nazar, L. F. Rational Design

of Sulphur Host Materials for Li-S Batteries: Correlating Lithium Polysulphide Adsorptivity and Self-Discharge Capacity Loss. *Chem. Commun.* **2015**, *51* (12), 2308–

(9) Park, J.; Yu, B. C.; Park, J. S.; Choi, J. W.; Kim, C.; Sung, Y. E.; Goodenough, J. B. Tungsten Disulfide Catalysts Supported on a Carbon Cloth Interlayer for High Performance Li–S Battery. *Adv. Energy Mater.* **2017**, *7* (11), 1–6.

(10) Jeong, T. G.; Choi, D. S.; Song, H.; Choi, J.; Park, S. A.; Oh, S. H.; Kim, H.; Jung, Y.; Kim, Y. T. Heterogeneous Catalysis for Lithium-Sulfur Batteries: Enhanced Rate Performance by Promoting Polysulfide Fragmentations. *ACS Energy Lett.* **2017**, *2* (2), 327–333.

(11) Chung, W. J.; Griebel, J. J.; Kim, E. T.; Yoon, H.; Simmonds, A. G.; Ji, H. J.; Dirlam, P. T.; Glass, R. S.; Wie, J. J.; Nguyen, N. A.; Guralnick, B. W.; Park, J.; Somogyi, Á.; Theato, P.; Mackay, M. E.; Sung, Y. E.; Char, K.; Pyun, J. The Use of Elemental Sulfur as an Alternative Feedstock for Polymeric Materials. *Nat. Chem.* **2013**, *5* (6), 518–524.

(12) Manthiram, A.; Fu, Y.; Chung, S.; Zu, C.; Su, Y. Rechargeable Lithium − Sulfur Batteries. **2014**.

(13) Wang, C. Y.; Zhang, G.; Ge, S.; Xu, T.; Ji, Y.; Yang, X. G.; Leng, Y. Lithium-Ion Battery Structure That Self-Heats at Low Temperatures. *Nature* **2016**, *529* (7587), 515–518.

(14) Slater, M. D.; Kim, D.; Lee, E.; Johnson, C. S. Sodium-Ion Batteries. *Adv. Funct. Mater.* **2013**, *23* (8), 947–958.

(15) Singh, N.; Arthur, T. S.; Ling, C.; Matsui, M.; Mizuno, F. A High Energy-Density Tin Anode for Rechargeable Magnesium-Ion Batteries. *Chem. Commun.* **2013**, *49* (2), 149–151.

(16) Zhu, Y.; Murali, S.; Stoller, M. D.; Ganesh, K. J.; Cai, W.; Ferreira, P. J.; Pirkle, A.; Wallace,

R. M.; Cychosz, K. A.; Thommes, M.; Su, D.; Stach, E. A.; Ruoff, R. S. Carbon-Based Supercapacitors. **2011**, *332* (June), 1537–1542.

(17) Peng, Z.; Freunberger, S. A.; Chen, Y.; Bruce, P. G. A Reversible and Higher-Rate Li-O2 Battery. *Science (80-.).* **2012**, *337* (6094), 563–566.

(18) Seh, Z. W.; Sun, Y.; Zhang, Q.; Cui, Y. Designing High-Energy Lithium-Sulfur Batteries. *Chem. Soc. Rev.* **2016**, *45* (20), 5605–5634.

(19) Chu, S.; Cui, Y.; Liu, N. The Path towards Sustainable Energy. *Nat. Mater.* **2016**, *16* (1),

(20) Nitta, N.; Wu, F.; Lee, J. T.; Yushin, G. Li-Ion Battery Materials: Present and Future. *Mater. Today* **2015**, *18* (5), 252–264.

(21) Zhan, C.; Wu, T.; Lu, J.; Amine, K. Dissolution, Migration, and Deposition of Transition Metal Ions in Li-Ion Batteries Exemplified by Mn-Based Cathodes-A Critical Review. *Energy Environ. Sci.* **2018**, *11* (2), 243–257.

(22) Nayak, P. K.; Erickson, E. M.; Schipper, F.; Penki, T. R.; Munichandraiah, N.; Adelhelm, P.; Sclar, H.; Amalraj, F.; Markovsky, B.; Aurbach, D. Review on Challenges and Recent Advances in the Electrochemical Performance of High Capacity Li- and Mn-Rich Cathode Materials for Li-Ion Batteries. *Adv. Energy Mater.* **2018**, *8* (8), 1–16.

(23) Diouf, B.; Pode, R. Potential of Lithium-Ion Batteries in Renewable Energy. *Renew. Energy* **2015**, *76*, 375–380.

(24) Deng, D. Li-Ion Batteries: Basics, Progress, and Challenges. *Energy Sci. Eng.* **2015**, *3* (5), 385–418.

(25) Zubi, G.; Dufo-López, R.; Carvalho, M.; Pasaoglu, G. The Lithium-Ion Battery: State of

the Art and Future Perspectives. *Renew. Sustain. Energy Rev.* **2018**, *89* (April 2017), 292–308.

(26) Parellada, J. A.; Dunn, M. M.; Wayland, A.; Cousins, J.; Shaw de Paredes, E. Patient Tracking and Follow-up after Percutaneous Breast Biopsy. *Appl. Radiol.* **1997**, *26* (2), 7–10.

(27) Jung, Y. S.; Lu, P.; Cavanagh, A. S.; Ban, C.; Kim, G. H.; Lee, S. H.; George, S. M.; Harris, S. J.; Dillon, A. C. Unexpected Improved Performance of ALD Coated LiCoO2/Graphite Li-Ion Batteries. *Adv. Energy Mater.* **2013**, *3* (2), 213–219.

(28) Smith, A. J.; Dahn, H. M.; Burns, J. C.; Dahn, J. R. Long-Term Low-Rate Cycling of LiCoO 2 /Graphite Li-Ion Cells at 55°C . *J. Electrochem. Soc.* **2012**, *159* (6), A705–A710.

(29) Zhang, S. S.; Xu, K.; Jow, T. R. Study of the Charging Process of a LiCoO2-Based Li-Ion Battery. *J. Power Sources* **2006**, *160* (2 SPEC. ISS.), 1349–1354.

(30) Etacheri, V.; Marom, R.; Elazari, R.; Salitra, G.; Aurbach, D. Challenges in the Development of Advanced Li-Ion Batteries: A Review. *Energy Environ. Sci.* **2011**, *4* (9), 3243–3262.

(31) Xu, J.; Lawson, T.; Fan, H.; Su, D.; Wang, G. Updated Metal Compounds (MOFs, □S, □OH, □N, □C) Used as Cathode Materials for Lithium–Sulfur Batteries. *Adv. Energy Mater.* **2018**, *8* (10), 1–23.

(32) Wang, X.; Li, G.; Li, J.; Zhang, Y.; Wook, A.; Yu, A.; Chen, Z. Structural and Chemical Synergistic Encapsulation of Polysulfides Enables Ultralong-Life Lithium-Sulfur Batteries. *Energy Environ. Sci.* **2016**, *9* (8), 2533–2538.

(33) Xu, G.; Ding, B.; Pan, J.; Nie, P.; Shen, L.; Zhang, X. High Performance Lithium-Sulfur Batteries: Advances and Challenges. *J. Mater. Chem. A* **2014**, *2* (32), 12662–12676.

(34) Chen, L.; Shaw, L. L. Recent Advances in Lithium-Sulfur Batteries. *J. Power Sources* **2014**, *267*, 770–783.

(35) Wang, D. W.; Zeng, Q.; Zhou, G.; Yin, L.; Li, F.; Cheng, H. M.; Gentle, I. R.; Lu, G. Q. M. Carbon-Sulfur Composites for Li-S Batteries: Status and Prospects. *J. Mater. Chem. A* **2013**, *1* (33), 9382–9394.

(36) Chen, S.; Huang, X.; Sun, B.; Zhang, J.; Liu, H.; Wang, G. Multi-Shelled Hollow Carbon Nanospheres for Lithium-Sulfur Batteries with Superior Performances. *J. Mater. Chem. A* **2014**, *2* (38), 16199–16207.

(37) Wang, H.; Zhang, W.; Liu, H.; Guo, Z. A Strategy for Configuration of an Integrated Flexible Sulfur Cathode for High-Performance Lithium-Sulfur Batteries. *Angew. Chemie - Int. Ed.* **2016**, *55* (12), 3992–3996.

(38) Cheng, X. B.; Huang, J. Q.; Zhang, Q.; Peng, H. J.; Zhao, M. Q.; Wei, F. Aligned Carbon Nanotube/Sulfur Composite Cathodes with High Sulfur Content for Lithium-Sulfur Batteries. *Nano Energy* **2014**, *4*, 65–72.

(39) Zheng, Z.; Guo, H.; Pei, F.; Zhang, X.; Chen, X.; Fang, X.; Wang, T.; Zheng, N. High Sulfur Loading in Hierarchical Porous Carbon Rods Constructed by Vertically Oriented Porous Graphene-Like Nanosheets for Li-S Batteries. *Adv. Funct. Mater.* **2016**, *26* (48), 8952–8959.

(40) Milroy, C.; Manthiram, A. An Elastic, Conductive, Electroactive Nanocomposite Binder for Flexible Sulfur Cathodes in Lithium–Sulfur Batteries. *Adv. Mater.* **2016**, *28* (44), 9744–

9751.

(41) Cuisinier, M.; Cabelguen, P. E.; Evers, S.; He, G.; Kolbeck, M.; Garsuch, A.; Bolin, T.; Balasubramanian, M.; Nazar, L. F. Sulfur Speciation in Li-S Batteries Determined by Operando X-Ray Absorption Spectroscopy. *J. Phys. Chem. Lett.* **2013**, *4* (19), 3227–3232.

(42) Liu, B.; Wang, S.; Yang, Q.; Hu, G. H.; Xiong, C. Thiokol with Excellent Restriction on the Shuttle Effect in Lithium-Sulfur Batteries. *Appl. Sci.* **2018**, *8* (1).

(43) Xu, R.; Lu, J.; Amine, K. Progress in Mechanistic Understanding and Characterization Techniques of Li-S Batteries. *Adv. Energy Mater.* **2015**, *5* (16), 1–22.

(44) Sen Gursoy, S.; Canoluk, C.; Yigit, K. Decoration of TiO2 with Polyfuran to Form a New Nanocomposite via Oxidative Chemical Polymerization. *Int. J. Adv. Sci. Tech. Res.* **2017**, *5* (7), 141–150.

(45) Shi, J. Le; Peng, H. J.; Zhu, L.; Zhu, W.; Zhang, Q. Template Growth of Porous Graphene Microspheres on Layered Double Oxide Catalysts and Their Applications in Lithium-Sulfur Batteries. *Carbon N. Y.* **2015**, *92*, 96–105.

(46) Ding, N.; Chien, S. W.; Hor, T. S. A.; Liu, Z.; Zong, Y. Key Parameters in Design of Lithium Sulfur Batteries. *J. Power Sources* **2014**, *269*, 111–116.

(47) Cai, K.; Song, M. K.; Cairns, E. J.; Zhang, Y. Nanostructured Li2S-C Composites as Cathode Material for High-Energy Lithium/Sulfur Batteries. *Nano Lett.* **2012**, *12* (12), 6474–6479.

(48) Zhou, G.; Paek, E.; Hwang, G. S.; Manthiram, A. High-Performance Lithium-Sulfur Batteries with a Self-Supported, 3D Li2S-Doped Graphene Aerogel Cathodes. *Adv. Energy*

Mater. **2016**, *6* (2), 1–9.

(49) Zhao, Q.; Hu, X.; Zhang, K.; Zhang, N.; Hu, Y.; Chen, J. Sulfur Nanodots Electrodeposited on Ni Foam as High-Performance Cathode for Li-S Batteries. *Nano Lett.* **2015**, *15* (1), 721–726.

(50) Seh, Z. W.; Li, W.; Cha, J. J.; Zheng, G.; Yang, Y.; McDowell, M. T.; Hsu, P. C.; Cui, Y. Sulphur-TiO 2 Yolk-Shell Nanoarchitecture with Internal Void Space for Long-Cycle Lithium-Sulphur Batteries. *Nat. Commun.* **2013**, *4*.

(51) Choi, S.; Seo, D. H.; Kaiser, M. R.; Zhang, C.; Van Der Laan, T.; Han, Z. J.; Bendavid, A.; Guo, X.; Yick, S.; Murdock, A. T.; Su, D.; Lee, B. R.; Du, A.; Dou, S. X.; Wang, G. WO 3 Nanolayer Coated 3D-Graphene/Sulfur Composites for High Performance Lithium/Sulfur Batteries. *J. Mater. Chem. A* **2019**, *7* (9), 4596–4603.

(52) Zhou, W.; Yu, Y.; Chen, H.; Disalvo, F. J. Yolk − Shell Structure of Polyaniline-Coated Sulfur for Lithium − Sulfur Batteries. **2013**.

(53) Zhang, Z.; Kong, L. L.; Liu, S.; Li, G. R.; Gao, X. P. A High-Efficiency Sulfur/Carbon Composite Based on 3D Graphene Nanosheet@Carbon Nanotube Matrix as Cathode for Lithium–Sulfur Battery. *Adv. Energy Mater.* **2017**, *7* (11), 1–12.

(54) Rauh, R. D.; Abraham, K. M.; Pearson, G. F.; Surprenant, J. K.; Brummer, S. B. A Lithium/Dissolved Sulfur Battery with an Organic Electrolyte. *J. Electrochem. Soc.* **1979**, *126* (4), 523–527.

(55) Martin, R. P.; Doub, W. H.; Roberts, J. L.; Sawyer, D. T. Further Studies of the Electrochemical Reduction of Sulfur in Aprotic Solvents. *Inorg. Chem.* **1973**, *12* (8), 1921–

1925.

(56) Chung, S. H.; Manthiram, A. Carbonized Eggshell Membrane as a Natural Polysulfide Reservoir for Highly Reversible Li-S Batteries. *Adv. Mater.* **2014**, *26* (9), 1360–1365.

(57) Nanda, S.; Gupta, A.; Manthiram, A. A Lithium–Sulfur Cell Based on Reversible Lithium Deposition from a Li2S Cathode Host onto a Hostless-Anode Substrate. *Adv. Energy Mater.* **2018**, *8* (25), 2–7.

(58) Ma, G.; Wen, Z.; Wu, M.; Shen, C.; Wang, Q.; Jin, J.; Wu, X. A Lithium Anode Protection Guided Highly-Stable Lithium-Sulfur Battery. *Chem. Commun.* **2014**, *50* (91), 14209–14212.

(59) Li-s, C. Lithium – Sulfur Battery Lithium – Sulfur Battery. **2008**, *46* (1), 2–5.

(60) Mikhaylik, Y. V.; Akridge, J. R. Polysulfide Shuttle Study in the Li/S Battery System. *J. Electrochem. Soc.* **2004**, *151* (11), A1969.

(61) Cui, Y.; Liu, S.; Liu, B.; Wang, D.; Zhong, Y.; Zhang, X.; Wang, X.; Xia, X.; Gu, C.; Tu, J. Bi-Containing Electrolyte Enables Robust and Li Ion Conductive Solid Electrolyte Interphase for Advanced Lithium Metal Anodes. *Front. Chem.* **2020**, *7* (January), 1–10.

(62) Pang, Q.; Nazar, L. F. Long-Life and High-Areal-Capacity Li-S Batteries Enabled by a Light-Weight Polar Host with Intrinsic Polysulfide Adsorption. *ACS Nano* **2016**, *10* (4), 4111–4118.

(63) Yoo, J.; Cho, S. J.; Jung, G. Y.; Kim, S. H.; Choi, K. H.; Kim, J. H.; Lee, C. K.; Kwak, S. K.; Lee, S. Y. COF-Net on CNT-Net as a Molecularly Designed, Hierarchical Porous Chemical Trap for Polysulfides in Lithium-Sulfur Batteries. *Nano Lett.* **2016**, *16* (5), 3292–

3300.

(64) Li, B.; Li, S.; Liu, J.; Wang, B.; Yang, S. Vertically Aligned Sulfur-Graphene Nanowalls on Substrates for Ultrafast Lithium-Sulfur Batteries. *Nano Lett.* **2015**, *15* (5), 3073–3079.

(65) Rehman, S.; Guo, S.; Hou, Y. Rational Design of Si/SiO2@Hierarchical Porous Carbon Spheres as Efficient Polysulfide Reservoirs for High-Performance Li-S Battery. *Adv. Mater.* **2016**, *28* (16), 3167–3172.

(66) Chung, S. H.; Chang, C. H.; Manthiram, A. A Core-Shell Electrode for Dynamically and Statically Stable Li-S Battery Chemistry. *Energy Environ. Sci.* **2016**, *9* (10), 3188–3200.

(67) Singh, A.; Kalra, V. Electrospun Nanostructures for Conversion Type Cathode (S, Se) Based Lithium and Sodium Batteries. *J. Mater. Chem. A* **2019**, *7* (19), 11613–11650.

(68) Cheng, J.; Zhao, D.; Fan, L.; Wu, X.; Wang, M.; Zhang, N.; Sun, K. Ultra-High Rate Li-S Batteries Based on a Novel Conductive Ni2P Yolk-Shell Material as the Host for the S Cathode. *J. Mater. Chem. A* **2017**, *5* (28), 14519–14524.

(69) Park, K.; Cho, J. H.; Jang, J. H.; Yu, B. C.; De La Hoz, A. T.; Miller, K. M.; Ellison, C. J.; Goodenough, J. B. Trapping Lithium Polysulfides of a Li-S Battery by Forming Lithium Bonds in a Polymer Matrix. *Energy Environ. Sci.* **2015**, *8* (8), 2389–2395.

(70) Li, M.; Wan, Y.; Huang, J. K.; Assen, A. H.; Hsiung, C. E.; Jiang, H.; Han, Y.; Eddaoudi, M.; Lai, Z.; Ming, J.; Li, L. J. Metal-Organic Framework-Based Separators for Enhancing Li-S Battery Stability: Mechanism of Mitigating Polysulfide Diffusion. *ACS Energy Lett.* **2017**, *2* (10), 2362–2367.

(71) Bao, W.; Liu, L.; Wang, C.; Choi, S.; Wang, D.; Wang, G. Facile Synthesis of Crumpled

Nitrogen-Doped MXene Nanosheets as a New Sulfur Host for Lithium–Sulfur Batteries. *Adv. Energy Mater.* **2018**, *8* (13), 1–11.

(72) Su, D.; Cortie, M.; Fan, H.; Wang, G. Prussian Blue Nanocubes with an Open Framework Structure Coated with PEDOT as High-Capacity Cathodes for Lithium–Sulfur Batteries. *Adv. Mater.* **2017**, *29* (48), 1–8.

(73) Zhou, F.; Li, Z.; Luo, X.; Wu, T.; Jiang, B.; Lu, L. L.; Yao, H. Bin; Antonietti, M.; Yu, S. H. Low Cost Metal Carbide Nanocrystals as Binding and Electrocatalytic Sites for High Performance Li-S Batteries. *Nano Lett.* **2018**, *18* (2), 1035–1043.

(74) Li, W.; Yao, H.; Yan, K.; Zheng, G.; Liang, Z.; Chiang, Y. M.; Cui, Y. The Synergetic Effect of Lithium Polysulfide and Lithium Nitrate to Prevent Lithium Dendrite Growth. *Nat. Commun.* **2015**, *6* (May).

(75) Liang, X.; Wen, Z.; Liu, Y.; Wu, M.; Jin, J.; Zhang, H.; Wu, X. Improved Cycling Performances of Lithium Sulfur Batteries with LiNO 3-Modified Electrolyte. *J. Power Sources* **2011**, *196* (22), 9839–9843.

(76) Zhang, S. S. Role of LiNO 3 in Rechargeable Lithium/Sulfur Battery. *Electrochim. Acta* **2012**, *70*, 344–348.

(77) Adams, B. D.; Carino, E. V.; Connell, J. G.; Han, K. S.; Cao, R.; Chen, J.; Zheng, J.; Li, Q.; Mueller, K. T.; Henderson, W. A.; Zhang, J. G. Long Term Stability of Li-S Batteries Using High Concentration Lithium Nitrate Electrolytes. *Nano Energy* **2017**, *40* (July), 607–617.

(78) Rosenman, A.; Elazari, R.; Salitra, G.; Markevich, E.; Aurbach, D.; Garsuch, A. The Effect of Interactions and Reduction Products of LiNO 3 , the Anti-Shuttle Agent, in Li-S Battery

Systems . *J. Electrochem. Soc.* **2015**, *162* (3), A470–A473.

(79) Chung, S. H.; Singhal, R.; Kalra, V.; Manthiram, A. Porous Carbon Mat as an Electrochemical Testing Platform for Investigating the Polysulfide Retention of Various Cathode Configurations in Li-S Cells. *J. Phys. Chem. Lett.* **2015**, *6* (12), 2163–2169.

(80) Pang, Q.; Liang, X.; Kwok, C. Y.; Nazar, L. F. Advances in Lithium-Sulfur Batteries Based on Multifunctional Cathodes and Electrolytes. *Nat. Energy* **2016**, *1* (9), 1–11.

(81) Pang, Q.; Kundu, D.; Cuisinier, M.; Nazar, L. F. Surface-Enhanced Redox Chemistry of Polysulphides on a Metallic and Polar Host for Lithium-Sulphur Batteries. *Nat. Commun.* **2014**, *5* (May), 3–10.

(82) Mi, K.; Chen, S.; Xi, B.; Kai, S.; Jiang, Y.; Feng, J.; Qian, Y.; Xiong, S. Sole Chemical Confinement of Polysulfides on Nonporous Nitrogen/Oxygen Dual-Doped Carbon at the Kilogram Scale for Lithium–Sulfur Batteries. *Adv. Funct. Mater.* **2017**, *27* (1).

(83) Weng, W.; Pol, V. G.; Amine, K. Ultrasound Assisted Design of Sulfur/Carbon Cathodes with Partially Fluorinated Ether Electrolytes for Highly Efficient Li/S Batteries. *Adv. Mater.* **2013**, *25* (11), 1608–1615.

(84) Li, G.; Sun, J.; Hou, W.; Jiang, S.; Huang, Y.; Geng, J. Three-Dimensional Porous Carbon Composites Containing High Sulfur Nanoparticle Content for High-Performance Lithium-Sulfur Batteries. *Nat. Commun.* **2016**, *7*.

(85) Chen, S.; Huang, X.; Liu, H.; Sun, B.; Yeoh, W.; Li, K.; Zhang, J.; Wang, G. 3D Hyperbranched Hollow Carbon Nanorod Architectures for High-Performance Lithium-Sulfur Batteries. *Adv. Energy Mater.* **2014**, *4* (8), 1–9.

(86) Ge, Y.; Chen, P.; Zhang, W.; Shan, Q.; Fang, Y.; Chen, N.; Yuan, Z.; Zhang, Y.; Feng, X. Shape-Controlled MnO2as a Sulfur Host for High Performance Lithium-Sulfur Batteries. *New J. Chem.* **2020**, *44* (26), 11365–11372.

(87) Shan, J.; Liu, Y.; Su, Y.; Liu, P.; Zhuang, X.; Wu, D.; Zhang, F.; Feng, X. Graphene-Directed Two-Dimensional Porous Carbon Frameworks for High-Performance Lithium-Sulfur Battery Cathodes. *J. Mater. Chem. A* **2015**, *4* (1), 314–320.

(88) Chung, S. H.; Han, P.; Chang, C. H.; Manthiram, A. A Shell-Shaped Carbon Architecture with High-Loading Capability for Lithium Sulfide Cathodes. *Adv. Energy Mater.* **2017**, *7* (17), 1–7.

(89) Chen, S.; Gao, Y.; Yu, Z.; Gordin, M. L.; Song, J.; Wang, D. High Capacity of Lithium-Sulfur Batteries at Low Electrolyte/Sulfur Ratio Enabled by an Organosulfide Containing Electrolyte. *Nano Energy* **2017**, *31* (September 2016), 418–423.

(90) Zhang, T.; Hong, M.; Yang, J.; Xu, Z.; Wang, J.; Guo, Y.; Liang, C. A High Performance Lithium-Ion-Sulfur Battery with a Free-Standing Carbon Matrix Supported Li-Rich Alloy Anode. *Chem. Sci.* **2018**, *9* (47), 8829–8835.

(91) Zhang, Y.; Li, K.; Li, H.; Peng, Y.; Wang, Y.; Wang, J.; Zhao, J. High Sulfur Loading Lithium-Sulfur Batteries Based on a Upper Current Collector Electrode with Lithium-Ion Conductive Polymers. *J. Mater. Chem. A* **2017**, *5* (1), 97–101.

(92) Li, M.; Zhang, Y.; Hassan, F.; Ahn, W.; Wang, X.; Liu, W. W.; Jiang, G.; Chen, Z. Compact High Volumetric and Areal Capacity Lithium Sulfur Batteries through Rock Salt Induced Nano-Architectured Sulfur Hosts. *J. Mater. Chem. A* **2017**, *5* (40), 21435–21441.

(93) Li, Y.; Fu, K. K.; Chen, C.; Luo, W.; Gao, T.; Xu, S.; Dai, J.; Pastel, G.; Wang, Y.; Liu, B.; Song, J.; Chen, Y.; Yang, C.; Hu, L. Enabling High-Areal-Capacity Lithium-Sulfur Batteries: Designing Anisotropic and Low-Tortuosity Porous Architectures. *ACS Nano* **2017**, *11* (5), 4801–4807.

(94) Jeon, B. H.; Yeon, J. H.; Kim, K. M.; Chung, I. J. Preparation and Electrochemical Properties of Lithium-Sulfur Polymer Batteries. *J. Power Sources* **2002**, *109* (1), 89–97.

(95) Jayaprakash, N.; Shen, J.; Moganty, S. S.; Corona, A.; Archer, L. A. Porous Hollow Carbon@sulfur Composites for High-Power Lithium-Sulfur Batteries. *Angew. Chemie - Int. Ed.* **2011**, *50* (26), 5904–5908.

(96) Xin, S.; Gu, L.; Zhao, N. H.; Yin, Y. X.; Zhou, L. J.; Guo, Y. G.; Wan, L. J. Smaller Sulfur Molecules Promise Better Lithium'sulfur Batteries. *J. Am. Chem. Soc.* **2012**, *134* (45), 18510–18513.

(97) Schneider, A.; Weidmann, C.; Suchomski, C.; Sommer, H.; Janek, J.; Brezesinski, T. Ionic Liquid-Derived Nitrogen-Enriched Carbon/Sulfur Composite Cathodes with Hierarchical Microstructure-a Step toward Durable High-Energy and High-Performance Lithium-Sulfur Batteries. *Chem. Mater.* **2015**, *27* (5), 1674–1683.

(98) K. S. Novoselov, A. K. Geim, S. V. Morozov, D. Jiang, Y. Zhang, S. V. Dubonos, I. V. G. and A. A. F. Electric Field Effect in Atomically Thin Carbon Films. **2016**, *306* (5696), 666–669.

(99) Raccichini, R.; Varzi, A.; Passerini, S.; Scrosati, B. The Role of Graphene for Electrochemical Energy Storage. *Nat. Mater.* **2015**, *14* (3), 271–279.

(100) Li, X.; Zhi, L. Graphene Hybridization for Energy Storage Applications. *Chem. Soc. Rev.* **2018**, *47* (9), 3189–3216.

(101) Wang, J. Z.; Lu, L.; Choucair, M.; Stride, J. A.; Xu, X.; Liu, H. K. Sulfur-Graphene Composite for Rechargeable Lithium Batteries. *J. Power Sources* **2011**, *196* (16), 7030–7034.

(102) Sun, H.; Xu, G. L.; Xu, Y. F.; Sun, S. G.; Zhang, X.; Qiu, Y.; Yang, S. A Composite Material of Uniformly Dispersed Sulfur on Reduced Graphene Oxide: Aqueous One-Pot Synthesis, Characterization and Excellent Performance as the Cathode in Rechargeable Lithium-Sulfur Batteries. *Nano Res.* **2012**, *5* (10), 726–738.

(103) Wang, H.; Yang, Y.; Liang, Y.; Robinson, J. T.; Li, Y.; Jackson, A.; Cui, Y.; Dai, H. Graphene-Wrapped Sulfur Particles as a Rechargeable Lithium-Sulfur Battery Cathode Material with High Capacity and Cycling Stability. *Nano Lett.* **2011**, *11* (7), 2644–2647.

(104) Wang, Z.; Dong, Y.; Li, H.; Zhao, Z.; Bin Wu, H.; Hao, C.; Liu, S.; Qiu, J.; Lou, X. W. D. Enhancing Lithium-Sulphur Battery Performance by Strongly Binding the Discharge Products on Amino-Functionalized Reduced Graphene Oxide. *Nat. Commun.* **2014**, *5* (May).

(105) Tao, Y.; Wei, Y.; Liu, Y.; Wang, J.; Qiao, W.; Ling, L.; Long, D. Kinetically-Enhanced Polysulfide Redox Reactions by Nb2O5 Nanocrystals for High-Rate Lithium-Sulfur Battery. *Energy Environ. Sci.* **2016**, *9* (10), 3230–3239.

(106) He, J.; Luo, L.; Chen, Y.; Manthiram, A. Yolk–Shelled C@Fe3O4 Nanoboxes as Efficient Sulfur Hosts for High-Performance Lithium–Sulfur Batteries. *Adv. Mater.* **2017**, *29* (34), 1–5.

(107) Cao, K.; Liu, H.; Li, Y.; Wang, Y.; Jiao, L. Encapsulating Sulfur in δ-MnO2 at Room Temperature for Li-S Battery Cathode. *Energy Storage Mater.* **2017**, *9* (June), 78–84.

(108) Wu, X.; Du, Y.; Wang, P.; Fan, L.; Cheng, J.; Wang, M.; Qiu, Y.; Guan, B.; Wu, H.; Zhang, N.; Sun, K. Kinetics Enhancement of Lithium-Sulfur Batteries by Interlinked Hollow MoO2 Sphere/Nitrogen-Doped Graphene Composite. *J. Mater. Chem. A* **2017**, *5* (48), 25187–25192.

(109) Ghazi, Z. A.; He, X.; Khattak, A. M.; Khan, N. A.; Liang, B.; Iqbal, A.; Wang, J.; Sin, H.; Li, L.; Tang, Z. MoS2/Celgard Separator as Efficient Polysulfide Barrier for Long-Life Lithium–Sulfur Batteries. *Adv. Mater.* **2017**, *29* (21), 1–6.

(110) Cheng, Z.; Xiao, Z.; Pan, H.; Wang, S.; Wang, R. Elastic Sandwich-Type RGO–VS2/S Composites with High Tap Density: Structural and Chemical Cooperativity Enabling Lithium–Sulfur Batteries with High Energy Density. *Adv. Energy Mater.* **2018**, *8* (10), 1–12.

(111) Yao, Y.; Wang, H.; Yang, H.; Zeng, S.; Xu, R.; Liu, F.; Shi, P.; Feng, Y.; Wang, K.; Yang, W.; Wu, X.; Luo, W.; Yu, Y. A Dual-Functional Conductive Framework Embedded with TiN-VN Heterostructures for Highly Efficient Polysulfide and Lithium Regulation toward Stable Li–S Full Batteries. *Adv. Mater.* **2020**, *32* (6), 1–10.

(112) Yuan, Z.; Peng, H. J.; Hou, T. Z.; Huang, J. Q.; Chen, C. M.; Wang, D. W.; Cheng, X. B.; Wei, F.; Zhang, Q. Powering Lithium-Sulfur Battery Performance by Propelling Polysulfide Redox at Sulfiphilic Hosts. *Nano Lett.* **2016**, *16* (1), 519–527.

(113) Chen, T.; Cheng, B.; Zhu, G.; Chen, R.; Hu, Y.; Ma, L.; Lv, H.; Wang, Y.; Liang, J.; Tie, Z.; Jin, Z.; Liu, J. Highly Efficient Retention of Polysulfides in “Sea Urchin”-Like Carbon

Nanotube/Nanopolyhedra Superstructures as Cathode Material for Ultralong-Life Lithium-Sulfur Batteries. *Nano Lett.* **2017**, *17* (1), 437–444.

(114) Lin, Z.; Li, X.; Huang, W.; Zhu, X.; Wang, Y.; Shan, Z. Active Platinum Nanoparticles as a Bifunctional Promoter for Lithium−Sulfur Batteries. *ChemElectroChem* **2017**, *4* (10), 2577–2582.

(115) Gnana Kumar, G.; Chung, S. H.; Raj Kumar, T.; Manthiram, A. Three-Dimensional Graphene-Carbon Nanotube-Ni Hierarchical Architecture as a Polysulfide Trap for Lithium-Sulfur Batteries. *ACS Appl. Mater. Interfaces* **2018**, *10* (24), 20627–20634.

(116) Simmonds, A. G.; Griebel, J. J.; Park, J.; Kim, K. R.; Chung, W. J.; Oleshko, V. P.; Kim, J.; Kim, E. T.; Glass, R. S.; Soles, C. L.; Sung, Y. E.; Char, K.; Pyun, J. Inverse Vulcanization of Elemental Sulfur to Prepare Polymeric Electrode Materials for Li-S Batteries. *ACS Macro Lett.* **2014**, *3* (3), 229–232.

(117) Kim, H.; Lee, J.; Ahn, H.; Kim, O.; Park, M. J. Synthesis of Three-Dimensionally Interconnected Sulfur-Rich Polymers for Cathode Materials of High-Rate Lithium-Sulfur Batteries. *Nat. Commun.* **2015**, *6*.

(118) Dirlam, P. T.; Simmonds, A. G.; Kleine, T. S.; Nguyen, N. A.; Anderson, L. E.; Klever, A. O.; Florian, A.; Costanzo, P. J.; Theato, P.; Mackay, M. E.; Glass, R. S.; Char, K.; Pyun, J. Inverse Vulcanization of Elemental Sulfur with 1,4-Diphenylbutadiyne for Cathode Materials in Li-S Batteries. *RSC Adv.* **2015**, *5* (31), 24718–24722.

(119) Shukla, S.; Ghosh, A.; Sen, U. K.; Roy, P. K.; Mitra, S.; Lochab, B. Cardanol Benzoxazine-Sulfur Copolymers for Li-S Batteries: Symbiosis of Sustainability and Performance. *ChemistrySelect* **2016**, *1* (3), 594–600.

(120) Chang, C. H.; Chung, S. H.; Manthiram, A. Effective Stabilization of a High-Loading Sulfur Cathode and a Lithium-Metal Anode in Li-S Batteries Utilizing SWCNT-Modulated Separators. *Small* **2016**, *12* (2), 174–179.

(121) Lee, C. L.; Kim, I. D. A Hierarchical Carbon Nanotube-Loaded Glass-Filter Composite Paper Interlayer with Outstanding Electrolyte Uptake Properties for High-Performance Lithium-Sulphur Batteries. *Nanoscale* **2015**, *7* (23), 10362–10367.

(122) Bai, S.; Liu, X.; Zhu, K.; Wu, S.; Zhou, H. Metal-Organic Framework-Based Separator for Lithium-Sulfur Batteries. *Nat. Energy* **2016**, *1* (7).

(123) Cao, R.; Chen, J.; Han, K. S.; Xu, W.; Mei, D.; Bhattacharya, P.; Engelhard, M. H.; Mueller, K. T.; Liu, J.; Zhang, J. G. Effect of the Anion Activity on the Stability of Li Metal Anodes in Lithium-Sulfur Batteries. *Adv. Funct. Mater.* **2016**, *26* (18), 3059–3066.

(124) Yin, Y. X.; Xin, S.; Guo, Y. G.; Wan, L. J. Lithium-Sulfur Batteries: Electrochemistry, Materials, and Prospects. *Angew. Chemie - Int. Ed.* **2013**, *52* (50), 13186–13200.

(125) Rosenman, A.; Markevich, E.; Salitra, G.; Aurbach, D.; Garsuch, A.; Chesneau, F. F. Review on Li-Sulfur Battery Systems: An Integral Perspective. *Adv. Energy Mater.* **2015**, *5* (16), 1–21.

(126) Zhou, G.; Paek, E.; Hwang, G. S.; Manthiram, A. Long-Life Li/Polysulphide Batteries with High Sulphur Loading Enabled by Lightweight Three-Dimensional Nitrogen/Sulphur-Codoped Graphene Sponge. *Nat. Commun.* **2015**, *6*.

(127) Qiu, Y.; Li, W.; Zhao, W.; Li, G.; Hou, Y.; Liu, M.; Zhou, L.; Ye, F.; Li, H.; Wei, Z.; Yang, S.; Duan, W.; Ye, Y.; Guo, J.; Zhang, Y. High-Rate, Ultralong Cycle-Life Lithium/Sulfur

Batteries Enabled by Nitrogen-Doped Graphene. **2014**, 1–7.

(128) Smaller, C. S.; Li, Z.; Jiang, Y.; Yuan, L.; Yi, Z.; Wu, C.; Liu, Y.; Strasser, P.; Huang, Y. ARTICLE A Highly Ordered Meso @ Microporous Sulfur Core À Shell Structured. *ACS Nano* **2014**, *8* (9), 9295–9303.

(129) Demir-Cakan, R.; Morcrette, M.; Nouar, F.; Davoisne, C.; Devic, T.; Gonbeau, D.; Dominko, R.; Serre, C.; Férey, G.; Tarascon, J. M. Cathode Composites for Li-S Batteries via the Use of Oxygenated Porous Architectures. *J. Am. Chem. Soc.* **2011**, *133* (40), 16154–16160.

(130) Bao, W.; Su, D.; Zhang, W.; Guo, X.; Wang, G. 3D Metal Carbide@Mesoporous Carbon Hybrid Architecture as a New Polysulfide Reservoir for Lithium-Sulfur Batteries. *Adv. Funct. Mater.* **2016**, *26* (47), 8746–8756.

(131) Lei, T.; Chen, W.; Huang, J.; Yan, C.; Sun, H.; Wang, C.; Zhang, W.; Li, Y.; Xiong, J. Multi-Functional Layered WS2 Nanosheets for Enhancing the Performance of Lithium–Sulfur Batteries. *Adv. Energy Mater.* **2017**, *7* (4), 1–8.

(132) Griebel, J. J.; Li, G.; Glass, R. S.; Char, K.; Pyun, J. Kilogram Scale Inverse Vulcanization of Elemental Sulfur to Prepare High Capacity Polymer Electrodes for Li-S Batteries. *J. Polym. Sci. Part A Polym. Chem.* **2015**, *53* (2), 173–177.

(133) Li, B.; Li, S.; Xu, J.; Yang, S. A New Configured Lithiated Silicon-Sulfur Battery Built on 3D Graphene with Superior Electrochemical Performances. *Energy Environ. Sci.* **2016**, *9* (6), 2025–2030.

(134) Ghosh, A.; Shukla, S.; Khosla, G. S.; Lochab, B.; Mitra, S. Sustainable Sulfur-Rich Copolymer/Graphene Composite as Lithium-Sulfur Battery Cathode with Excellent

Electrochemical Performance. *Sci. Rep.* **2016**, *6* (January), 1–13.

(135) Yu, B. C.; Jung, J. W.; Park, K.; Goodenough, J. B. A New Approach for Recycling Waste Rubber Products in Li-S Batteries. *Energy Environ. Sci.* **2017**, *10* (1), 86–90.

(136) Marcano, D. C.; Kosynkin, D. V.; Berlin, J. M.; Sinitskii, A.; Sun, Z.; Slesarev, A.; Alemany, L. B.; Lu, W.; Tour, J. M. Improved Synthesis of Graphene Oxide. *ACS Nano* **2010**, *4* (8), 4806–4814.

(137) Chen, S.; Chen, P.; Wang, Y. Carbon Nanotubes Grown in Situ on Graphene Nanosheets as Superior Anodes for Li-Ion Batteries. *Nanoscale* **2011**, *3* (10), 4323–4329.

(138) Shen, K.; Mei, H.; Li, B.; Ding, J.; Yang, S. 3D Printing Sulfur Copolymer-Graphene Architectures for Li-S Batteries. *Adv. Energy Mater.* **2018**, *8* (4), 1–6.

(139) Zhang, L.; Ji, L.; Glans, P. A.; Zhang, Y.; Zhu, J.; Guo, J. Electronic Structure and Chemical Bonding of a Graphene Oxide-Sulfur Nanocomposite for Use in Superior Performance Lithium-Sulfur Cells. *Phys. Chem. Chem. Phys.* **2012**, *14* (39), 13670–13675.

(140) Fu, C.; Li, G.; Zhang, J.; Cornejo, B.; Piao, S. S.; Bozhilov, K. N.; Haddon, R. C.; Guo, J. Electrochemical Lithiation of Covalently Bonded Sulfur in Vulcanized Polyisoprene. *ACS Energy Lett.* **2016**, *1* (1), 115–120.

(141) Goodenough, J. B.; Kim, Y. Challenges for Rechargeable Li Batteries. *Chem. Mater.* **2010**, *22* (3), 587–603.

(142) Cao, R.; Xu, W.; Lv, D.; Xiao, J.; Zhang, J. G. Anodes for Rechargeable Lithium-Sulfur Batteries. *Adv. Energy Mater.* **2015**, *5* (16), 1–23.

(143) Pang, Q.; Shyamsunder, A.; Narayanan, B.; Kwok, C. Y.; Curtiss, L. A.; Nazar, L. F. Tuning

the Electrolyte Network Structure to Invoke Quasi-Solid State Sulfur Conversion and Suppress Lithium Dendrite Formation in Li–S Batteries. *Nat. Energy* **2018**, *3* (9), 783–791.

(144) Xu, X.; Zhou, D.; Qin, X.; Lin, K.; Kang, F.; Li, B.; Shanmukaraj, D.; Rojo, T.; Armand, M.; Wang, G. A Room-Temperature Sodium–Sulfur Battery with High Capacity and Stable Cycling Performance. *Nat. Commun.* **2018**, *9* (1), 1–12.

(145) Fan, X.; Yue, J.; Han, F.; Chen, J.; Deng, T.; Zhou, X.; Hou, S.; Wang, C. High-Performance All-Solid-State Na-S Battery Enabled by Casting-Annealing Technology. *ACS Nano* **2018**, *12* (4), 3360–3368.

(146) Kozen, A. C.; Lin, C. F.; Pearse, A. J.; Schroeder, M. A.; Han, X.; Hu, L.; Lee, S. B.; Rubloff, G. W.; Noked, M. Next-Generation Lithium Metal Anode Engineering via Atomic Layer Deposition. *ACS Nano* **2015**, *9* (6), 5884–5892.

(147) Zhang, J.; Li, M.; Younus, H. A.; Wang, B.; Weng, Q.; Zhang, Y.; Zhang, S. An Overview of the Characteristics of Advanced Binders for High-Performance Li–S Batteries. *Nano Mater. Sci.* **2020**, No. xxxx.

(148) Balach, J.; Jaumann, T.; Klose, M.; Oswald, S.; Eckert, J.; Giebeler, L. Functional Mesoporous Carbon-Coated Separator for Long-Life, High-Energy Lithium-Sulfur Batteries. *Adv. Funct. Mater.* **2015**, *25* (33), 5285–5291.

(149) Carter, R.; Oakes, L.; Douglas, A.; Muralidharan, N.; Cohn, A. P.; Pint, C. L. A Sugar-Derived Room-Temperature Sodium Sulfur Battery with Long Term Cycling Stability. *Nano Lett.* **2017**, *17* (3), 1863–1869.

(150) Ai, W.; Zhou, W.; Du, Z.; Chen, Y.; Sun, Z.; Wu, C.; Zou, C.; Li, C.; Huang, W.; Yu, T.

Nitrogen and Phosphorus Codoped Hierarchically Porous Carbon as an Efficient Sulfur Host for Li-S Batteries. *Energy Storage Mater.* **2017**, *6* (October 2016), 112–118.

(151) Chen, Y. M.; Liang, W.; Li, S.; Zou, F.; Bhaway, S. M.; Qiang, Z.; Gao, M.; Vogt, B. D.; Zhu, Y. A Nitrogen Doped Carbonized Metal-Organic Framework for High Stability Room Temperature Sodium-Sulfur Batteries. *J. Mater. Chem. A* **2016**, *4* (32), 12471–12478.

(152) Sun, Q.; Xi, B.; Li, J. Y.; Mao, H.; Ma, X.; Liang, J.; Feng, J.; Xiong, S. Nitrogen-Doped Graphene-Supported Mixed Transition-Metal Oxide Porous Particles to Confine Polysulfides for Lithium–Sulfur Batteries. *Adv. Energy Mater.* **2018**, *8* (22), 1–10.

(153) Luo, L.; Qin, X.; Wu, J.; Liang, G.; Li, Q.; Liu, M.; Kang, F.; Chen, G.; Li, B. An Interwoven MoO3@CNT Scaffold Interlayer for High-Performance Lithium-Sulfur Batteries. *J. Mater. Chem. A* **2018**, *6* (18), 8612–8619.

(154) Li, X.; Ding, K.; Gao, B.; Li, Q.; Li, Y.; Fu, J.; Zhang, X.; Chu, P. K.; Huo, K. Freestanding Carbon Encapsulated Mesoporous Vanadium Nitride Nanowires Enable Highly Stable Sulfur Cathodes for Lithium-Sulfur Batteries. *Nano Energy* **2017**, *40* (June), 655–662.

(155) Luo, Y.; Luo, N.; Kong, W.; Wu, H.; Wang, K.; Fan, S.; Duan, W.; Wang, J. Multifunctional Interlayer Based on Molybdenum Diphosphide Catalyst and Carbon Nanotube Film for Lithium–Sulfur Batteries. *Small* **2018**, *14* (8), 1–9.

(156) Furukawa, H.; Ko, N.; Go, Y. B.; Aratani, N.; Choi, S. B.; Choi, E.; Yazaydin, A. Ö.; Snurr, R. Q.; O'Keeffe, M.; Kim, J.; Yaghi, O. M. Ultrahigh Porosity in Metal-Organic Frameworks. *Science (80-.).* **2010**, *329* (5990), 424–428.

(157) Zheng, J.; Tian, J.; Wu, D.; Gu, M.; Xu, W.; Wang, C.; Gao, F.; Engelhard, M. H.; Zhang,

J. G.; Liu, J.; Xiao, J. Lewis Acid-Base Interactions between Polysulfides and Metal Organic Framework in Lithium Sulfur Batteries. *Nano Lett.* **2014**, *14* (5), 2345–2352.

(158) Liu, Y. C.; Yeh, L. H.; Zheng, M. J.; Wu, K. C. W. Highly Selective and High-Performance Osmotic Power Generators in Subnanochannel Membranes Enabled by Metal-Organic Frameworks. *Sci. Adv.* **2021**, *7* (10).

(159) Marcano, D.; Kosynkin, D.; Berlin, J. Improved Synthesis of Graphene Oxide. *Acs …* **2010**, *4* (8), 4806–4814.

(160) Zeng, Q.; Wang, D. W.; Wu, K. H.; Li, Y.; Condi De Godoi, F.; Gentle, I. R. Synergy of Nanoconfinement and Surface Oxygen in Recrystallization of Sulfur Melt in Carbon Nanocapsules and the Related Li-S Cathode Properties. *J. Mater. Chem. A* **2014**, *2* (18), 6439–6447.

(161) Sheng, W.; Shi, T.; Sun, B.; Tan, X.; Jiang, T.; Liao, G. Three Dimensional Metal Film Catalyst Assisted Etching of Silicon. *Tech. Proc. 2013 NSTI Nanotechnol. Conf. Expo, NSTI-Nanotech 2013* **2013**, *2* (2), 427–430.

(162) Su, Y. S.; Manthiram, A. Lithium-Sulphur Batteries with a Microporous Carbon Paper as a Bifunctional Interlayer. *Nat. Commun.* **2012**, *3*, 1–6.

(163) Wang, Y.; Wang, L.; Huang, W.; Zhang, T.; Hu, X.; Perman, J. A.; Ma, S. A Metal-Organic Framework and Conducting Polymer Based Electrochemical Sensor for High Performance Cadmium Ion Detection. *J. Mater. Chem. A* **2017**, *5* (18), 8385–8393.

(164) Stankovich, S.; Dikin, D. a.; Piner, R. D.; Kohlhaas, K. a.; Kleinhammes, A.; Jia, Y.; Wu, Y.; Nguyen, S. T.; Ruoff, R. S. Synthesis of Graphene-Based Nanosheets via Chemical

Reduction of Exfoliated Graphite Oxide. *Carbon N. Y.* **2007**, *45* (7), 1558–1565.

(165) Zhao, X.; Cheruvally, G.; Kim, C.; Cho, K.-K.; Ahn, H.-J.; Kim, K.-W.; Ahn, J.-H. Lithium/Sulfur Secondary Batteries: A Review. *J. Electrochem. Sci. Technol.* **2016**, *7* (2), 97–114.

(166) Briggs, D. X-Ray Photoelectron Spectroscopy (XPS). *Handb. Adhes. Second Ed.* **2005**, 621–622.

(167) Zheng, C.; Niu, S.; Lv, W.; Zhou, G.; Li, J.; Fan, S.; Deng, Y.; Pan, Z.; Li, B.; Kang, F.; Yang, Q. H. Propelling Polysulfides Transformation for High-Rate and Long-Life Lithium–Sulfur Batteries. *Nano Energy* **2017**, *33* (January), 306–312.

(168) Zhao, Y.; Sun, Q.; Li, X.; Wang, C.; Sun, Y.; Adair, K. R.; Li, R.; Sun, X. Carbon Paper Interlayers: A Universal and Effective Approach for Highly Stable Li Metal Anodes. *Nano Energy* **2018**, *43* (October 2017), 368–375.

(169) Manthiram, A.; Chung, S. H.; Zu, C. Lithium-Sulfur Batteries: Progress and Prospects. *Adv. Mater.* **2015**, *27* (12), 1980–2006.

(170) Fang, R.; Zhao, S.; Sun, Z.; Wang, D. W.; Cheng, H. M.; Li, F. More Reliable Lithium-Sulfur Batteries: Status, Solutions and Prospects. *Adv. Mater.* **2017**, *29* (48), 1–25.

(171) Chung, S. H.; Chang, C. H.; Manthiram, A. Progress on the Critical Parameters for Lithium–Sulfur Batteries to Be Practically Viable. *Adv. Funct. Mater.* **2018**, *28* (28), 1–20.

(172) Li, J.; Chen, C.; Chen, Y.; Li, Z.; Xie, W.; Zhang, X.; Shao, M.; Wei, M. Polysulfide Confinement and Highly Efficient Conversion on Hierarchical Mesoporous Carbon Nanosheets for Li–S Batteries. *Adv. Energy Mater.* **2019**, *9* (42), 1–10.

(173) Zhang, H.; Gao, Q.; Qian, W.; Xiao, H.; Li, Z.; Ma, L.; Tian, X. Binary Hierarchical Porous Graphene/Pyrolytic Carbon Nanocomposite Matrix Loaded with Sulfur as a High-Performance Li-S Battery Cathode. *ACS Appl. Mater. Interfaces* **2018**, *10* (22), 18726–

(174) Chen, H.; Chen, C.; Liu, Y.; Zhao, X.; Ananth, N.; Zheng, B.; Peng, L.; Huang, T.; Gao, W.; Gao, C. High-Quality Graphene Microflower Design for High-Performance Li–S and Al-Ion Batteries. *Adv. Energy Mater.* **2017**, *7* (17), 1–9.

(175) Gueon, D.; Hwang, J. T.; Yang, S. B.; Cho, E.; Sohn, K.; Yang, D. K.; Moon, J. H. Spherical Macroporous Carbon Nanotube Particles with Ultrahigh Sulfur Loading for Lithium-Sulfur Battery Cathodes. *ACS Nano* **2018**, *12* (1), 226–233.

(176) Ruan, J.; Yuan, T.; Pang, Y.; Luo, S.; Peng, C.; Yang, J.; Zheng, S. Nitrogen and Sulfur Dual-Doped Carbon Films as Flexible Free-Standing Anodes for Li-Ion and Na-Ion Batteries. *Carbon N. Y.* **2018**, *126*, 9–16.

(177) Cheng, X. B.; Peng, H. J.; Huang, J. Q.; Zhang, R.; Zhao, C. Z.; Zhang, Q. Dual-Phase Lithium Metal Anode Containing a Polysulfide-Induced Solid Electrolyte Interphase and Nanostructured Graphene Framework for Lithium-Sulfur Batteries. *ACS Nano* **2015**, *9* (6), 6373–6382.

(178) Chen, Y.; Choi, S.; Su, D.; Gao, X.; Wang, G. Self-Standing Sulfur Cathodes Enabled by 3D Hierarchically Porous Titanium Monoxide-Graphene Composite Film for High-Performance Lithium-Sulfur Batteries. *Nano Energy* **2018**, *47* (March), 331–339.

(179) Chen, D.; Yue, X. Y.; Li, X. L.; Bao, J.; Qiu, Q. Q.; Wu, X. J.; Zhang, X.; Zhou, Y. N. Freestanding Double-Layer MoO3/CNT@S Membrane: A Promising Flexible Cathode for Lithium-Sulfur Batteries. *ACS Appl. Mater. Interfaces* **2020**, *12* (2), 2354–2361.

(180) Li, R.; Zhou, X.; Shen, H.; Yang, M.; Li, C. Conductive Holey MoO2-Mo3N2 Heterojunctions as Job-Synergistic Cathode Host with Low Surface Area for High-Loading Li-S Batteries. *ACS Nano* **2019**, *13* (9), 10049–10061.

(181) Li, Z.; He, Q.; Xu, X.; Zhao, Y.; Liu, X.; Zhou, C.; Ai, D.; Xia, L.; Mai, L. A 3D Nitrogen-Doped Graphene/TiN Nanowires Composite as a Strong Polysulfide Anchor for Lithium–Sulfur Batteries with Enhanced Rate Performance and High Areal Capacity. *Adv. Mater.* **2018**, *30* (45), 1–8.

(182) Zhang, L.; Chen, X.; Wan, F.; Niu, Z.; Wang, Y.; Zhang, Q.; Chen, J. Enhanced Electrochemical Kinetics and Polysulfide Traps of Indium Nitride for Highly Stable Lithium-Sulfur Batteries. *ACS Nano* **2018**, *12* (9), 9578–9586.

(183) Huang, Z. D.; Fang, Y.; Yang, M.; Yang, J.; Wang, Y.; Wu, Z.; Du, Q.; Masese, T.; Liu, R.; Yang, X.; Qian, C.; Jin, S.; Ma, Y. Sulfur in Mesoporous Tungsten Nitride Foam Blocks: A Rational Lithium Polysulfide Confinement Experimental Design Strategy Augmented by Theoretical Predictions. *ACS Appl. Mater. Interfaces* **2019**, *11* (22), 20013–20021.

(184) He, J.; Hartmann, G.; Lee, M.; Hwang, G. S.; Chen, Y.; Manthiram, A. Freestanding 1T MoS 2 /Graphene Heterostructures as a Highly Efficient Electrocatalyst for Lithium Polysulfides in Li-S Batteries. *Energy Environ. Sci.* **2019**, *12* (1), 344–350.

(185) Xiao, S.; Zhang, J.; Deng, Y.; Zhou, G.; Wang, R.; He, Y. B.; Lv, W.; Yang, Q. H. Graphene-Templated Growth of WS2Nanoclusters for Catalytic Conversion of Polysulfides in Lithium-Sulfur Batteries. *ACS Appl. Energy Mater.* **2020**, *3* (5), 4923–4930.

(186) Zhu, X.; Zhao, W.; Song, Y.; Li, Q.; Ding, F.; Sun, J.; Zhang, L.; Liu, Z. In Situ Assembly of 2D Conductive Vanadium Disulfide with Graphene as a High-Sulfur-Loading Host for

Lithium–Sulfur Batteries. *Adv. Energy Mater.* **2018**, *8* (20), 1–9.

(187) Song, Y.; Cai, W.; Kong, L.; Cai, J.; Zhang, Q.; Sun, J. Rationalizing Electrocatalysis of Li–S Chemistry by Mediator Design: Progress and Prospects. *Adv. Energy Mater.* **2020**, *10* (11), 1–21.

(188) Kong, W.; Yan, L.; Luo, Y.; Wang, D.; Jiang, K.; Li, Q.; Fan, S.; Wang, J. Ultrathin MnO2/Graphene Oxide/Carbon Nanotube Interlayer as Efficient Polysulfide-Trapping Shield for High-Performance Li–S Batteries. *Adv. Funct. Mater.* **2017**, *27* (18).

(189) Yu, X.; Zhou, G.; Cui, Y. Mitigation of Shuttle Effect in Li-S Battery Using a Self-Assembled Ultrathin Molybdenum Disulfide Interlayer. *ACS Appl. Mater. Interfaces* **2019**, *11* (3), 3080–3086.

(190) Singhal, R.; Chung, S. H.; Manthiram, A.; Kalra, V. A Free-Standing Carbon Nanofiber Interlayer for High-Performance Lithium-Sulfur Batteries. *J. Mater. Chem. A* **2015**, *3* (8), 4530–4538.

(191) Ghosh, A.; Garapati, M. S.; Vijaya Kumar Saroja, A. P.; Sundara, R. Polar Bilayer Cathode for Advanced Lithium-Sulfur Battery: Synergy between Polysulfide Conversion and Confinement. *J. Phys. Chem. C* **2019**, *123* (17), 10777–10787.

(192) Zhong, Y.; Xia, X.; Deng, S.; Zhan, J.; Fang, R.; Xia, Y.; Wang, X.; Zhang, Q.; Tu, J. Popcorn Inspired Porous Macrocellular Carbon: Rapid Puffing Fabrication from Rice and Its Applications in Lithium–Sulfur Batteries. *Adv. Energy Mater.* **2018**, *8* (1), 1–8.

(193) Wang, Y.; Adekoya, D.; Sun, J.; Tang, T.; Qiu, H.; Xu, L.; Zhang, S.; Hou, Y. Manipulation of Edge-Site Fe–N_2 Moiety on Holey Fe, N Codoped Graphene to Promote the Cycle

Stability and Rate Capacity of Li–S Batteries. *Adv. Funct. Mater.* **2019**, *29* (5), 1–9.

(194) Wang, Z.; Shen, J.; Ji, S.; Xu, X.; Zuo, S.; Liu, Z.; Zhang, D.; Hu, R.; Ouyang, L.; Liu, J.; Zhu, M. B,N Codoped Graphitic Nanotubes Loaded with Co Nanoparticles as Superior Sulfur Host for Advanced Li–S Batteries. *Small* **2020**, *16* (7), 1–9.

(195) Wang, R.; Yang, J.; Chen, X.; Zhao, Y.; Zhao, W.; Qian, G.; Li, S.; Xiao, Y.; Chen, H.; Ye, Y.; Zhou, G.; Pan, F. Highly Dispersed Cobalt Clusters in Nitrogen-Doped Porous Carbon Enable Multiple Effects for High-Performance Li–S Battery. *Adv. Energy Mater.* **2020**, *10* (9), 1–10.

(196) Yin, L. C.; Liang, J.; Zhou, G. M.; Li, F.; Saito, R.; Cheng, H. M. Understanding the Interactions between Lithium Polysulfides and N-Doped Graphene Using Density Functional Theory Calculations. *Nano Energy* **2016**, *25*, 203–210.

(197) Li, Q.; Guo, J.; Zhao, J.; Wang, C.; Yan, F. Porous Nitrogen-Doped Carbon Nanofibers Assembled with Nickel Nanoparticles for Lithium-Sulfur Batteries. *Nanoscale* **2019**, *11* (2), 647–655.

(198) Su, D.; Cortie, M.; Wang, G. Fabrication of N-Doped Graphene–Carbon Nanotube Hybrids from Prussian Blue for Lithium–Sulfur Batteries. *Adv. Energy Mater.* **2017**, *7* (8).

(199) Zhang, L.; Liu, D.; Muhammad, Z.; Wan, F.; Xie, W.; Wang, Y.; Song, L.; Niu, Z.; Chen, J. Single Nickel Atoms on Nitrogen-Doped Graphene Enabling Enhanced Kinetics of Lithium–Sulfur Batteries. *Adv. Mater.* **2019**, *31* (40), 1–9.

(200) She, Z. W.; Wang, H.; Hsu, P.C.; Zhang, Q.; Li. W.; Zheng, G.; Yao, H.; Cui, Y. Facile synthesis of Li_2S-polypyrrole composite structures for high-performance Li_2S cathodes.

Energy Environ. Sci. **2014**, 7, 672-676.

(201) Wang, Z.; Huang, J.; Mao, J.; Guo, Q.; Chen, Z.; Lai, Y. Metal-Organic Frameworks and Their Derivatives with Graphene Composites: Preparation and Applications in Electrocatalysis and Photocatalysis. *J. Mater. Chem. A* **2020**, *8* (6), 2934–2961.

(202) Zhao, M.; Li, B. Q.; Peng, H. J.; Yuan, H.; Wei, J. Y.; Huang, J. Q. Lithium–Sulfur Batteries under Lean Electrolyte Conditions: Challenges and Opportunities. *Angew. Chemie - Int. Ed.* **2020**, *59* (31), 12636–12652.